NASA CR-54201
D2-24056

GPO PRICE $ ______

CSFTI PRICE(S) $ ______

Hard copy (HC) 4.00

Microfiche (MF) .75

ff 653 July 65

METEOROID PROTECTION FOR SPACECRAFT STRUCTURES

by

J. F. Lundeberg, P. H. Stern, and R. J. Bristow

prepared for

NATIONAL AERONAUTICS AND SPACE ADMINISTRATION

CONTRACT NAS3-2570

FACILITY FORM 602

N65-35826 (ACCESSION NUMBER)

(THRU)

104 (PAGES)

1 (CODE)

(NASA CR OR TMX OR AD NUMBER)

32 (CATEGORY)

Aerospace Group
THE BOEING COMPANY
Seattle, Washington

NASA CR-54201
D2-21056

Final Report

METEOROID PROTECTION FOR SPACECRAFT STRUCTURES

by

J. F. Lundeberg, P. H. Stern, and R. J. Bristow

Prepared for

National Aeronautics and Space Administration

October 1965

Contract NAS3-2570

Technical Management
NASA Lewis Research Center
Cleveland, Ohio
Liquid Rocket Technology Branch
Gordon T. Smith

Aerospace Group
THE BOEING COMPANY
Seattle, Washington

BLANK PAGE

METEOROID PROTECTION FOR SPACECRAFT STRUCTURES

by

J. F. Lundeberg, P. H. Stern, and R. J. Bristow

ABSTRACT

A procedure to determine meteoroid-protection requirements for spacecraft structures has been developed based on the meteoroid environment, acceptable risk, mission exposure, and structural response to impact. A rational evaluation of impact damage, based on hypervelocity test data, permits selection of barrier elements for minimum-weight protection, or determination of the maximum particle that can be defeated by an arbitrary barrier configuration. The effect of stress and hypervelocity impact on aluminum tankage at cryogenic temperatures is investigated. The critical stress to resist catastrophic fracture is determined for a range of impact damage patterns, material thicknesses, and operating temperatures.

FOREWORD

This report presents the work accomplished by The Boeing Company from June 26, 1963, to August 26, 1964, on "Meteoroid Protection for Spacecraft Structures," Contract NAS3-2570. The work was administered under the direction of Mr. Gordon Smith of the NASA Lewis Research Center.

CONTENTS

ILLUSTRATIONS

ILLUSTRATIONS (Cont)

---

* See larger version of this figure in back-cover pocket.

TABLES

SYMBOLS

A	Exposed area
a	Critical damage radius in stressed specimens
C	Speed of sound in shield
D	Diameter of projectile
d	Damage diameter in shield
K	Ratio of penetration with filler to penetration without filler
M	Meteoroid mass (gm)
N	Number of witness sheets penetrated
n	Allowable number of penetrations
$P(n)$	Poisson probability of n or fewer penetrations
r	Radius of damage in first witness sheet
S	Spacing between sheets
T	Melting Temperature (°R)
t	Thickness of sheet
V	Velocity of projectile
γ	Half-angle subtended by damage area in first witness sheet
ρ	Density
σ	Gross stress
τ	Exposed time

Subscripts

1	Pertains to shield, space behind shield, or major damage area (if used with spray angle)
2	Pertains to first witness sheet, space behind first witness sheet, or perforated area (if used with spray angle)
3	Pertains to second witness sheet
f	Pertains to filler material
o	Pertains to penetration without filler
p	Pertains to projectile

ILLUSTRATION SYMBOLS*

Symbol	Gun Bore (in.)	Projectile Size (in.)	Projectile Material	Shield Material
⊙	1/4	1/4	Aluminum	Aluminum
◇	↓	↓	↓	301 Stainless Steel
⊛	↓	↓	↓	Lead
◒	↓	↓	↓	Molybdenum
◪	↓	↓	↓	Beryllium-Copper
▼	↓	↓	↓	Tungsten
▶	↓	↓	↓	Tantalum
☼	↓	↓	Pyrex	301 Stainless Steel
♁	↓	↓	Foamed Aluminum	Aluminum
□	↓	0.124 x 0.121	Foamed Nickel	Aluminum
●	1/4	1/8	Aluminum	Aluminum
◈	↓	↓	↓	301 Stainless Steel
⟠	↓	↓	↓	321 Stainless Steel
×	↓	↓	↓	1095 Carbon Steel
⊗	↓	↓	↓	Magnesium-Lithium
⊠	↓	↓	↓	Beryllium-Copper
▣	↓	↓	↓	Titanium
◬	↓	↓	↓	Tantalum
▲	↓	↓	↓	Tungsten
⊖	↓	↓	↓	Copper
⦶	↓	↓	↓	Lead
⊘	↓	↓	↓	Magnesium
◓	1/4	1/8	Aluminum	Molybdenum
⧄	↓	↓	↓	Niobium
⧅	↓	1/16	Pyrex	Aluminum
⦸	↓	↓	Aluminum	↓
✦	↓	1/16 x 1/16	↓	↓
⦽	1/16	1/16	Aluminum	Aluminum
⦵	↓	↓	↓	Magnesium
⧗	↓	↓	↓	Tungsten
+	↓	↓	↓	Zinc
⚲	↓	↓	↓	Magnesium-Lithium
⛛	↓	↓	↓	Tantalum
◑	↓	↓	↓	Lead
■	↓	↓	↓	Beryllium-Copper
◆	↓	↓	↓	301 Stainless Steel
✖	↓	↓	Sapphire	Aluminum

---

* These symbols apply unless otherwise defined on specific figures.

METEOROID PROTECTION FOR SPACECRAFT STRUCTURES

by J. F. Lundeberg, P. H. Stern, and R. J. Bristow

The Boeing Company

SUMMARY

The elements of meteoroid protection of spacecraft structures have been analytically and experimentally studied. The hypervelocity impact tests included specimens of 14 metals and 8 low-density filler materials arranged in simple and composite-barrier configurations. Projectile size ranged from 1/32 to 1/4 inch in diameter and impact velocities varied from 5000 to 27,000 fps.

A design procedure has been developed for selecting the thickness of any element and the spacing between shielding elements for any barrier to yield minimum shielding weight. This method allows assessment of the protection afforded by the vehicle structure and integration of existing structural components into the barrier. Thus, the selection of a shield compatible with other design constraints is ensured. The solution of the empirically based penetration equation is extended into the meteoroid velocity range, and reasonable limits are established for the uncertainties introduced by velocity extrapolation. The solution to the analytical expression is presented as a nomogram, which can be used to design a barrier or to determine the particle that can be defeated by a given structure.

The impact-fracture characteristics of 2014-T6 and 2219-T62 aluminum tanks at cryogenic temperatures were investigated. The critical preimpact stress necessary to resist catastrophic fracture was determined as a function of the diameter of the impact damage pattern.

The results of impact-fracture tests on uniaxially stressed specimens were used to predict the fracture characteristics of biaxially stressed spherical specimens.

Several diagnostic studies were performed to determine experimentally the heat and pressure pulse environment of a shielded structure under conditions of hypervelocity impact. Instrumentation was developed to measure the velocity of impact debris fragments within a layer of low-density fiberglass wool insulation. The results of the pressure and temperature measurements of the debris cloud, although too limited to be of design value, have established the lower limits at which such instrumentation must function.

BLANK PAGE

INTRODUCTION

Original data on meteoroids were obtained from astronomical observation of meteors within Earth's atmosphere. Knowledge of the meteoroid environment has improved, especially since the astronomical data were supplemented by satellite-borne meteoroid sensing experiments. Despite this, the best current estimates differ by several orders of magnitude, and the information on the mass range of most interest to the designer is also the most meager. This mass range, 10^{-2} to 10^{-5} gram, falls between the lower limit of the ground-based astronomical data and the upper limits of satellite experiments. Hopefully, future satellite experiments providing larger-area and longer-life sensors will provide the urgently needed additional data.

Many equations describing hypervelocity cratering of semi-infinite targets have been suggested. These equations are derived from theoretical considerations or from empirical correlations. To obtain a mathematically tractable formulation, the theoretician must reduce the complexities of penetration to a single effective physical process, such as a hydrodynamic analogy (References 1 through 4). The experimentalist, because of limited laboratory simulation capability ($\leq$30,000 fps for well-defined projectiles), must extrapolate test data to meteoroid velocities (35,000 to 235,000 fps). Under these conditions, it is remarkable that agreement between theoretically and experimentally based predictions has been as good as it is.

It is often assumed that cratering predictions for semi-infinite targets can be related to the penetration of single-sheet structures (Reference 5). Although single-sheet pressure compartments are adequate for present generations of small unmanned spacecraft, even modest extensions of vehicle mission capability lead rapidly to prohibitively heavy shielding reinforcements. To overcome this problem, several schemes have been suggested. The simplest concept is a meteoroid bumper, first proposed by Whipple (Reference 6); it has since been studied in various forms by a number of investigators (References 7 and 8). Other concepts include multisheet barriers, low-density insulation barriers, composite combinations of multibumpers and insulation barriers, and mechanical atmospheres of suspended dust clouds (Reference 9). Because most extended mission vehicles will be insulated against heat, the multisheet and insulation shielding arrangement has appeared particularly attractive. Several programs have been performed to evaluate the efficiency of multisheet configurations, both with and without insulative layers (References 10 and 11). The information gathered from these programs has been encouraging but inconclusive because too few tests were performed and not enough experimental parameters were investigated. In addition, it has been found that, under certain circumstances, impact penetration into such specimens can induce explosive reactions that magnify the damage to nearby structures (Reference 12).

Because of inadequate knowledge of the distribution and nature of meteoroids and their impact damage potential, the possibility of the penetration of a practical structure cannot be overlooked. The consequences of such a penetration depend on the type of structural arrangement and on the type of compartment or pressure-vessel penetrated. It has been recognized (Reference 13) that hypervelocity penetration of an intact projectile into liquid-filled tanks could cause catastrophic failure. However, the damage potential to pressure vessels produced by debris fragments from a perforated shield has not been well defined. Recent studies (Reference 14) have shown that a static fracture mechanics criterion is inadequate for designing pressure vessels to resist hypervelocity impact damage. These studies have indicated that the pertinent operational and environmental factors of stress, temperature, and impact must be applied simultaneously when investigating candidate materials for cryogenic pressure vessels.

Tasks that must be performed to provide information useful to spacecraft designers are listed below.

1) The development of a penetration equation suitable for predicting hypervelocity impact damage to the thin-sheet configurations representative of actual space-vehicle structure.
2) A variety of materials with a broad spectrum of physical properties must be tested to ensure that all important variables are accounted for by the equation.
3) A procedure must be devised that permits designers to select and evaluate alternate meteoroid-shielding arrangements. In such a method, calculations must be held to a minimum and the salient geometric design parameters must be prominently displayed. This would then allow rapid consideration of many design options, facilitating the trade-off studies required to determine the effects of vehicle design constraints.
4) The penetration characteristics of low-density fillers must be investigated experimentally to check for undesirable effects and to evaluate weight-saving advantages.
5) Representative composite vehicle structural arrangements must be subjected to hypervelocity impact to check the validity of the predictions and to ascertain shielding capability.
6) Cryogenic fuel-tank materials must be tested under representative environmental conditions and their impact-fracture characteristics evaluated.

A program for accomplishing these tasks has been developed and the tasks completed.

EXPERIMENTAL PROGRAM

TEST PLAN

A meteoroid barrier is the total array of materials required to withstand a critical-design meteoroid. Some of these elements might serve a dual function. The barrier might be placed on the outer shell of the vehicle as an organic part of the load-bearing structure, it might be placed on the components to be protected, or it might be divided between the outer shell and the components. The best arrangement wil~~l depend largely on the size of the meteoroid being con-~~ sidered. Small meteoroids will be most effectively defeated at the outer shell using primarily existing structure, whereas large meteoroids will require that protection be placed, at least in part, contiguous to the vital inner components.

A comprehensive experimental program to study the penetration characteristics of a wide variety of shield and low-density-filler materials has been undertaken. The choice of materials was governed both by practical design considerations and by the need to examine the effects of a broad range of physical variables such as density, melting temperature, and sonic velocity. The metallic materials tested were:

1) Magnesium-lithium;

2) Magnesium;

3) Aluminum;

4) 6Al-4V titanium;

5) Zinc;

6) 301 and 321 stainless steel;

7) 1095 steel;

8) Beryllium-copper;

9) Copper;

10) TZM molybdenum;

11) Niobium;

12) Lead;

13) Tantalum;

14) Tungsten.

In addition, ~~the penetration resistance of the following types of low-density insulation materials was investigated:~~

1) Polyurethane;

2) Polystyrene;

3) Q-felt;

4) Dexiglas;

5) Glass wool;

6) Cork

The materials were evaluated by subjecting selected configurations to hypervelocity impact by metallic projectiles fired from light-gas guns. The test velocities varied from 5000 to 27,000 fps.

To provide a common basis for comparison, a variety of gages between 0.002 and 0.060 inch for each material was tested against a standard array of thin aluminum witness sheets. The three critical quantities describing damage are: spray angle, depth of particle penetration (i.e., number of witness sheets penetrated), and witness-sheet hole-out. The information obtained from these separate tests was combined to assess the damage resistance of the composite structural arrangements used on space vehicles.

A considerable additional weight saving for cryogenic spacecraft modules can be obtained by incorporating the propellant tank wall and insulation with the inner portion of the barrier. This has required investigation of the effect of fragment impact on stressed structural specimens at cryogenic temperatures. Tests have been performed of both uniaxially and biaxially stressed cryogenic specimens to determine the impact conditions necessary to induce catastrophic fracture.

TEST PROCEDURES

Experimental testing for this program has been performed in the Boeing hypervelocity laboratories. The launchers that have been used range from the 1/4-inch-bore light-gas gun down to the 1/32-inch-bore light-gas gun designed specifically for impact investigations of thin-skinned structure. This range of bore sizes provides for convenient launching of different-sized particles needed in developing impact scaling laws.

The 1/4-inch-bore launcher, shown in Figure 1, has been used for the experiments requiring 1/8- and 1/4-inch-diameter projectiles. Maximum velocities attained for these particles have been 6,000 and 23,000 fps, respectively. Instrumentation for this gun includes six independent velocity stations that trigger five 10-megacycle solid-state counters. Spark shadowgraphs and cameras at each station verify the electronic velocity measurement and the integrity of the projectile. Abtronic image converter cameras for high-speed photography and three flash X-ray units are available for studies of impact phenomena.

Figure 2 shows the 1/16-inch-bore light-gas gun. Velocities up to 27,000 fps were obtained using this launcher. The 1/32-inch-bore light-gas gun has been used to launch 0.001-gram projectiles at velocities up to 20,000 fps. Several velocity measuring systems are used with these guns. Photomultiplier tubes, ionization gages, and piezoelectric crystals are used to detect the passage of the particle and to trigger a 10-megacycle counter. Oscilloscope recordings of the pulses are used for verification. Four flash X-ray units are available for velocity-measurement and impact studies. Specimens tested with the 1/4-inch-bore launcher were 8 inches square; those used with the small launchers were rectangles 2 inches wide by 3 inches long. Suitable holders were constructed to allow a variety of barrier configurations to be tested.

Testing of uniaxially loaded structure was accomplished in the 1/4-inch-bore facility. The specimens, as shown in Figure 3, were 8 inches wide by 23 inches long. Calibration tests showed that the loading frame introduced no bending stresses in any direction and that a uniform stress field existed on a section transverse to the axis of the specimen. Loads were applied by means of two hydraulic cylinders connected in parallel and supplied from a common source. When the desired stress level was reached, the load was locked into the loading frame through two nuts on the support columns and the hydraulic cylinders were removed. Continuous monitoring of stresses was obtained from three strain gages connected to a strip-chart recorder.

The temperature environment was provided by circulating either gaseous or liquid nitrogen through a cold box (see Figure 4) attached to the loading frame. A thin membrane on the front of the cold box provided the only contact with the specimen, thus preventing axial load transfer from the specimen to the cold box.

The pressure differential between the inside of the cold box and the evacuated gas-gun range tank caused the membrane to bulge and introduced some bending stresses in the specimen. Calibration tests have shown that this bulging caused additional axial stresses in the middle surface of the plate, but that they were always less than 500 psi.

Temperatures were monitored by means of three copper-constantan thermocouples placed on the front and back of the specimen and in the vicinity of the temperature-compensated strain gages. A view of the rear of the loading frame and cold box in the range tank is shown in Figure 5.

MULTIPLE-THIN-SHEET SPECIMENS

The multiple-thin-sheet specimens consisted of a first sheet (hereafter called the shield or target plate), followed by sheets of constant thickness, called witness sheets (Figure 6). The spaces between witness sheets were equal. The witness-sheet geometry and material were arbitrarily chosen to permit multiple-sheet penetrations; subsequent testing showed that it was possible to account for variations in the witness-sheet arrangements. This demonstrated that the design procedures developed were not biased by the test setup.

The projectiles used were spheres, or cylinders with a length equal to their diameter. The cylinders exhibited damage characteristics similar to spheres of the same diameter when the cylinder impacted normal to its axis of symmetry. If the cylinder impacted at some other attitude, damage could be compared to spherical-projectile data by using the smallest-diameter first-sheet hole size and the mean fragment-spray diameters. The depth of penetration did not depend on the attitude of the cylinder.

DEFINITION OF DAMAGE

One of the more difficult aspects of comparing the test results of several independent investigations is the lack of agreement among authorities on how to describe damage or even on what constitutes failure. For the purpose of this program, four types of damage to thin unstressed metallic specimens are defined. Only the damage that can be described geometrically is considered; changes in material physical properties due to impact are not included. Figure 6 shows the important dimensions.

Shield or Target — For the thin sheets tested under this program, the damage produced by an unfragmented projectile consisted of a well-defined hole in the target.

Spray Angles — Two fragment spray angles are defined. The first is the angle subtended between the edge of the target hole and the primary hole in the first witness sheet. The second spray angle is defined for spherical projectiles as the angle between the edge of the target-sheet hole and the outer perforations in the first witness sheet; for cylindrical projectiles, the second angle is the angle between the edge of the target-sheet hole and the mean radius of perforations in the first witness sheet.

Hole-Out — Hole-out is the area missing from the first witness sheet. Any of the types of damage shown in Figure 7 are possible depending on the experimental conditions.

Penetration — Penetration is the number of witness sheets penetrated. This includes an estimate of partial penetration for the last sheet.

Shield Damage

The well-defined hole that represents damage to thin shields can be predicted with accuracy. The functional relation describing the damage diameter was obtained after exhaustive correlation studies of significant material and geometric properties of both the shield and projectile. This equation, as shown in Figure 8, is:

$$d/D = 3.4\,(t_1/D)^{1/3}\,(V/C)^{1/3}\,(1 - 0.0208\;\rho_1/\rho_p) \qquad (1)$$

The projectiles were 1/16- to 1/4-inch-diameter spheres and 1/16- to 1/8-inch-diameter cylinders (diameter-to-length ratio equal to 1). Some tests were repeated with projectiles of equivalent dimensions, but made from sapphire, pyrex, Lexar, ~~foamed aluminum, or foamed nickel.~~ Test velocities varied from 15,000 to 27,000 fps. Target thicknesses from 0.002 to 0.125 inch were tested.

Fragment Spray Angles

It has long been recognized that for a given combination of shield and projectile there exists a critical velocity at which the shock propagated into the projectile on impact is sufficiently strong to shatter the projectile. If the target is thin enough, the average velocity of the debris cloud (consisting of fragments from both the shield and projectile) is nearly the same as the particle impact velocity. As the projectile velocities increase, the heat energy liberated on impact increases until fragments of the projectile and shield begin to melt or vaporize (or both).

Both fragment size and dispersion are strongly dependent on impact velocity. The magnitude of this effect may be seen in Figure 9, which shows a standard array of 0.020-inch aluminum sheets struck by aluminum projectiles traveling at speeds of from 5000 to 26,000 fps. It has been postulated (Reference 15) that at meteoroid velocities all material involved in the impact will be vaporized, and that no solid debris will impinge on structure behind the shield. Careful examination of the test specimens has indicated that this is unlikely. Examination of the first-witness-sheet spray damage has shown that many of the fragments around the outer damaged diameter impacted at low speed, even for the highest velocity tests. The conclusion that some solid fragments will be present at any velocity can also be obtained theoretically. This is based on the fact that the target hole diameter in a thin target is significantly larger than the projectile diameter. The target material outside of the projectile diameter is removed by shearing action, which begins at the projectile edge and moves outward. The forces causing this shearing have a maximum value at the edge of the impact zone and dissipate as the hole grows. Even at the highest impact velocities, the target fragments near the outer edge of the hole will gain relatively little energy and have low resulting velocity. Therefore, some fragments would gain insufficient energy for melting or vaporization.

When the projectile and target fragments strike the first witness sheet, damage may occur in any of the patterns shown in Figure 7. Two types of fragment spray angles have been defined (Figure 6). The first angle, γ_1, was picked because it gives an indication of the diameter of the deeply penetrating spray. The second spray angle, γ_2, was picked to give an indication of the total potential damage area on the second sheet. As shown in Figure 10, the spray angles can be approximated as:

$$\gamma_1 = 0.28\,(\rho_1/\rho_p)^{2/3}\,(t_1/D)^{1/4}\,(V/C)^{2/3} \qquad (2)$$

$$\gamma_2 = 0.479\,(\rho_1/\rho_p)^{2/3}\,(t_1/D)^{1/3}\,(V/C)^{2/3} \qquad (3)$$

The spray angle, γ_2, reaches a maximum of approximately $\pi/4$ radians, after which it remains constant. The above equations were derived using aluminum projectiles at 15,000 to 25,000 fps impacting various target materials and thicknesses; the aluminum witness sheets all had a sheet-thickness-to-projectile-diameter ratio of 0.16. The spacing between the shield and first witness sheet was 20 projectile diameters.

Normalized spray angles based on Equations 2 and 3 are plotted for a variety of shield materials in Figure 11. The least dense material, magnesium-lithium, produces the smallest spray angle; tungsten, the most dense material, produces the largest. Figure 12 illustrates the difference in spray-angle characteristics produced by magnesium-lithium and tantalum shields. This phenomenon cannot be explained on the basis of shield mass per unit area, since increasing shield thickness of low-density materials did not produce the results indicated in the photograph. However, the melting temperature of the target material has a significant effect. The high-melting-point materials produced a spray of discrete particles with little vaporization, as evidenced by the individual impacts on the second sheet. Low-melting-point materials, on the other hand, produced a more volatilized debris that resulted in greater hole-out, but less penetration.

As discussed previously, the choice of witness-sheet thickness and spacing was somewhat arbitrary. Since it was necessary to correlate the results for the arrays used in the 1/16- and 1/4-inch-gun facilities, and because it was desirable to extend these findings to other configurations, a number of tests were performed to examine the effects of witness-sheet spacing and thickness on spray angle for various materials. Aluminum and steel were chosen as representative of the low- and high-melting-point materials. The results of the test series, shown in Figures 13 and 14, confirm that variations in the geometric arrangements can be accounted for in a rational manner.

Hole-Out

When the projectile and shield fragments are very small, damage to the first witness sheet is similar to that produced by a normal pressure pulse. If the skin is stressed by the impact above its dynamic ultimate strength, the damage is a petalled hole, as shown in Figure 15. If the transient stresses are less than the ultimate, but above the dynamic yield strength, the damage is limited to permanent local deformation, as indicated on the last witness sheet in Figure 15. The normalized hole area for several shield materials is shown in Figure 16 as a function of relative shield thickness. The hole-out of petalled sheets was obtained by measuring the area contained within the line on the petal surface 1 projectile diameter below the original sheet surface. The hole-out of pinholed sheets was obtained by measuring the hole diameters in a typical circular segment. The total hole-out was then calculated by summing the areas of the individual holes. For t_1/D less than 0.2, the hole-out is greatest with shields having a high melting point. When t_1/D is greater than 0.2, the larger hole-out is associated with low-melting-point shields. The high-melting-point shields produce many small pinholes, as shown by the tantalum specimen of Figure 12. An empirical plot showing the physical quantities on which this type of hole-out depends is shown in Figure 17.

The variation of hole-out with changes in witness-sheet spacing and thickness is shown in Figures 18 and 19. Several trends can be seen from these figures. One is that hole-out-versus-witness-sheet-geometry relations are also dependent on shield material. A second is that, for aluminum shields, maximum hole-out occurs at a shield spacing of about 15 projectile diameters. Finally, for three of the four shields tested, the thickness of the witness sheet made little difference in the hole-out.

Penetration

Penetration of the multisheet specimens is defined as the number of witness sheets penetrated plus the penetrated fraction of the sheet against which the fragment stopped. Figure 20 shows the effect of shield thickness on penetration. Melting temperature of the shield appears to be of major importance in determining penetration. Lead, with the lowest melting point, exhibits the least penetration; tungsten, which has the highest melting point, shows the greatest penetration. The combined effects of the important physical properties for all metals tested are shown in Figure 21. The exponent appearing on the shield-thickness term represents an approximation. The large number of data available for aluminum shields made it possible to obtain a more accurate empirical relation to account for shield thickness. Figure 22 shows this function.

The effect of witness-sheet thickness and spacing on penetration is given in Figures 23 through 25. Figure 23 shows that penetration drops off much more rapidly with witness-sheet thickness for steel shields than for aluminum shields. Figure 24 gives penetration as a function of the spacing between the shield and the first witness sheet. Increasing spacing reduces penetration for aluminum shields. However, steel shields produce a maximum penetration near the middle of the spacing range tested. Figure 25 shows the effect of witness-sheet spacing on penetration. The penetration of aluminum-shielded specimens changes little with an increase in witness-sheet spacing; the penetration of steel-shielded specimens decreases rapidly. The relative weights of shield plus witness sheets required to stop the projectile are plotted in Figure 26 as a function of shield thickness. Aluminum, magnesium, and magnesium-lithium are significantly lighter than the other shield materials tested.

COMPOSITE SPECIMENS

A space-vehicle hull ~~is composed of structural and insulating~~ materials, usually arranged with the insulation between two or more thin metallic sheets. Other structural members are present, but have been neglected for this study. To test practical configurations of this type, a number of composite barriers of thin sheets, honeycomb, and low-density-insulation or filler materials were tested using 1/32- to 1/4-inch-diameter magnesium-lithium and aluminum projectiles.

Filler Materials

The filler materials investigated included polyurethane, polystyrene, Q-felt, stabilized Q-felt, Dexiglas, Owens-Corning TW-F insulating wool, and Armstrong low-density cork. All of the filler materials except the cork were first tested in an unshielded configuration approximating a semi-infinite target to determine the relative effects of fragment penetration before testing more complicated arrangements. These tests were performed using 1/32-inch magnesium-lithium projectiles in the velocity range of 14,000 to 20,000 fps. In this unshielded configuration, the penetration damage for all materials appeared to be geometrically similar. Damage consisted of a long cylindrical hole. In addition, there was some heat discoloration for a distance of from 3 to 5 projectile diameters from the central hole.

No weight advantage appears to be gained by increasing the density of the rigid cellular fillers. For example, if the three densities of polystyrene foam are compared on a weight-per-unit-area basis (i.e., depth of penetration times gross density), the quantity of material required to defeat a 0.49-milligram magnesium-lithium particle at approximately 16,000 fps is 0.110 ± 0.010 pound per square foot for all densities. Similar tests using 1.02-milligram aluminum particles at approximately 15,000 fps show that 0.200 ± 0.030 pound per square foot is needed.

Multiple close-packed layers of foil and insulation materials such as Dexiglas do not appear promising as barrier elements. It is estimated that 0.40 pound per square foot will be required to defeat a 1.02 milligram aluminum particle at approximately 18,000 fps. This is twice the weight of a polystyrene filler. None of the fillers gave any indication of the explosive reactions that were discovered later when shielded configurations were tested. This is further evidence that filler evaluation must include testing of configurations approximating the actual proposed usage.

Three types of fiberglass wool containing various amounts of resin binder were tested. The tests were performed to determine if combustible ingredients in the filler enter into a chemical reaction with the fragments. The material properties are tabulated below.

Inorganic Fiber Fillers (With and Without Organic Binders)

Material	Binder	Unrestrained Density (lb/ft^3)	Test Density (lb/ft^3)
BMS 8-48 Johns-Manville Microlite AA	Phenolic Resin 17.5 ±2.5%	1.36	1.02 & 4
Unbonded B Fiberglass	None	0.95	0.85 & 4.2
Insulating Wool — Owens-Corning TW-F	Organic Lubricant	2.5	6.3

Tests of these materials indicated that the quantity of bonding material does not affect the damage pattern in the wool. However, a slight weight advantage may be attainable by using unbonded fiberglass wool. A comparison of all materials tested indicates that fibrous filler materials (glass wool and Q-felt) are more effective than cellular materials (polystyrene and polyurethane) in eroding projectile fragments. Closed-cell foams are undesirable because of secondary damage effects. The outer shield shatters the projectile into many small particles, some of which are vaporized (along with the filler material), giving rise to a highly compressed volume of gas. The resulting pressure pulse shatters the filler material over a wide area adjacent to the path of the particles and substantially increases the damage to the inner shield (Ref. 11). The skin suffers a large petal-shaped hole similar to those frequently seen when explosions occur adjacent to thin-sheet structures. A similar effect is observed for any low-density filler if sufficient space is not provided between the shield and the skin to relieve the compressed gases.

Range Pressure

The effect of range pressure on target damage was investigated by testing identical specimens at range pressures varying between 0.095 and 40 torr. The results of these tests, shown in Figure 27, indicate that no significant variation in target damage can be attributed to the presence of residual atmospheric gases in the test range.

Fragment Velocity

The velocity of the debris in glass wool was measured using an ionization probe. Two specimen configurations were tested. In the first, glass wool was placed ~~directly behind a 0.020-inch aluminum sheet.~~ The second was similar except that a space was left between the aluminum sheet and the wool. The projectile was a 1/4-inch-diameter aluminum sphere fired at approximately 20,000 fps. The results of the tests, shown in Figure 28, indicate that the greatest deceleration occurs as the fragments enter the wool. Because of the limited range of variables examined, no conclusion can be reached concerning specimen geometry, wool density, or projectile characteristics. These tests have, however, demonstrated the feasibility of this experimental technique: it is anticipated that, when sufficient data becomes available, improved estimates can be made of the subsequent damage potential of fragments after they have penetrated various distances into low-density materials.

Composite Configurations

Following preliminary evaluation of the fillers, composite specimens simulating actual spacecraft hulls were tested using aluminum and Lexan projectiles. The projectile diameters ranged from 1/16 to 1/4 inch, and velocities varied from 15,000 to 25,000 ~~fps. Three general configurations were investigated. The~~ first consisted of a low-density filler between two aluminum sheets. The second configuration had three sheets with filler between the first and second or the second and third sheets. The first sheet material was either aluminum or 301 stainless steel; the second two were of aluminum. The third configuration was similar to the second except that honeycomb core was placed either in the first or second space between the sheets. Witness sheets of aluminum placed behind the specimens made it possible to evaluate the relative effectiveness of the barrier, even when they were penetrated.

The composite specimen tests verified the results of the earlier filler tests. In addition, it was found that both cellular and fibrous fillers of the same density had approximately the same stopping power, but the damage to the sheet following the filler was different. This sheet damage increased for the configurations in the order below:

1) Fiberglass wool with preceding air space;

2) Fiberglass wool without air space;

3) Open-cell foam;

4) Closed-cell foam.

Low-density cork was found to shatter over a large areas on impact; damage to adjacent sheets was also high.

When unbonded honeycomb core was placed between aluminum sheets, it was found that penetration occurred as though the honeycomb had not been present. One specimen was tested using bonded honeycomb. The damage to material adjacent to the point of impact was somewhat less but total penetration did not appear to be reduced. In tests performed using honeycomb, neither beneficial nor deleterious effects were noted that could be attributed directly to the presence of honeycomb in the configuration.

The results of the composite barrier testing are summarized in Figure 29. The figure shows unit weight and overall depth for all of the composite specimens impacted by 1/4-inch-diameter aluminum spheres at approximately 20,000 fps. Although many configurations were tested, barrier depth was found to correspond to barrier weight for a particular type of damage. One test (Number 262) does not at first appear to fall within the proper damage zone. However, Test Number 262 contained honeycomb that added to the configuration weight, but did not help defeat the projectile. In Figure 29, two arrows are drawn from several of the points. The arrows showing an increase in barrier depth indicate where the points would lie if the witness sheets were included in the configuration. The horizontal arrows show the increase in unit weight if the final-sheet thickness was increased sufficiently to defeat the projectile. The increase in final-sheet thickness was calculated using the multisheet design procedure to be described later.

Penetration test data were obtained in sufficient quantity to develop a penetration equation applicable to fiberglass wool between aluminum sheets. The geometry of the test specimens is shown in Figure 30 and the test results are shown in Figure 31.

The results indicate that penetration with filler can be related to penetration without filler by the following equation:

$$N_f = K N_o. \tag{4}$$

The factor K was found to depend on projectile velocity and filler thickness and density in the following manner:

$$K = 1-0.9\, S_f/D \left[1 + 113\, (\rho_f/\rho_1)^2\right] f\,(V/C) \tag{5}$$

The velocity functional relationship is shown in Figure 32.

STRESSED SPECIMENS

The consequences of meteoroid impact on a spacecraft module depends on both the meteoroid size and on the spacecraft geometry. If the meteoroid is no larger than the particle for which the module was designed, penetration will be limited to the barrier. For particles of larger size, particle and barrier fragments will strike interior components such as the surface of cryogenic tanks, or may even penetrate into the fluid. When this happens, especially if the tank is stressed due to internal pressurization, the tank may fail catastrophically. The conditions under which this type of failure occurs were investigated by subjecting uniaxial stressed specimens and spherical tanks to controlled hypervelocity impacts. The specimens were of 2219-T62 and 2014-T6 aluminum. Projectiles were 1/8- to 1/4-inch-diameter aluminum spheres. In the majority of tests, a shield was placed in front of the specimen to fragment the projectile. Cryogenic temperatures were obtained by placing a cold box containing liquid nitrogen against the back of the uniaxial specimen. A thin organic diaphragm separated the liquid nitrogen from the stressed sheets. Spherical tank specimens were chilled by filling with cryogen through a controlled pressure port.

Experiments were conducted to determine ~~the effects of impact of~~ an unfragmented projectile into 2014-T6 and 2219-T62 aluminum specimens backed by liquid nitrogen. For this series, no stress was applied. A typical failure is shown in Figure 33. The 0.040-inch-thick 2014-T6 specimens failed even when tested with the smallest projectile, a 1/8-inch-diameter aluminum sphere at 21,000 fps. The 0.100-inch 2014-T6 specimen failed when hit by a 3/16-inch sphere at 24,000 fps, but not when hit by a 1/8-inch sphere at 25,000 fps. No fracture of the 0.100-inch-thick 2219-T62 specimens occurred during tests using the largest projectile, a 1/4-inch-diameter aluminum sphere at 19,000 fps. Although the general trend of data was reasonable and consistent with tests reported elsewhere (Reference 14), the limited scope of this test series precluded any general conclusions concerning the significance of projectile size or specimen ~~thickness. It can be deduced from~~ these tests, however, that 2219-T62 has more resistance to rupture at these temperatures than has 2014-T6.

A second series of investigations was performed with gaseous nitrogen in the cold box. For all cryogenic tests, the specimen was first chilled by circulating liquid nitrogen through the system. Low temperatures in the absence of liquid were achieved by closing the liquid-nitrogen supply line and allowing the liquid in the cold box to boil off. Indicators were used to check the level of liquid. The impact test was performed immediately after boiloff. Minimum temperatures thus obtained varied from -130 to -250°F, depending on the thickness of the specimen. The results of the 0.090-inch-thick 2014-T6 tests are shown in Figure 34. The critical gross stress is shown as a function of damage size. It was not possible to fracture the 0.100-inch-thick 2219-T62 specimens under these conditions. This was due to the lower yield strength and higher impact resistance of this material. The residual strength was found after impact damage by static tensile tests. The results are shown in Figure 35. Two curves give least-square fit of the data for the range tested:

$$\log \sigma = -0.167 \log (2a) + 4.644 \tag{6}$$

$$\log \sigma = -0.167 \log (2a) + 4.566 \tag{7}$$

The upper curve (Euqation 6) gives the residual static strength at room temperature of specimens that were tested at cryogenic temperature and on which a cold box had been mounted. The lower curve (Equation 7) is for specimens that were static tested at room temperature after being impacted at room temperature. The two curves are significantly different despite similarity in apparent impact flaw size. The temperature of the specimens during impact (possibly complicated for these tests by the presence of the cold box) has a major influence on the specimen reaction to impact.

Liquid-nitrogen-backed 0.040-inch-thick 2014-T6 specimens with shields were also tested. All shield and spacing combinations resulted in fracture. Figure 36 shows a typical failure.

The predictions based on uniaxial stress data were checked by testing spherical 2014-T62 aluminum tanks. Figure 37 shows a typical test arrangement. Three biaxial specimen tests were performed. The tank specimen shown in Figure 38 contained liquid nitrogen, but was not pressurized at the time of impact. The fracture corresponds to the failure observed in the uniaxial liquid-backed specimen. Figure 39 shows a spherical specimen after impact. The tank was partially filled with liquid and chilled to -300°F. The liquid supply was then shut off and the tank pressurized using gaseous nitrogen. The temperature and pressure as recorded at the time of impact were -200°F and 1010 psi. The contents of the tank were, therefore, in the supercritical regime and it was not possible to determine the relative percentage of liquid and vapor. The indicated stress at the time of impact was 27,500 psi. This point is shown in Figure 34 and is consistent with the uniaxial data, although not directly comparable because of differences in thicknesses.

The specimen shown in Figure 39 was retested under similar conditions except that the shield spacing was reduced to 3 inches. The resulting catastrophic failure is shown in Figure 40. The fragments of the specimen were recovered and reassembled. Examination of the impact area revealed that no penetration had occurred during impact. It is estimated that the loss of area due to the previous impact had reduced the effective thickness in the area of impact by about 25 percent. Therefore, the local net static stress was approximately 35,000 psi, and failure would be expected.

BLANK PAGE

PENETRATION ANALYSIS

The ability to predict the depth to which a hypervelocity particle will penetrate a target has long been a primary objective in meteoroid research. A number of theoretical and empirical equations have been developed to predict crater depth in semi-infinite targets. These equations have also been used to predict penetration into arrays of multiple thin sheets by multiplying the semi-infinite equations by a constant. This procedure assumes that the parametric relations effective in describing semi-infinite penetration are valid for more complex material and geometric arrangements. Although the validity of such an assumption is doubtful, it is commonly used, especially for preliminary design purposes. There is, however, little in this approach to guide the designer in selecting meteoroid barrier elements for minimum-weight detailed design, or in integrating shielding requirements and other operational constraints.

Using the data obtained during this meteoroid-protection program, a method has been developed for determining penetration into multiple thin-sheet arrays. Either minimum-weight barriers or shielding that incorporates load-carrying structures can be designed. Two penetration equations have been derived. One is approximate, but is valid for any projectile and shield-material combination. The other will predict penetration quite accurately, but is based only on data for aluminum projectiles penetrating aluminum shields.

PENETRATION PARAMETERS

The material and geometric parameters that have been considered in developing the penetration characteristics of multiple-sheet barriers are discussed below. Limitations on the validity of the equations and their extrapolations are also indicated.

Projectile Shape

Spheres and cylinders with a length-to-diameter ratio of 1 have been tested. It is assumed that test results are applicable to all particles with a length-to-diameter ratio of approximately unity.

Projectile Velocity

A velocity range of 15,000 to 26,000 fps was used in deriving the dependence of penetration on velocity. Reasonable confidence may be placed in velocity extrapolations of 10 to 15 percent. However, at meteoroid velocities the uncertainty (using several rational extrapolation techniques) in the thickness of the last sheet of a three-element barrier is at least a factor of 3.5. The corresponding uncertainty in total shielding weight is a factor of 2.

Shield Thickness

For aluminum projectiles penetrating aluminum targets, shield-thickness-to-projectile-diameter ratios of 0.03 to 1 are valid. For other materials, thickness-to-diameter ratios of 0.10 to 0.5 may be used. Figures 41 and 42 show the effect of extending the range of thickness-to-diameter ratio beyond that given above.

Sheets Behind the Shield

The penetration prediction charts were derived only for aluminum sheets behind the shield. The charts should, therefore, be applied only to aluminum structures, although sheets of magnesium and magnesium-lithium are admissible. No allowable thickness range has been established, but sheet-thickness-to-projectile-diameter ratios of 0.08 to 0.40 have been tested.

Sheet Spacing

As shown in Figures 23 through 25, the effect of spacing was found for shields of aluminum and stainless steel. First- to second-sheet spacing was found to be important for aluminum shields, whereas spacing behind the second sheet was found to be significant only for shields of stainless steel. Spacing does not appear in the penetration equations, except for aluminum into aluminum.

PENETRATION PROCESS

As discussed here, penetration is defined as the maximum penetrating power of individual fragments. In the experimental work it was found that although major damage was confined to the first few sheets of a multiple sheet array, very small fragments (0.01 to 0.03 inch) frequently penetrated from 3 to 25 witness sheets, depending on the material and thickness of the shield. For aluminum, magnesium, and magnesium lithium shields, the number of sheets penetrated never exceeded six.

The design procedure developed from the test data demands that the shield fragment the particle. This demand is easily met because even the strongest projectiles (steel) will be shattered by an aluminum shield with a t/D ratio of no more than 0.08 (the smallest tested) and a projectile velocity exceeding 15,000 fps. It is also assumed that once the projectile is shattered, the physical process governing the penetration of all subsequent sheets is the same. The best physical proof offered to validate this assumption is that microscopic examination of the perforations in the witness sheets reveals no visible variation from one sheet to the next. Subject to the above restrictions, the penetration of any projectile into any shield followed by aluminum sheets of constant thickness is given by

$$N \propto \left(\frac{T_1 + T_p}{T_2}\right) \left(\frac{\rho_1 + \rho_p}{\rho_2}\right)^{1/2} \left(\frac{t_1}{t_2}\right)^{1/3} \left(\frac{V}{C}\right)^{-4/3} \left(\frac{D}{t_2}\right)^{1/4} \qquad (8)$$

or

$$N \propto P\, t_2^{-7/12} \qquad (9)$$

where $$P = \left(\frac{T_1 + T_p}{T_2}\right) \left(\frac{\rho_1 + \rho_p}{\rho_2}\right)^{1/2} \left(\frac{V}{C}\right)^{-4/3} (t_1)^{1/3}\ p^{1/4} \qquad (10)$$

(Equation 8 has been verified experimentally for velocities of 13,000 to 26,000 fps.)

If all terms in Equation 10 are held constant, then

$$N\ (t_2)^{7/12} = \text{constant} \qquad (11)$$

where all the N sheets have constant thickness. If the thickness of the penetrated sheets (excepting the shield) were changed, the number of sheets penetrated becomes

$$N_b = N_a \left(\frac{t_{2a}}{t_{2b}}\right)^{7/12} \qquad (12)$$

where: N_a = sheets penetrated in Configuration a

N_b = sheets penetrated in Configuration b

t_{2a} = thickness of each sheet of Configuration a behind shield

t_{2b} = thickness of each sheet of Configuration b behind shield.

From Equation 12 it can be seen that an experiment on one configuration can be used to predict the required thickness, t_{2b}, for a desired penetration, N_b, in a geometrically similar configuration, provided all other conditions are held constant.

Consider the case for which the second sheet of the desired configuration has a thickness, t_2, that is different from t_3, the thickness of all subsequent sheets. Because Equation 12 is predicated on the condition that all sheets behind the shield are of the same thickness, it is first necessary to calculate an intermediate configuration that has all sheets of thickness t_2. Applying Equation 12 to the results of a test configuration, a, we calculate the intermediate configuration, b (see Figure 43). The shield, spacing, and t_2 of Configuration b are identical to those of Configuration c. It is now necessary to transform the remaining $(N_b - 1)$ sheets of thickness t_{2b} into the required $(N_c - 1)$ sheets of thickness t_{3c}:

$$(N_c - 1) = (N_b - 1) \left(\frac{t_{3b}}{t_{3c}}\right)^{7/12} \qquad (13)$$

because $t_{3b} = t_{2b}$

$$t_{3c} = \left(\frac{N_c - 1}{N_b - 1}\right)^{12/7} t_{2b}$$

Substituting Equation 12:

$$t_{2c} = \left[\frac{N_c - 1}{N_a\left(\frac{t_{2a}}{t_{2b}}\right)^{7/12} - 1}\right]^{12/7} \qquad (14)$$

Therefore, it is possible to predict the penetration resistance of any aluminum multisheet barrier for a given particle and velocity from a single test, provided that the shield material and shield spacing are held constant.

A number of tests are needed to determine the thickness function in

$$N = f\,(V,\ D,\ S_1,\ t_1,\ t_2,\ H) \qquad (15)$$

where H = material property.

Because of this requirement, the only condition for which Equation 15 was established was for the penetration of aluminum projectiles into aluminum shields. The empirical curve for these data is shown in Figure 22 and is given by the equation:

$$N = \left(\frac{V}{C}\right)^{-4/3}\left(\frac{D}{t_2}\right)^{7/12}\left(\frac{S_1}{D}\right)^{-5/12}\left[2.42\left(\frac{t_1}{D}\right)^{-1/3} + 4.26\left(\frac{t_1}{D}\right)^{1/3} - 4.18\right] \qquad (16)$$

where $0.7 < (V/C) < 2$ $\left[\text{for } V/C > 2 \quad \text{see Figure 46}\right]$.

If the effects of material melting point and density are introduced into Equation 16 along with an approximation for the t_1/D function, and if the spacing term $(S_1/D)^{-5/12}$ is omitted, Equation 16 reverts to Equation 8. It is because of the uncertainty in the spacing and t_1/D functions that Equation 8 should be used in conjunction with a test for nonaluminum shields.

Because of the amount of labor required to solve Equation 16 or relations similar to Equation 14, a nomogram (Figure 44) has been prepared. The sample problem shows how a three-sheet barrier (one shield plus two backup sheets) is designed using the results of a single standard test. The nomogram is entered at the known test results and with two of the three desired shield geometry values (spacing, thickness, and number of sheets). In the chart, N is the penetration beyond the shield, or the penetration beyond some other point in the array. Fractional values of N are used in deriving a solution, but the next larger integer should be used for the total number of sheets desired in the final design. For example, assume that a three-sheet configuration is desired such that t_2 and t_3 each are at least 0.008-inch thick. Assume that the tested configuration consisted of a shield spaced 0.60 inch from a series of 0.005-inch witness sheets, four of which are penetrated during the test. To start the analysis, choose a reasonable spacing, perhaps 1.25 inches, and enter the chart as shown by the solid-line arrows. For three-sheet construction (N = 2), t_{2b} is 0.010 inch. Because this is greater than 0.008 inch, structural gages must be increased to satisfy the meteoroid requirement. An alternate solution is to increase the first to second element spacing and reduce the thickness until $t_2 = t_3 = 0.008$ inch. However, this recourse is valid only for aluminum shields. Assume for this example that 1.25 inches is the maximum acceptable spacing and that all increases to structural gage will be absorbed by the last sheet. The dotted lines on the chart show that the number of 0.008-inch-thick sheets penetrated is 2.3. Because the thickness of only the third sheet is to be increased, these 2.3 sheets must be converted to one 0.008-inch sheet and an additional single sheet having the same stopping potential as 2.3 sheets 0.008-inch thick. The chart is re-entered at $N_b = 2.3 - 1 = 1.3$. The intersection of the $t_{2b} = 0.008$ line with the $N_b = 1.3$ line gives the protection capability. All points on a horizontal line through this point have the same protection capability. Moving horizontally to N = 1 gives the required thickness ($t_{2b} = 0.012$) of the third sheet.

Both the tested and required configurations discussed in this example were checked by testing with a 1/16-inch-diameter aluminum projectile fired at 19,000 fps into an 0.010-inch aluminum first sheet. The results of these and many other tests have verified the predictions obtained from the chart. Because the effect of spacing has been determined accurately only for aluminum, the chart of Figure 4-2 should be restricted to constant shield spacing, $S_{1a} = S_{1b}$, for nonaluminum shields. However, because tests using low-density particles (foamed aluminum, foamed nickel) have shown that the equation yields conservative results, it is felt that use of variable spacing may be acceptable for fragile low-density projectiles and aluminum targets.

BLANK PAGE

DESIGN APPLICATION

Meteoroid-shielding design is accomplished in two phases — the first consists of selecting the largest particle the shielding must defeat, the second consists of designing the structure to withstand this particle. The nomogram of Figure 45 has been prepared to aid in the selection of the design particle. The chart is entered at the upper right with a desired probability of 0, 1, or more encounters. Proceeding counter clockwise, the next diagram introduces the exposure (the product of area and time). Moving down to a desired flux curve, either the design particle mass may be read from the scale at the lower right, or the design particle diameter can be found from the family of density curves at the lower left. The chart is predicated upon the assumption that a Poisson probability distribution is valid. The probability of n or fewer occurrences for an exposure of $A\tau$ is then given by

$$P(n) = \sum_{k=o}^{k=n} \frac{e^{-\varphi A\tau} (\varphi A\tau)^k}{k!} \tag{17}$$

where φ = cumulative mean number of particles per unit area per unit time of mass m or greater

$\varphi A\tau$ = cumulative mean number of encounters with a particle of mass m or greater for the design exposure

Four flux curves are shown. Curves A and D define pessimistic and optimistic limits, respectively. Curve B has been suggested by Hawkins, Reference 16, while C was suggested by Whipple, Reference 17. The solution of a sample problem is shown on the chart.

After the design particle has been selected, the design of the barrier can proceed. If test results are available in which the above particle was projected at design speed into an array of aluminum sheets, the first sheet of which had the same thickness as the desired shield, the structure following the shield can be designed by Figure 44. If the test had the same first to second sheet spacing as in the design configuration, the nomogram can also be used for first sheets of metals other than aluminum.

Since laboratory techniques preclude the simulation of meteoroid velocities, a design procedure has been developed that incorporates the penetration functions, Equation 16. The solution to the equation is presented in the form of a nomogram in Figure 46. All geometric design parameters such as thickness and spacing have been nondimensionalized in terms of projectile diameter. The areas of validity and restrictions on this chart are the same as those given in the section on penetration parameters. The chart shows a range of possible velocity extrapolations above V/C = 1.6. This range covers the optimistic to pessimistic predictions of previous investigators. The upper limit requires that multisheet penetration be insensitive to velocity changes above 50,000 feet per second. This is the most optimistic extrapolation expected, even if complete vaporization of the projectile and shield fragments were possible. The lower limit represents the most pessimistic velocity effect predicted for semi-infinite and single-sheet impact. That is, above 70,000 feet per second the change in penetration with velocity is proportional to the change in the two-thirds power of the velocity of the projectile. Both extrapolation limit lines were faired to match the upper end of the test data. None of these extrapolations has been verified from laboratory data. Until reliable tests are conducted at these velocities, the designer must select an extrapolation based on other factors than those established under this program.

NUMERICAL EXAMPLE

The solution of a sample problem is shown in Figure 46. The example falls within the laboratory test range; the predicted configuration was tested and found adequate. The steps outlined are general and may be applied at any velocity.

Assume that a three-sheet configuration is desired. The design particle diameter is $D = 0.25$ inch; the design velocity is 20,000 feet per second. The shield thickness and spacing are 0.040 inch and 2.5 inches, respectively, and the second sheet is 0.020-inch thick. It is required to find t_3 such that the three-element barrier will stop the design particle. The arrows indicate that the chart is entered for the following values of the nondimensional ratios: $V/C = 1.2$, $t_1/D = 0.16$, and $S_1/D = 10$.

The diagram indicates that for $t_2/D = 0.08$, the number of sheets penetrated (not including the shield) is 3.4. This exceeds the desired number, since at this point the configuration consists of a shield (0.040-inch thick), a second sheet (0.020-inch thick), plus 2.4 more sheets, each of which is 0.020-inch thick. The final 2.4 sheets must now be transformed into a single sheet of equivalent penetration resistance. Hence, for the second cycle, the chart is entered at $N = 2.4$ and $t_2/D = 0.08$. By noting that horizontal lines represent lines of equal protection capability, it is seen that moving horizontally from the intersection of $N = 2.4$ and $t_2/D = 0.08$ to the $N = 1$ line yields $t/D = 0.36$. Therefore, $t_3/D = 0.36$ and $t_3 = 0.090$ inch.

In the preceding example it was assumed t_1, S_1, and t_2 had been fixed by other operational considerations. If no constraints had been placed on these variables, a lighter structure could have been designed. The minimum-weight, two- and three-sheet combinations for a given spacing and velocity extrapolation are shown in Figures 47 and 48.

MODULE DESIGN

The steps required to design meteoroid shielding for a cryogenic propulsion module are demonstrated through several examples applied to specific mission requirements.

The particle is selected using the Figure 45 nomogram as previously described. From a meteoroid protection standpoint, the primary structure, Figure 49, consists of two aluminum sheets. The inner and outer sheet thicknesses are 0.040 and 0.020 inch, respectively, and the separation is 3.4 inches. This will be sufficient protection for small particles, but an outer shield is required for larger particles. To determine the actual thicknesses required, the nomogram of Figure 46 is used. An extrapolation of the velocity effect must be selected prior to using the nomogram. The most conservative (lower curve) becomes proportional to the cube root of the projectile kinetic energy and is used in this design example.

Assuming a particle velocity of 100,000 feet per second and a desired two-sheet configuration, enter Figure 46 at a number of t_1/D values for several spacings. Read off the required $t_2/D (N = 1)$ for each pair of t_1/D and S_1/D values. A plot of t_1/D vs $t_1/D + t_2/D$ is shown in Figure 47. Draw a line through the minimum $t_1/D + t_2/D$ values for each S_1/D. This line represents the lightest total barrier weight for the selected spacings. If a three-sheet barrier is being designed, the same procedure is followed (for $t_2 = t_3$), except that $N = 2$ on the chart. A plot of t_1/D vs $t_1/D + t_2/D + t_3/D$ is shown in Figure 48.

To continue with the example, assume a two-sheet barrier and a probability of no penetration of 0.9999. For the cryogenic module shown in Figure 49, the exposure, $A\tau$, is 1.56 by 10^5 feet^2-hours. For a particle density of 0.5 gram per cubic centimeter, this leads to a particle diameter of 0.27 inch (see Figure 45). It is assumed that structural requirements dictate a 2.0-inch spacing and a minimum t_1 and t_2 of 0.020 and 0.040 inch, respectively. Dividing by D gives $S_1/D = 7.4$, $(t_1/D)_{min} = 0.074$, $(t_2/D)_{min} = 0.148$. The minimum curve from Figure 47 (dashed line) indicates that for $S_1/D = 7.4$, t_1/D is approximately 0.188 and $t_1/D + t_2/D$ is 0.900. The best t_2/D value is thus 0.712. Multiplying by D gives $t_1 = 0.051$ inch and $t_2 = 0.192$ inch.

A three-sheet design is accomplished in a similar manner. For example, using the same 0.27-inch diameter particle and assuming an allowable spacing of 5 inches results in $S_1/D = 18.5$. From Figure 48 the best t_1/D value is 0.10 inch and the best $t_1/D + t_2/D + t_3/D$ is 0.37 inch. These result in $t_1 = 0.027$ inch and $t_2 = t_3 = 0.037$ inch. If t_2 and t_3 must be at least 0.020 and 0.040 inch, respectively, due to structural requirements, the design nomogram should now be used to find what t_1 would be required for a $t_2 = 0.020$ inch and a $t_3 = 0.040$ inch. The 0.040-inch sheet must first be converted to an equivalent number of 0.020-inch sheets so that all sheets after t_1 will be of uniform thickness. Enter the nomogram at $N = 1$ and $t_2/D = 0.148$. Move horizontally (constant "protection capability") to $t_2/D = 0.074$. N is seen to equal 1.5. The 0.040-inch sheet is then equal to one and a half 0.020-inch sheets. Now enter the chart at $N = 2.5$ (the equivalent number of 0.020-inch sheets behind t_1) and $t_2/D = 0.074$. Move horizontally to $S_1/D = 18.5$. Drop down to the $V/C = 6$ and the lower velocity extrapolation line. Move diagonally to the t_1/D line. The t_1/D value required is 0.20 so that $t_{1_{min}} = 0.054$ inch. The constraints on t_2 and t_3 result in a 14-percent weight penalty compared to the minimum weight barrier as obtained from Figure 48.

The use of the nomogram to design the above two- and three-sheet barriers is illustrated on the large chart enclosed in the back cover pocket. The effect on barrier design of changing the acceptable risk (probability of no penetration) is tabulated in Figure 49 for both two- and three-sheet barriers.

A general discussion of the effects of using insulative materials within the meteoroid barrier has been given previously. A design procedure has been verified for glass-wool insulation and aluminum sheets. The procedure is the same as used for no insulation except that penetration is modified by a factor K. That is, penetration with filler, N_f, and penetration without filler, N_o, are related by:

$$N_f = K\ N_o \qquad (18)$$

The factor K is calculated from the following equation:

$$K = 1 - 0.9\ S_f/D \left[1 + 113\ (\rho_f/\rho_1)^2 \right] f(V/C) \qquad (19)$$

where $f(V/C)$ is given in Figure 32.

CONCLUSIONS AND RECOMMENDATIONS

A unique solution for a meteoroid barrier design does not exist. Many related solutions may be obtained, depending on the order of preference in selection of barrier element material and geometry. In general, it is not profitable to design complex meteoroid barriers by ratioing results applicable to single-sheet or semi-infinite targets. Under this program, an analytical method has been developed that permits the rational design of meteoroid barriers by the sequential selection of barrier elements. Design may be based on a minimum-weight criterion or with full consideration of other vehicle operational constraints, such as volume and size requirements, depth limits, minimum gages, structural loadings, or temperature control.

The use of low-density shield materials results in the lightest meteoroid barriers where the design criterion is based on complete resistance to penetration. Where some small punctures may be permitted, high-density shield materials may offer some weight advantages.

Since shield fragments are a major contributor to inner-element damage, the outer shield thickness must be chosen to minimize total damage. Total barrier depth for aluminum elements (especially the spacing between the first two elements) is the single parameter having the greatest effect on weight. It can be shown, however, that a maximum depth exists beyond which any further increase is not useful.

Penetration damage is strongly affected by projectile material and density. The factor of most importance in correlating damage from various projectiles is the transverse diameter of the impacting particle.

The hazards of velocity extrapolation for impact into semi-infinite plates have been thoroughly explored. Simple extrapolation based on particle momentum or energy does not appear to fit penetration through multisheet or composite barriers, at least over the velocity range tested. Despite this, an extrapolation proportional to the cube root of projectile kinetic energy has been provided in the design nomogram (Figure 43).

Significant advances have been made in the present program toward solving meteoroid-shielding-design problems. Some additional testing and analysis are required, however, to obtain solutions to all of the problems in the areas studied. Recommendations for additional studies are discussed in the following paragraphs.

During the present program, projectiles of aluminum, aluminum oxide, Pyrex, Lexan, magnesium-lithium, foamed aluminum, and foamed nickel were tested. The primary projectile was aluminum; relatively few of the other projectiles were tested. To predict the effect of projectile density and material, a test program should be conducted in which projectiles of different materials are tested. Projectiles of the same material but varying density should also be included. The projectiles should be fired at several velocities into similar targets.

The effect of impact by low-density projectiles should be investigated. Comparison of the data on impact by plastic and aluminum projectiles has indicated that, at high velocities, damage trends may be more severe when testing with low-density projectiles.

The results of the present program have been based on tests in which the velocity was varied from 5000 to 27,000 fps; the major portion of the data was obtained at velocities from 18,000 to 25,000 fps. Some of these tests should be repeated at higher velocities to have a broader base upon which to extrapolate velocity effects into the meteoroid range. Test velocities in excess of 30,000 fps would be useful.

A series of tests was performed in which specimens, loaded uniaxially and biaxially, were impacted at cryogenic temperature. The aluminum specimens (2219-T62 and 2014-T6) were impacted by aluminum projectiles and/or the fragments from aluminum shields (2014-T6 and 7075-T6). Other specimen materials and/or other shield materials might give different results. A significant number of additional tests should be made to investigate other cryogenic tankage materials over the anticipated range of operational temperatures.

The confinement offered by panel constraint needs to be investigated for a range of structural supporting systems. This includes skin and stringer, corrugated stiffener, and honeycomb structural arrangements.

REFERENCES

1. Bjork, R. L., "Review of Physical Processes in Hypervelocity Impact and Penetration," Part 1, Volume II, Proceedings of the Sixth Symposium on Hypervelocity Impact, Cleveland, Ohio, August 1963.
2. Walsh, J. M. and J. H. Tillotson, "Hydrodynamics of Hypervelocity Impact," Part I, Volume II, Proceedings of the Sixth Symposium on Hypervelocity Impact, Cleveland, Ohio, August 1963.
3. Riney, T. E., "Visco-Plastic Solution of Hypervelocity Impact Cratering Phenomenon," Part 1, Volume II, Proceedings of the Sixth Symposium on Hypervelocity Impact, Cleveland, Ohio, August 1963.
4. Eichelberger, R. J., "Summary: Theoretical and Experimental Studies of Crater Formation," Part 2, Volume II, Proceedings of the Sixth Symposium on Hypervelocity Impact, Cleveland, Ohio, August 1963.
5. Kinard, W. H., C. H. Lambert, Jr., D. R. Schryer, and F. W. Casey, Jr., "Effect of Target Thickness on Cratering and Penetration of Projectiles Impacting at Velocities to 13,000 Feet per Second," NASA Memo 10-18-58L, 1958.
6. Whipple, F. L., "Meteoritic Phenomena and Meteorites," Physics and Medicine of the Upper Atmosphere, University of New Mexico Press, Albuquerque, 1952, pp. 137-170.
7. Olshaker, A., "An Experimental Investigation in Lead of the Whipple Meteor Bumper," Fourth Hypervelocity Impact Symposium, Volume 2, April 1960. (M.S. Thesis, Massachusetts Institute of Technology, June 1960.)
8. Nysmith, C. R. and J. L. Summers, "An Experimental Investigation of the Impact Resistance of Double-Sheet Structures at Velocities to 24,000 fps," NASA TN D-1431, October 1962.
9. Klahr, C. N. and N. N. Stein, "Active Shielding Against Meteoroids," Report No. ASD-TDR-63-537, August 1963.
10. NASA TN D-1504, "A Report on the Research and Technological Problems of Manned Rotating Spacecraft," August 1962.
11. Frost, V. C., "Aerospace Meteoroid Environment and Penetration Criteria," Report No. TDR-269(4560-40)-2, August 17, 1964.
12. Lee, D. H. and G. T. Burch, Jr., "Impact Penetration to Spacecraft Cabins," The Boeing Company, D2-23083, April 15, 1964.
13. Stepka, F. S. and C. R. Morse, "Preliminary Investigation of Catastrophic Fracture of Liquid-Filled Tanks Impacted by High-Velocity Particles," NASA TN D-1537, May 1963.

14. Lundeberg, J. F., G. T. Burch, and D. H. Lee, "Hypervelocity Impact Failure of Pressure Vessels," Report No. ATL-TR-64-82, December 1964 (Confidential).

15. "Liquid Propellant Losses During Space Flight," Contract No. NASw-615 Final Report, Arthur D. Little, Inc., October 1964.

16. Hawkins, G. S., "The Meteor Population," Radio Meteor Project Research Report No. 3, NASA Contract NASr-158, Harvard College Observatory, Smithsonian Astro-Physical Observatory, August 1963.

17. Whipple, F. L., "On Meteoroids and Penetration," Journal of Geophysical Research, Volume 68, No. 17, September 1, 1963, pp. 4929-4939.

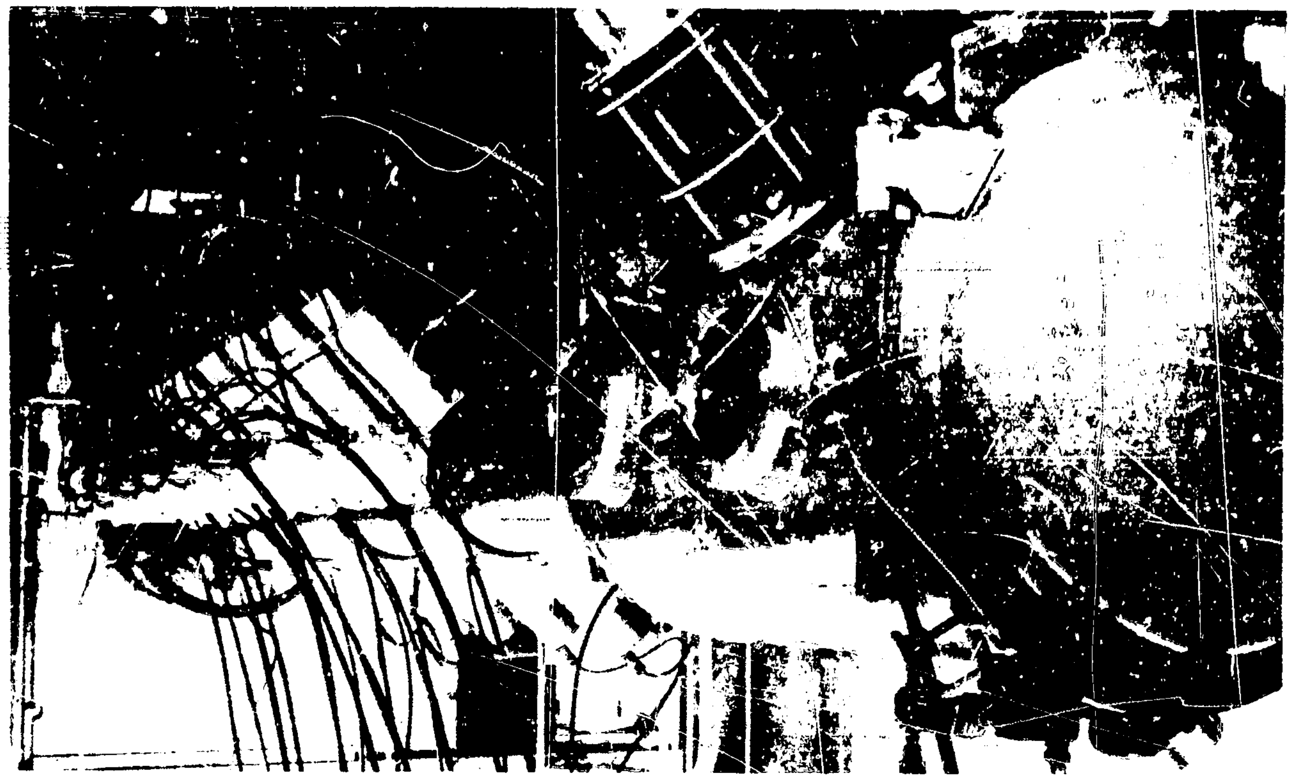

(a) BREECH, PUMP TUBE, HIGH-PRESSURE ADAPTER, AND BLAST TANK

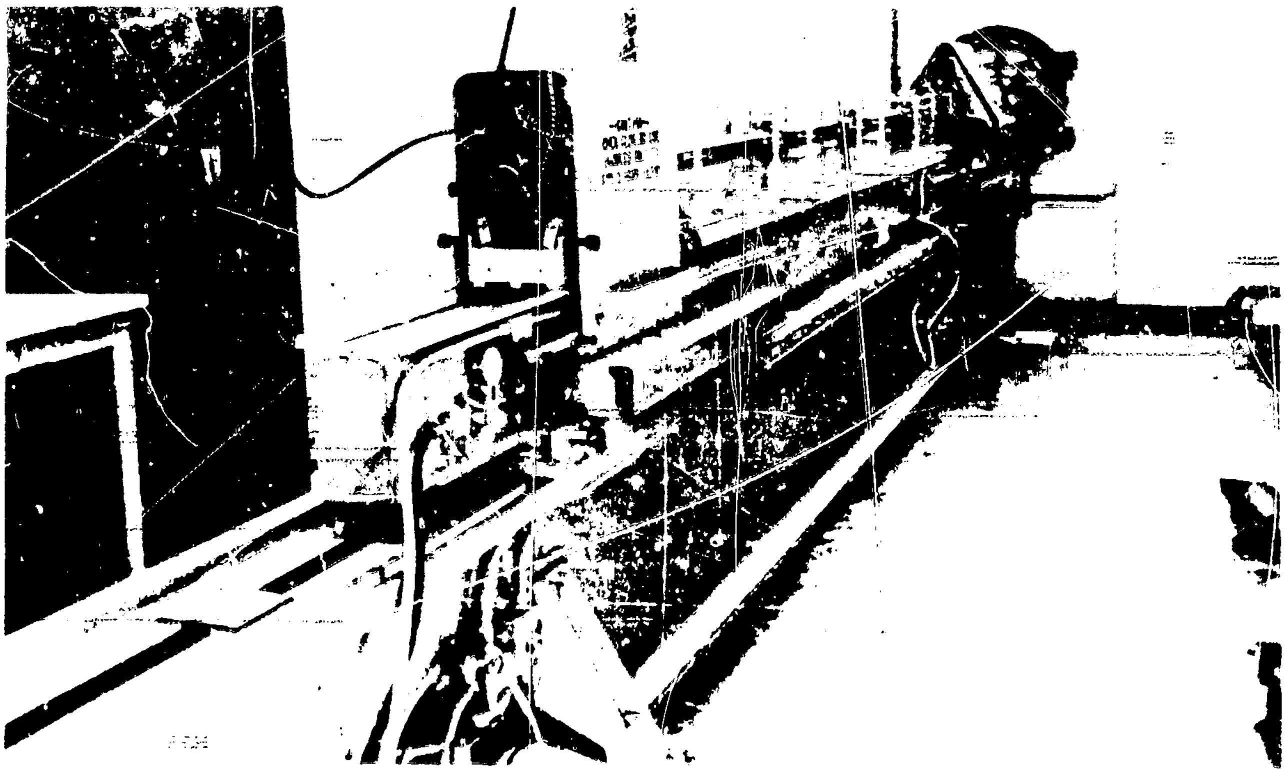

(b) INSTRUMENTATION SECTION AND TEST CHAMBER

Figure 1: BOEING LIGHT-GAS GUN — 1/4-INCH BORE

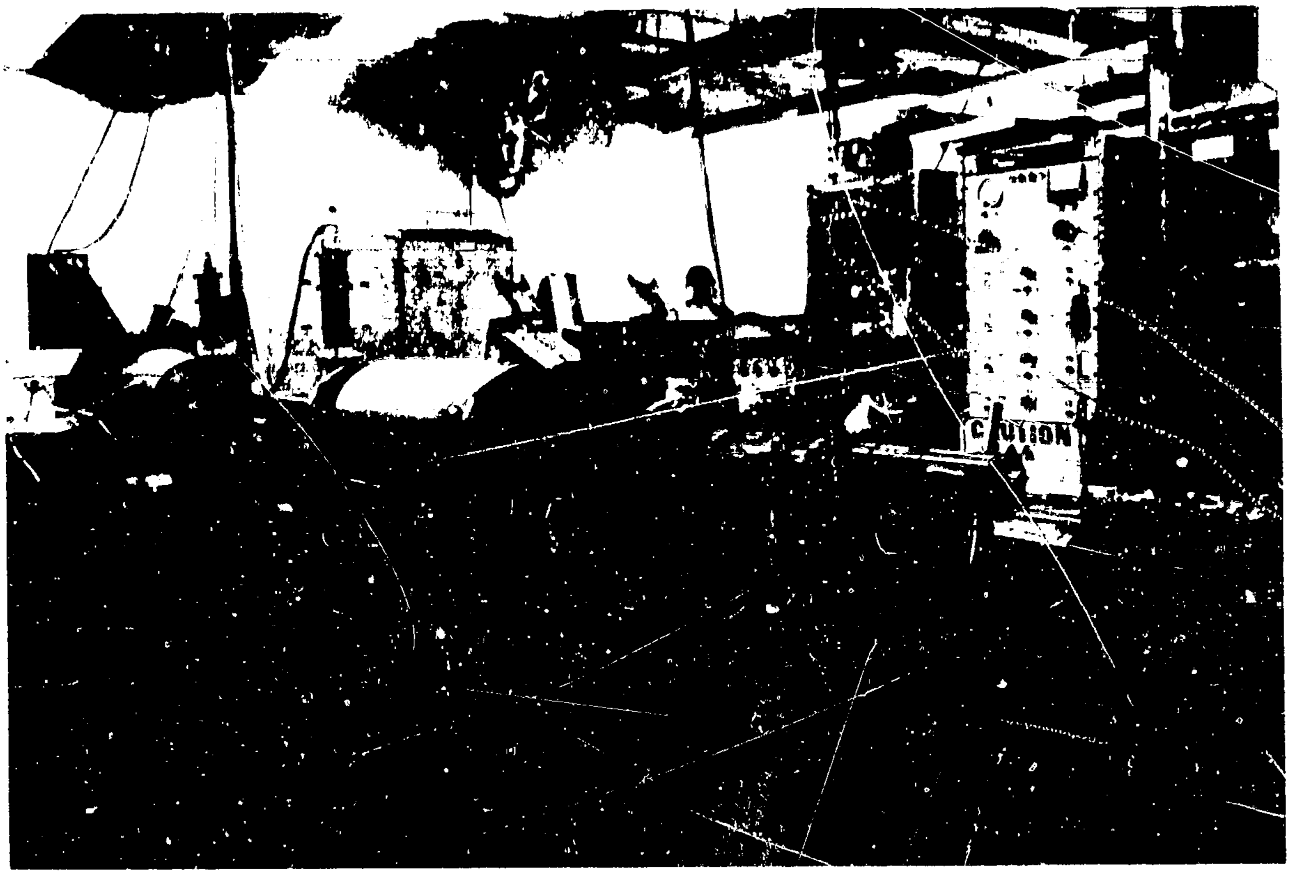

Figure 2: BOEING LIGHT-GAS GUN—1/16-INCH BORE

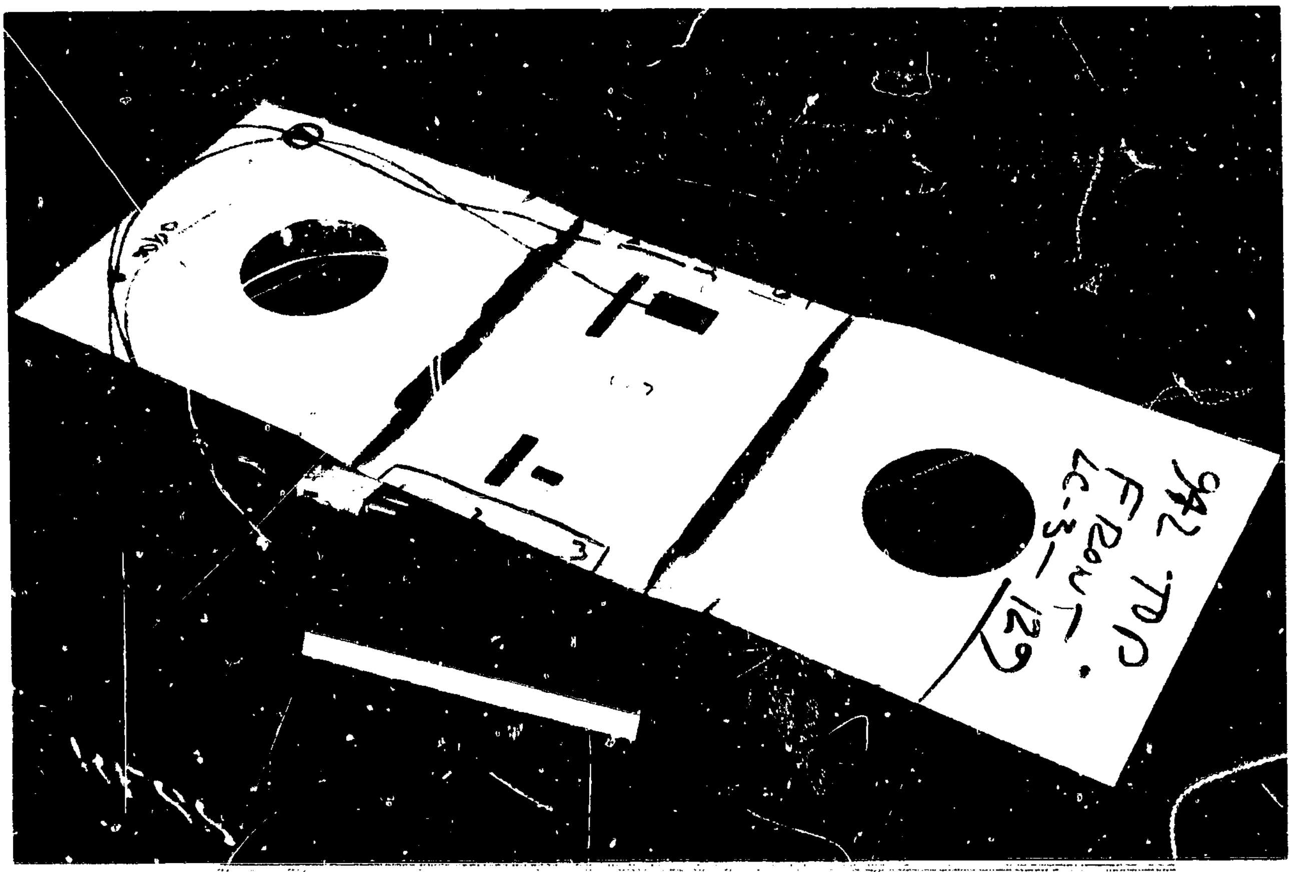

Figure 3: UNIAXIAL-STRESS SPECIMEN

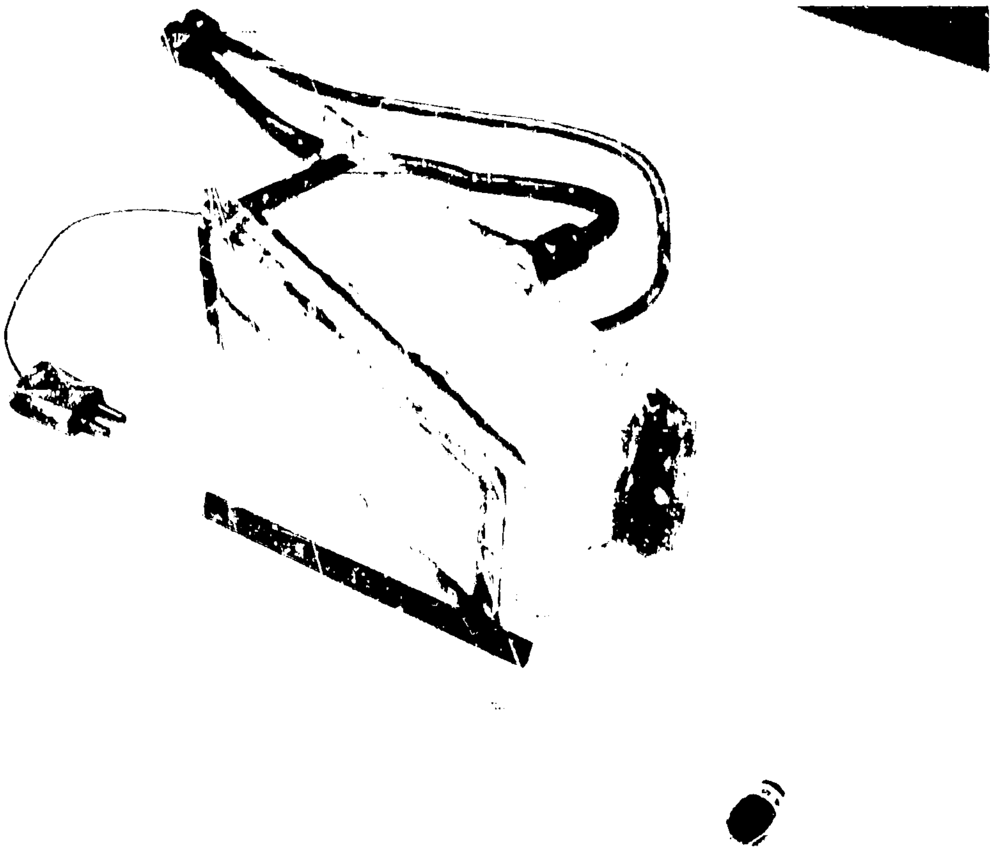

Figure 4: COLD BOX

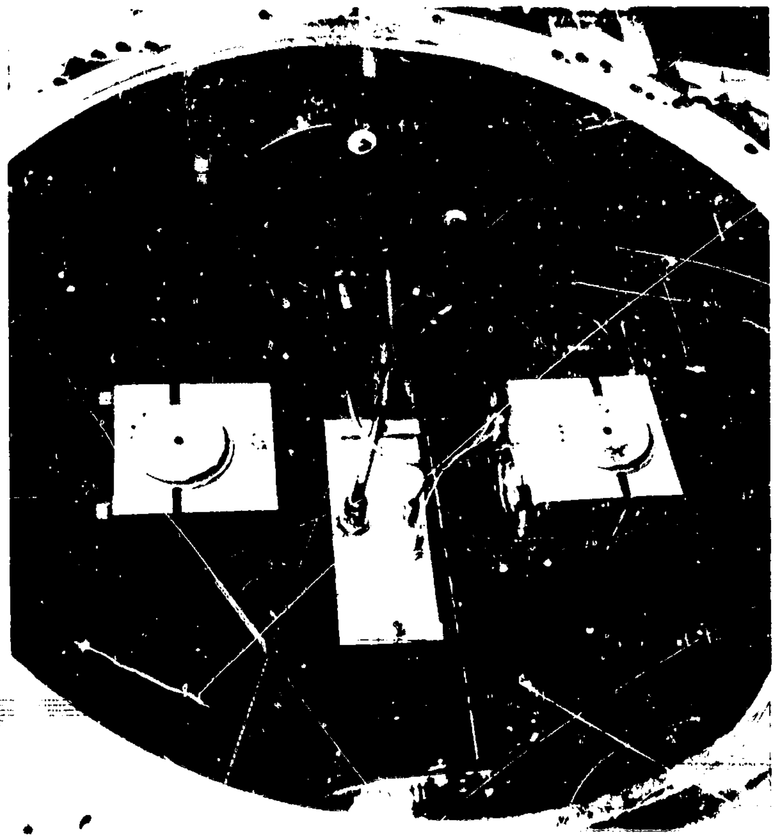

Figure 5: LOADING FIXTURE AND COLD BOX

TYPES OF DAMAGE

(1) First-Sheet Hole Diameter (d)

(2) First Witness Sheet

  (A) $\gamma_1 = \frac{2r_1 - d}{2S_1}$ = Major Damage Spray Angle

  (B) $\gamma_2 = \frac{2r_2 - d}{2S_1}$ = Perforation Spray Angle

  (C) Hole Area = "Hole Cut"

(3) N = Number of Witness Sheets Penetrated

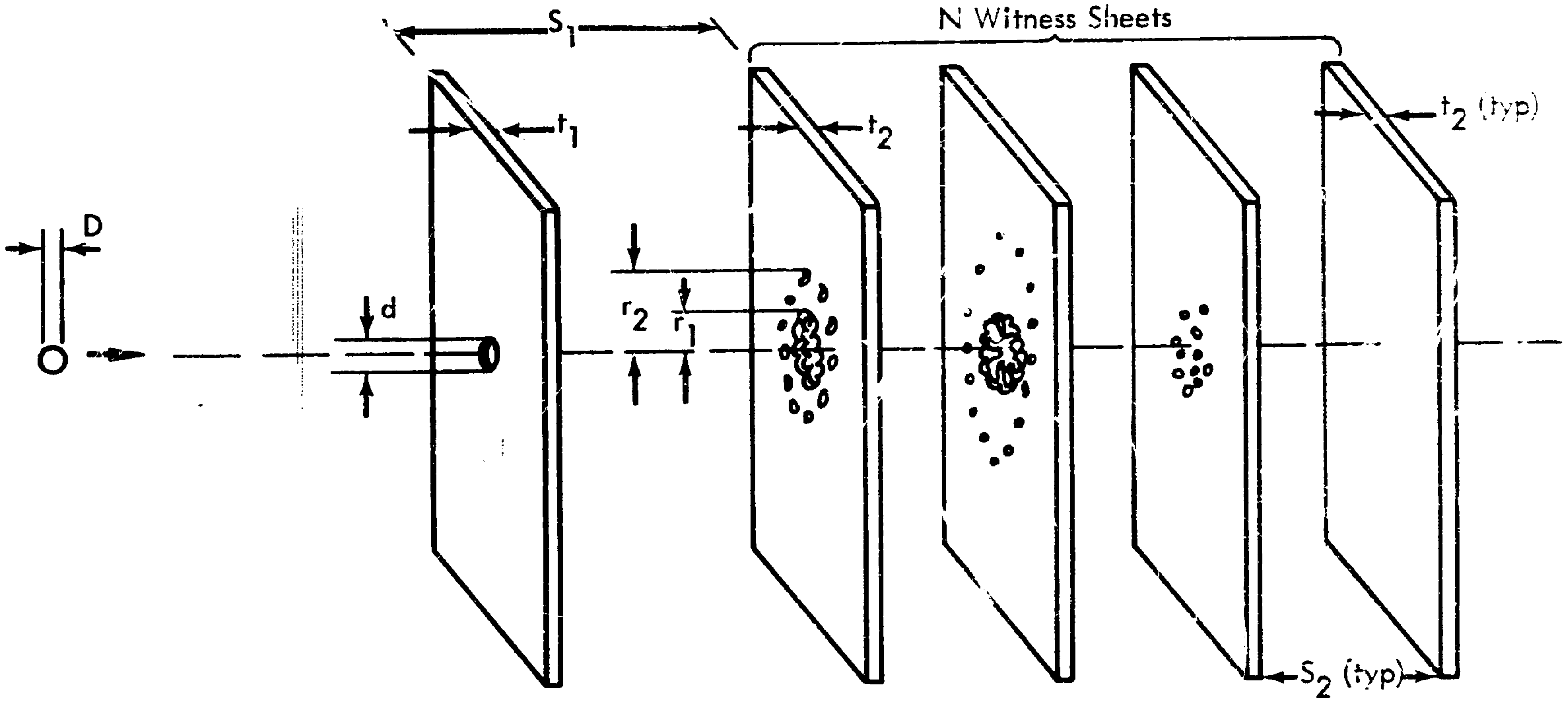

Figure 6: TYPES OF DAMAGE TO MULTIPLE-SHEET TARGETS

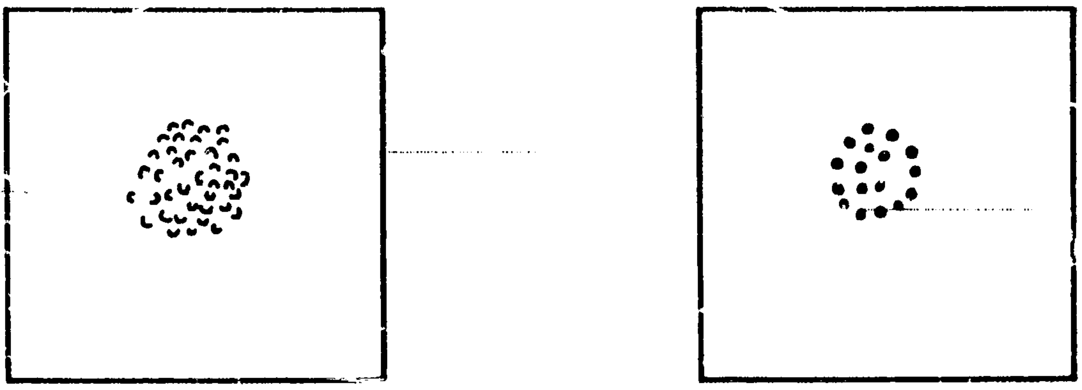

CRATERS ONLY

PINHOLES

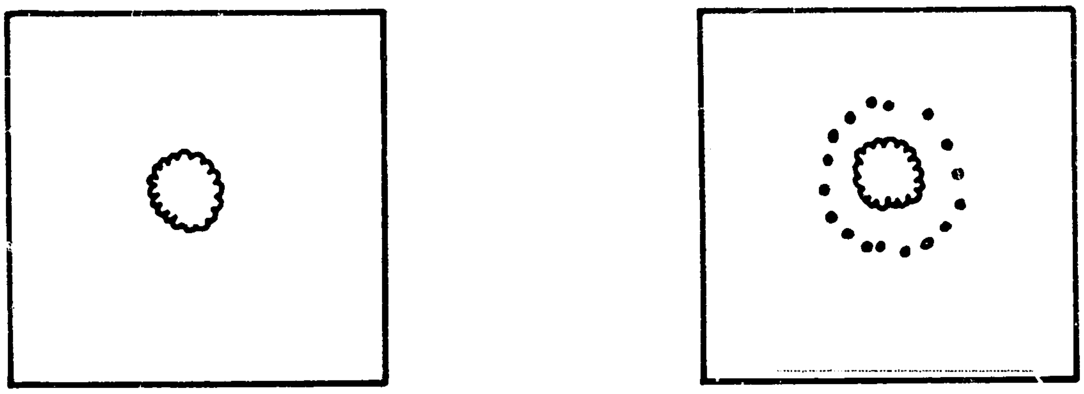

SCALLOPED HOLE

SCALLOPED HOLE
AND PINHOLES

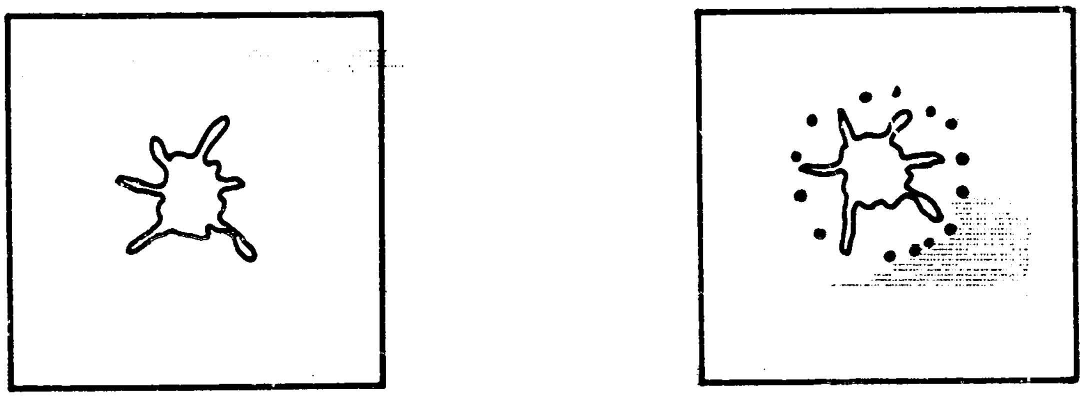

PETALLED HOLE

PETALLED HOLE
AND PINHOLES

Figure 7: DAMAGE PATTERNS ON FIRST WITNESS SHEET

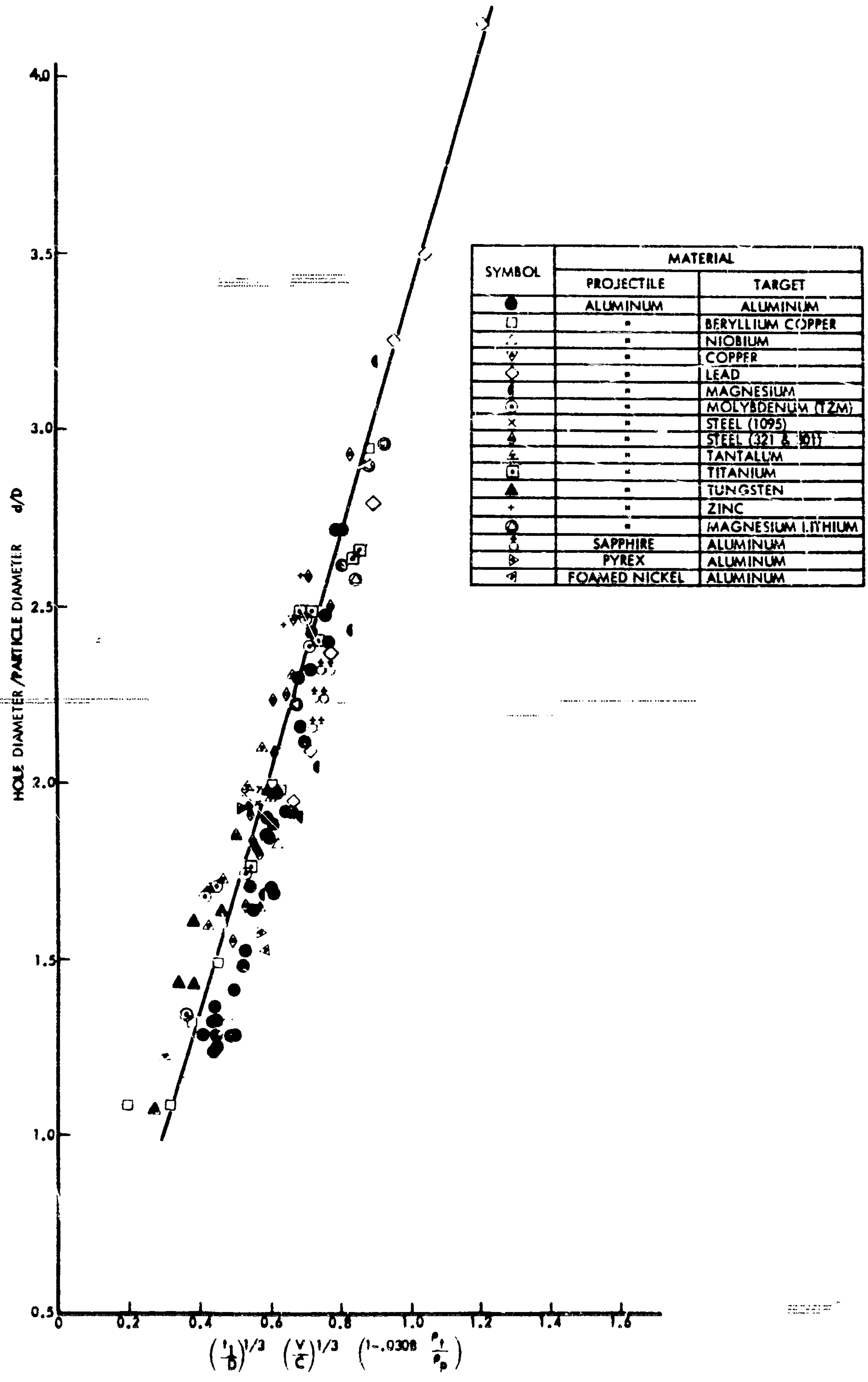

Figure 8: SHIELD DAMAGE

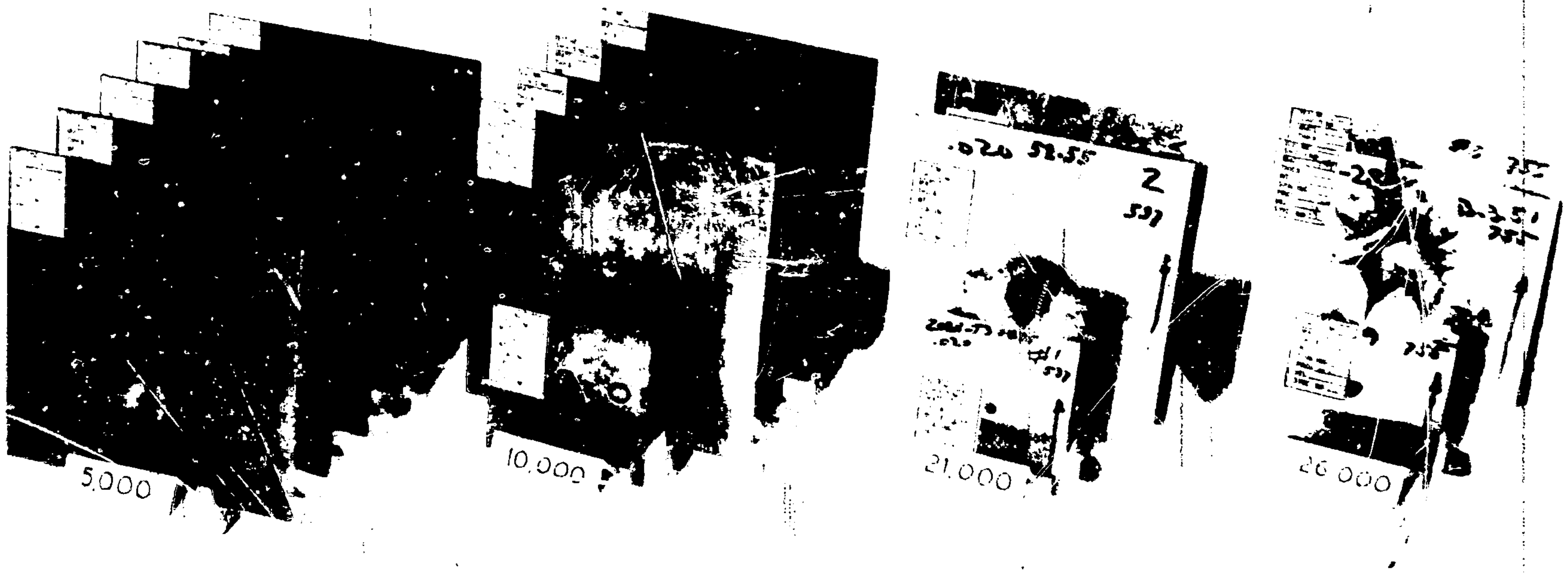

Figure 9: EFFECT OF PROJECTILE VELOCITY ON PENETRATION

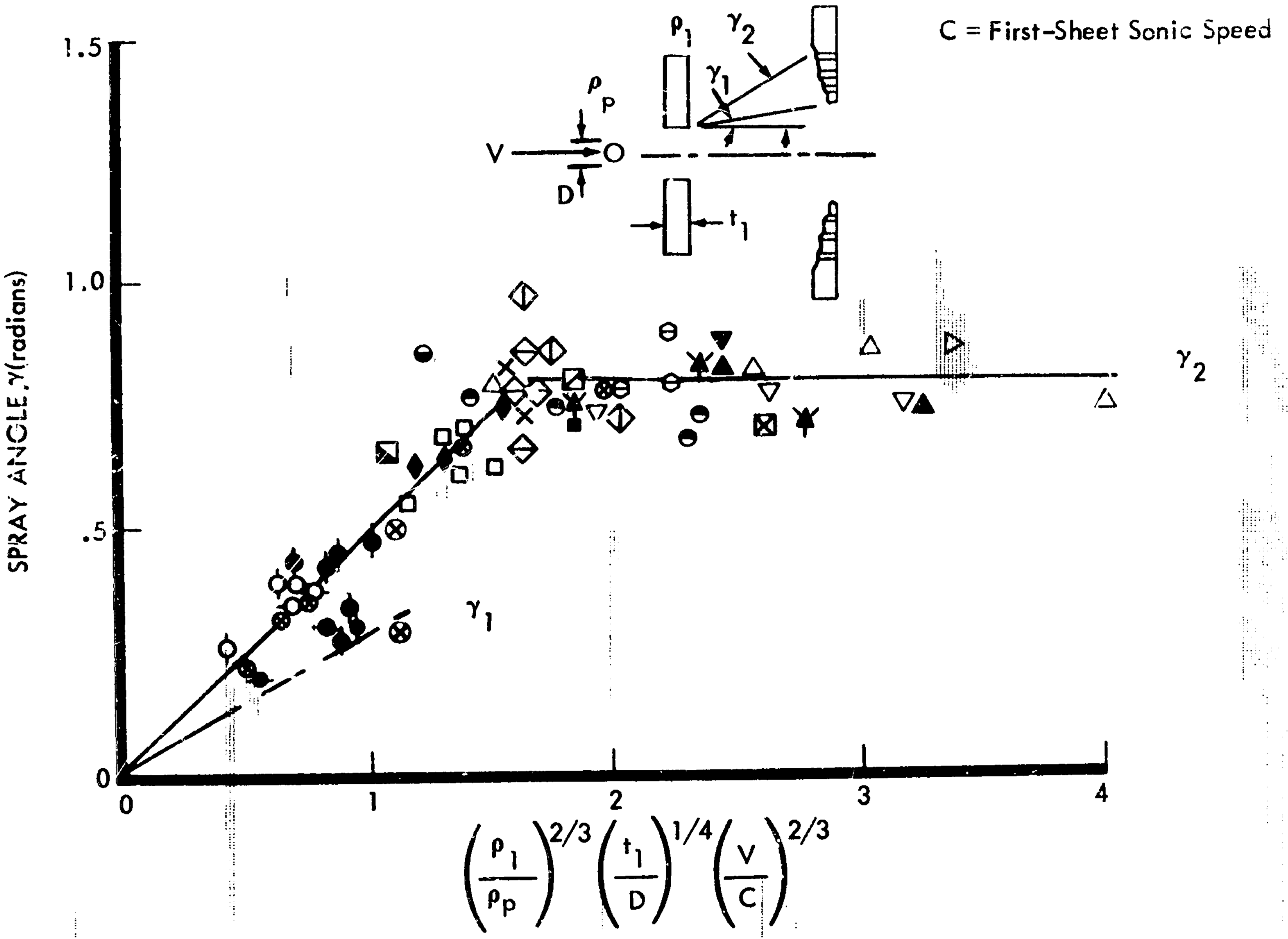

Figure 10: FRAGMENT DISPERSION

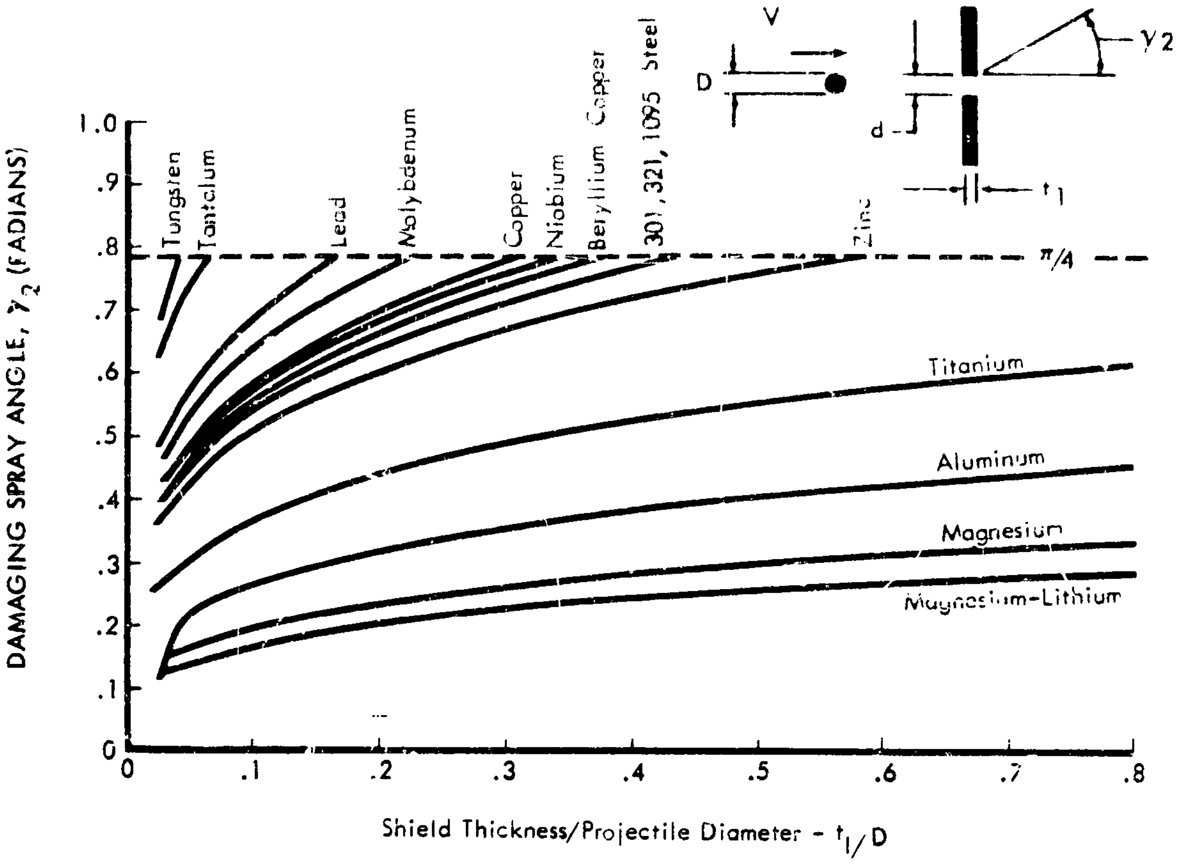

Figure 11: EFFECT OF DENSITY ON SPRAY ANGLE

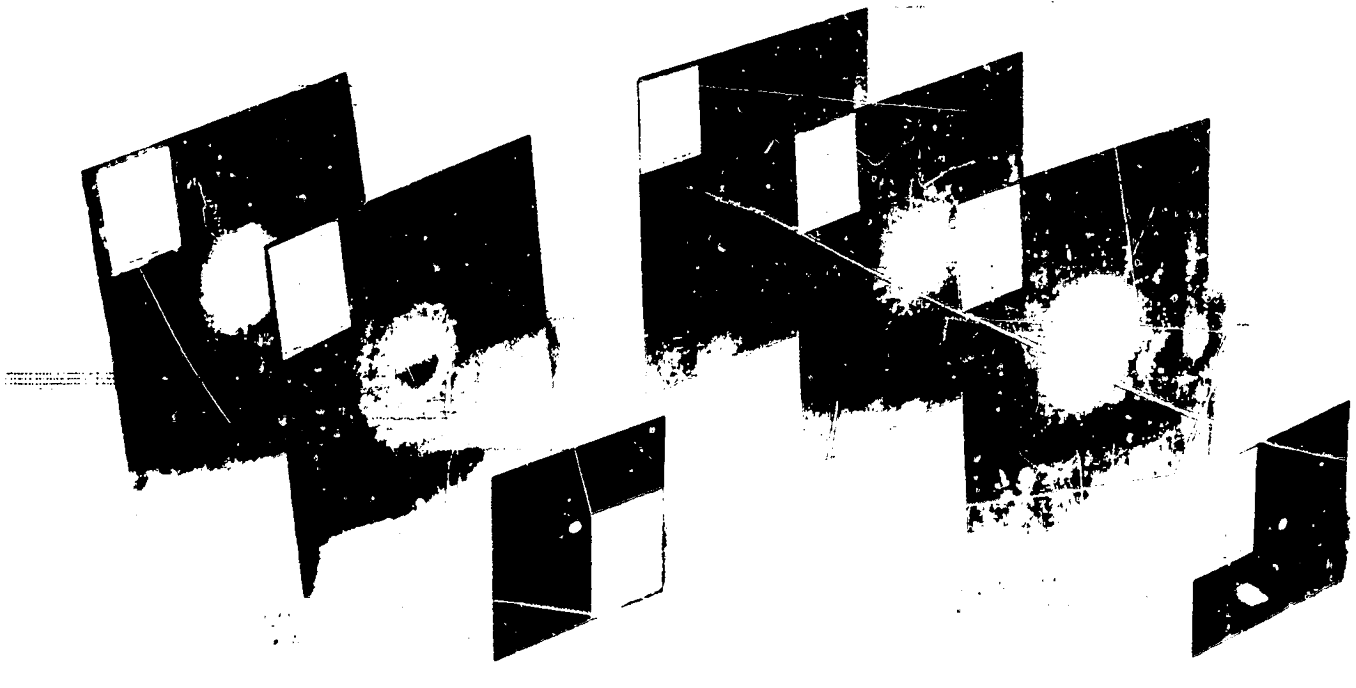

Figure 12: DAMAGE PATTERNS FOR MAGNESIUM-LITHIUM AND TANTALUM SHIELDS

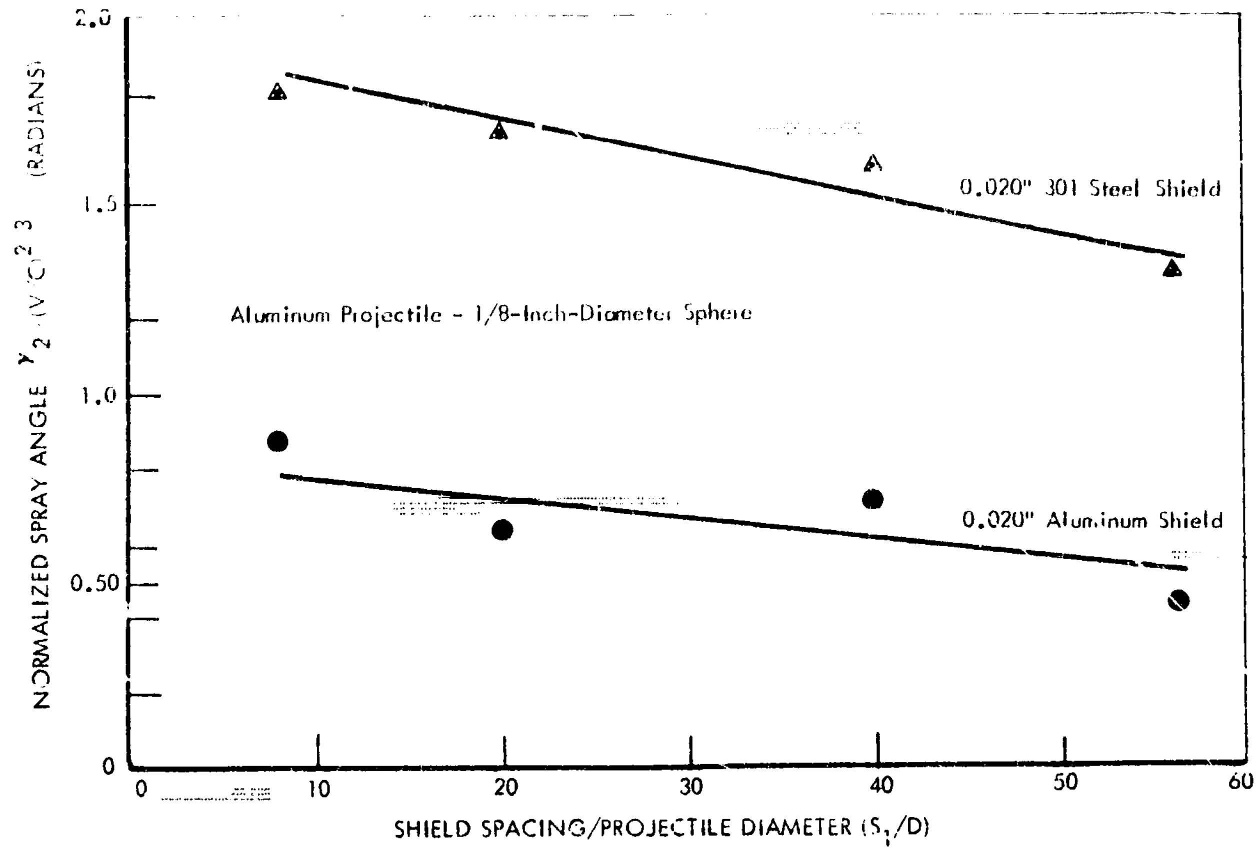

Figure 13: EFFECT OF SHIELD SPACING ON SPRAY ANGLE

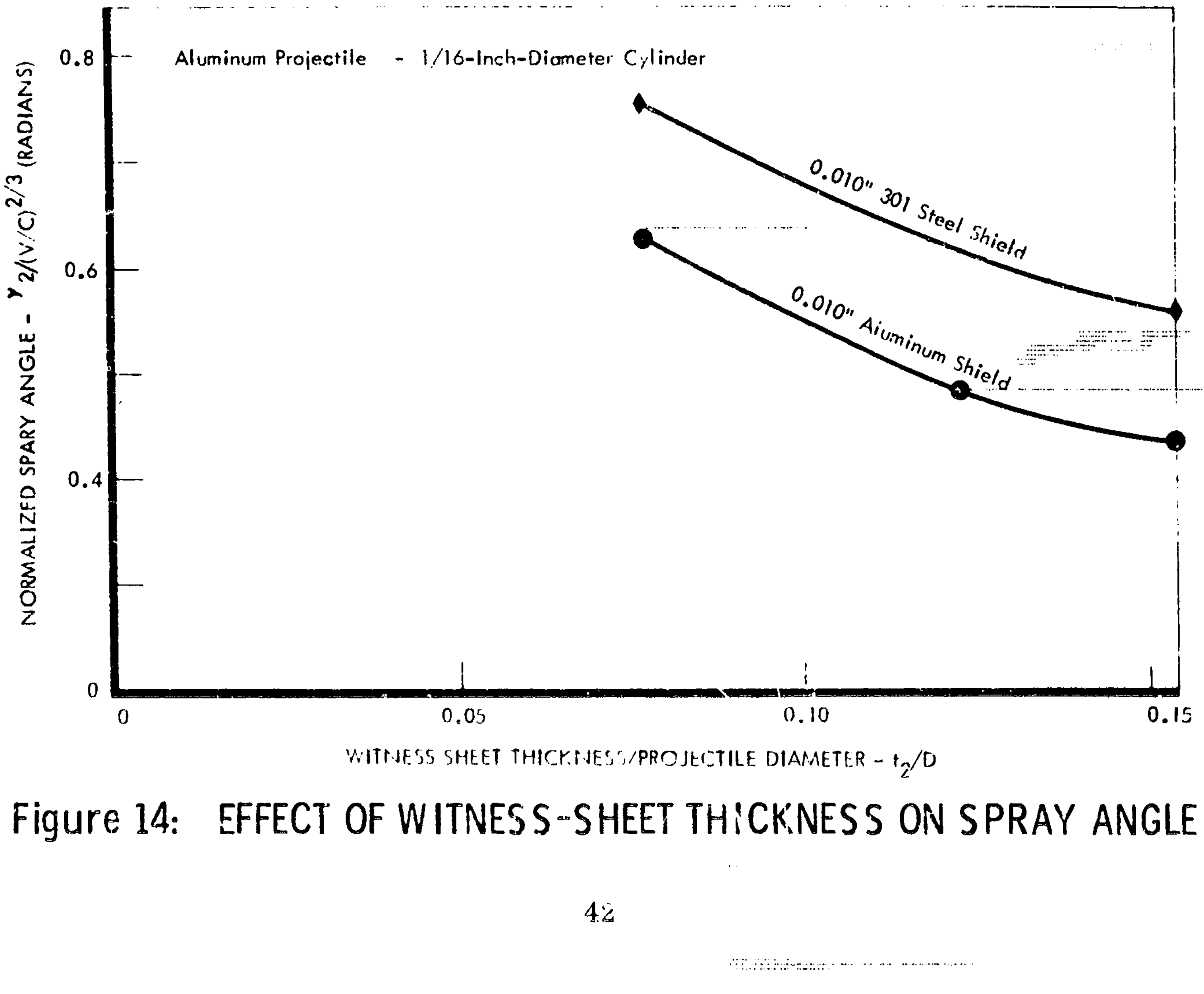

Figure 14: EFFECT OF WITNESS-SHEET THICKNESS ON SPRAY ANGLE

Figure 15: ALUMINUM SHEET ARRAY

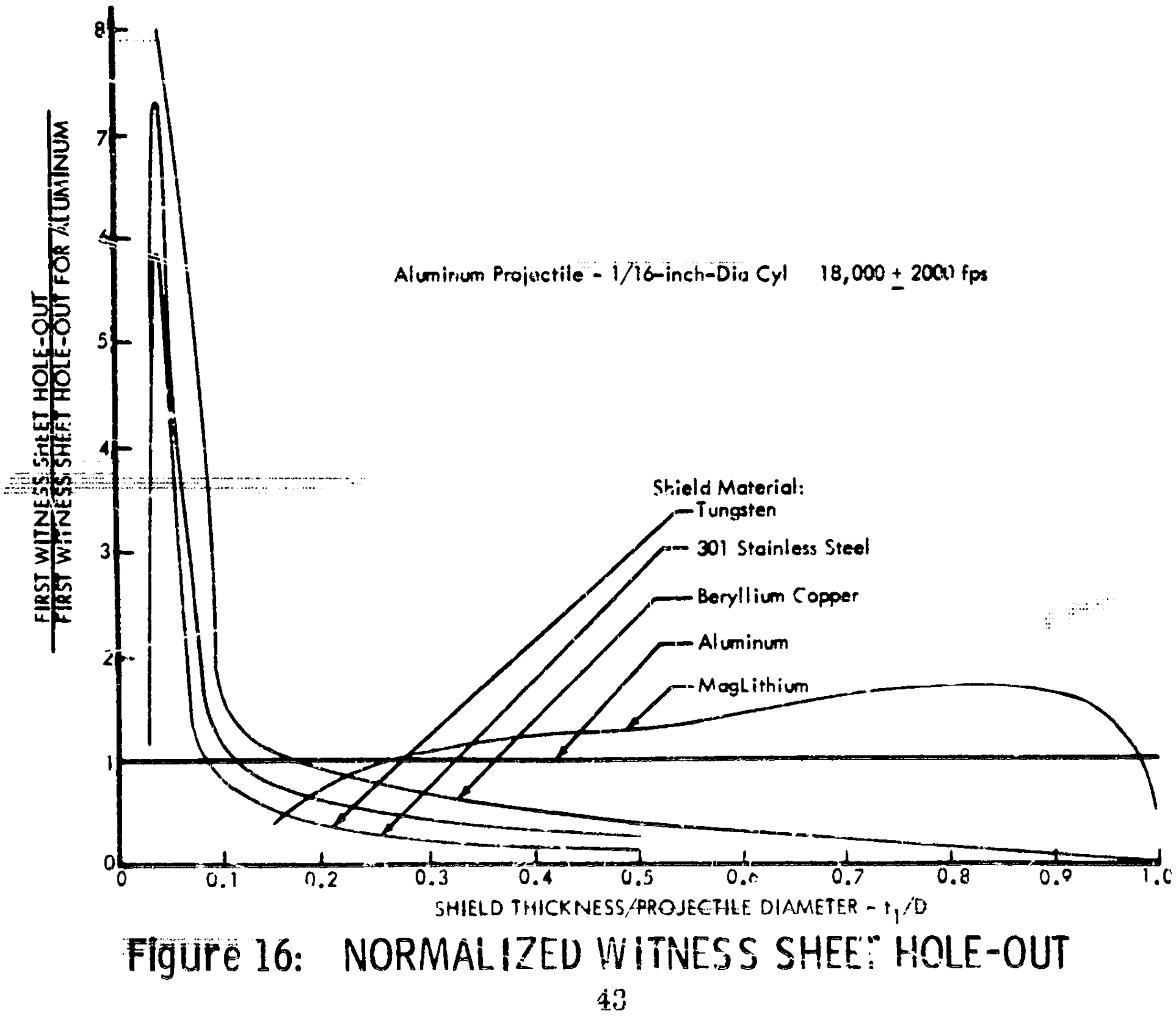

Figure 16: NORMALIZED WITNESS SHEET HOLE-OUT

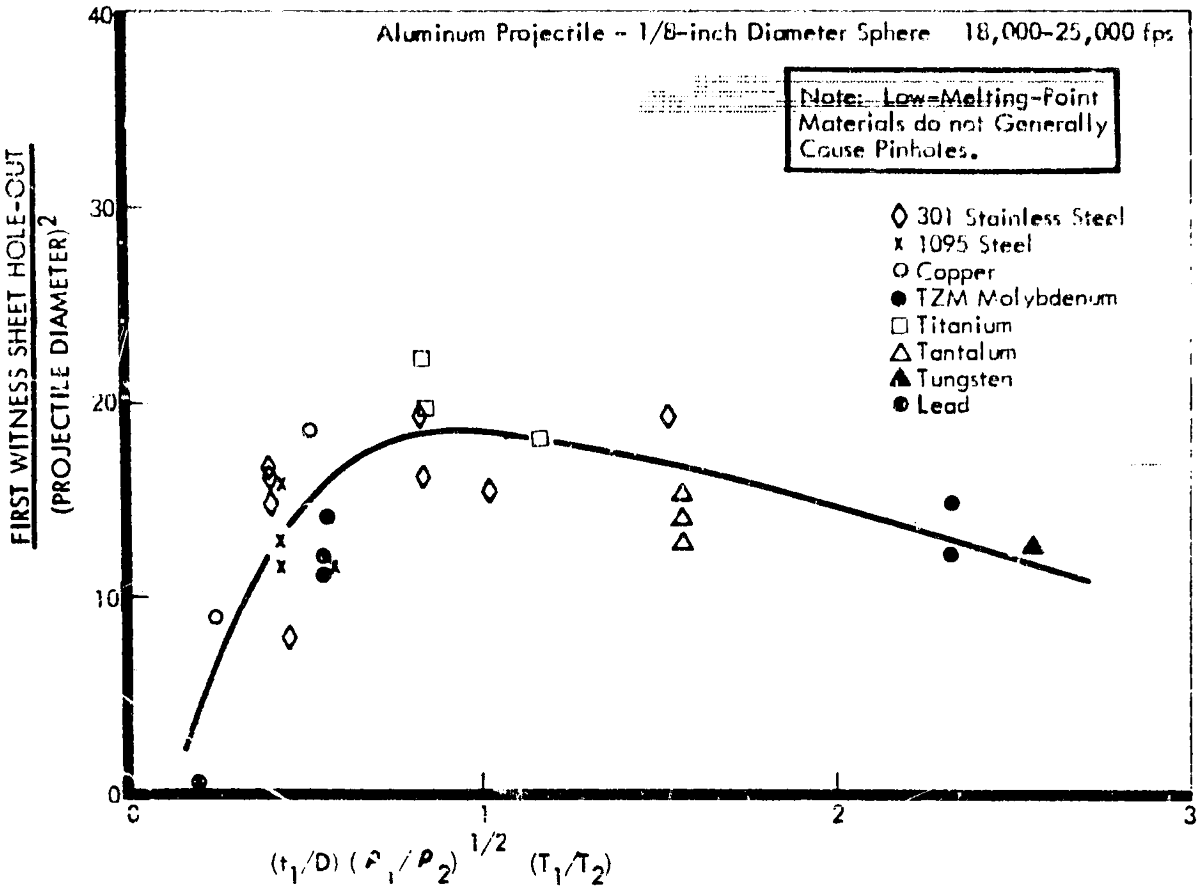

Figure 17: FIRST WITNESS-SHEET PINHOLE AREA

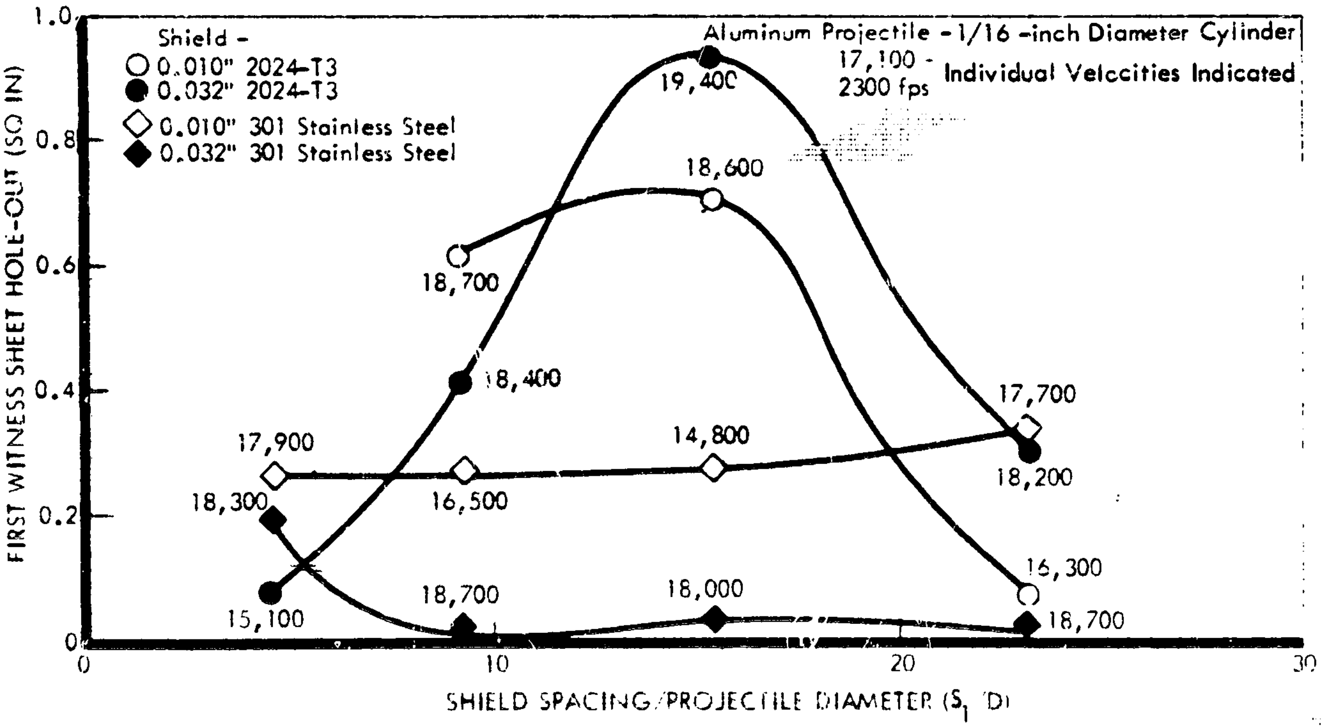

Figure 18: EFFECT OF SHIELD SPACING ON HOLE-OUT

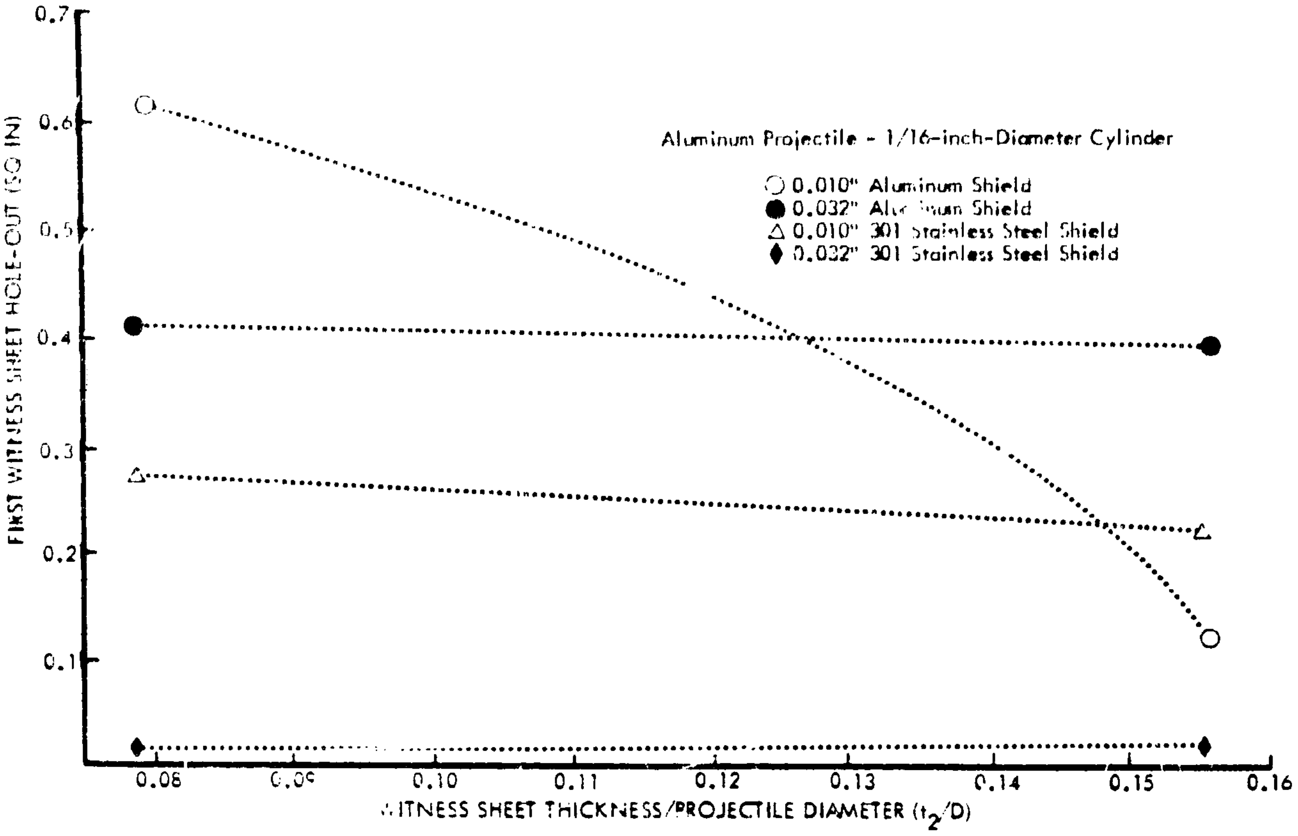

Figure 19: EFFECT OF WITNESS-SHEET THICKNESS ON HOLE-OUT

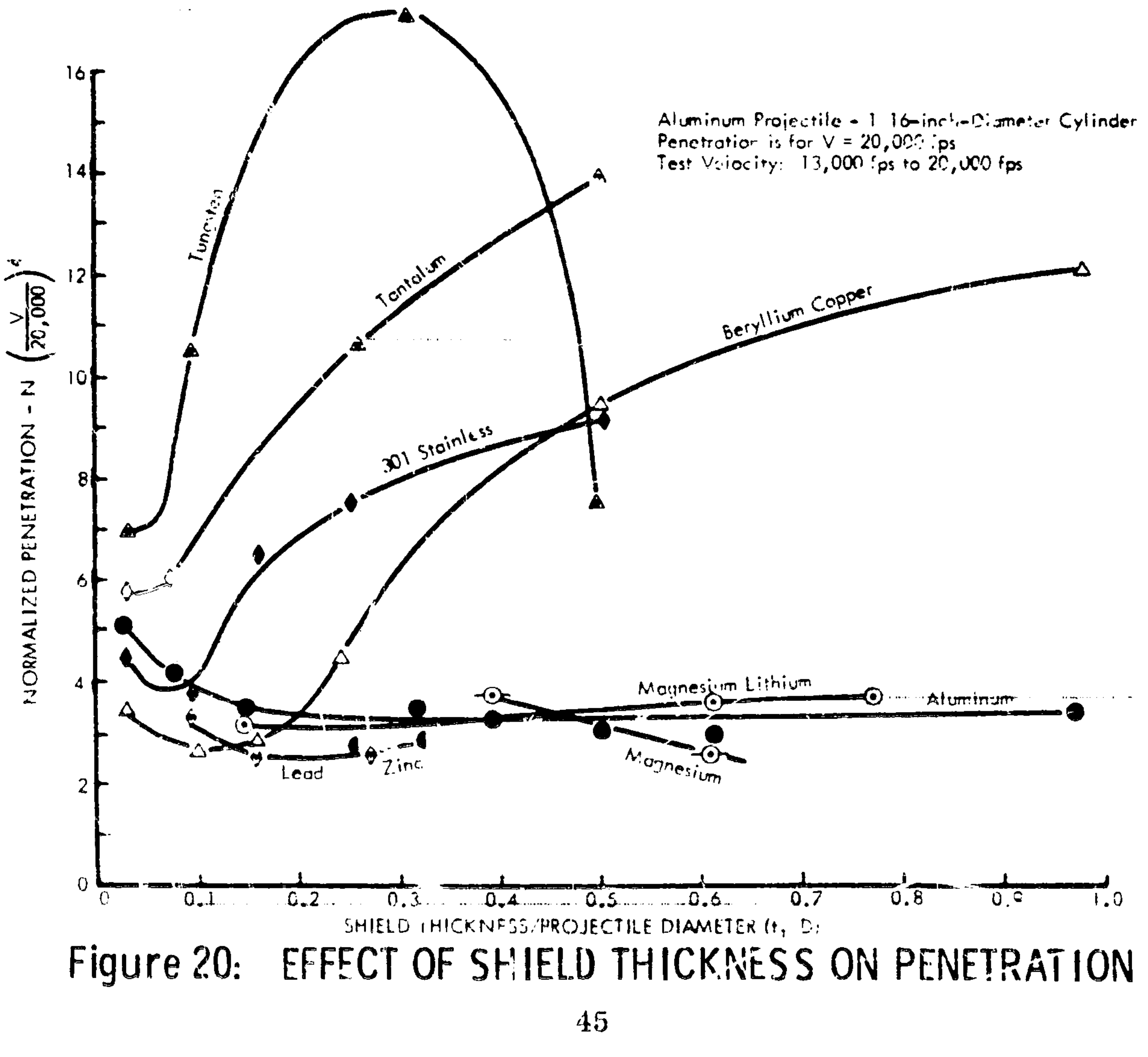

Figure 20: EFFECT OF SHIELD THICKNESS ON PENETRATION

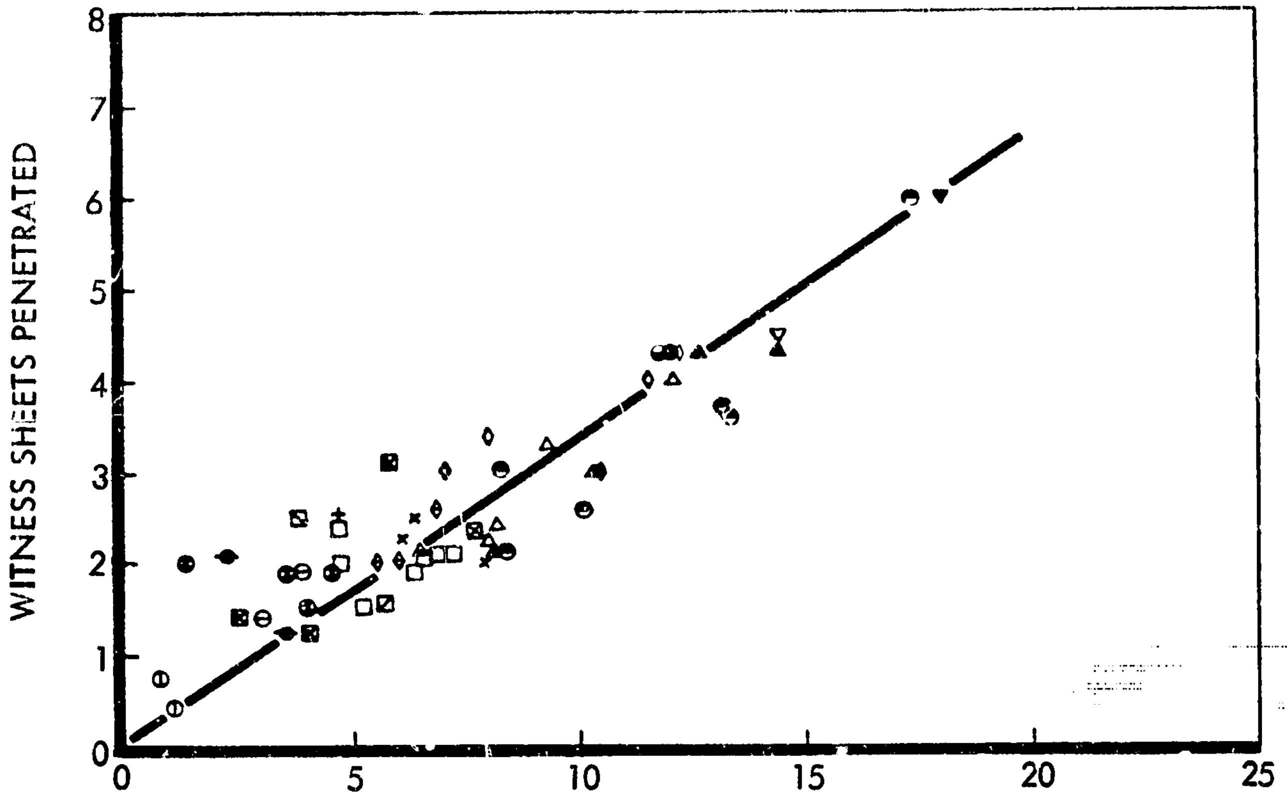

$$\left(\frac{T_1+T_p}{T_2}\right)\left(\frac{\rho_1+\rho_p}{\rho_2}\right)^{1/2}\left(\frac{t_1}{t_2}\right)^{1/3}\left(\frac{V}{C}\right)^{-4/3}\left(\frac{D}{t_2}\right)^{1/4}$$

See Symbol Index at Beginning of Report

T_1 = Melting Temp. of Target Sheet
T_p = Melting Temp. of Projectile
T_2 = Melting Temp. of Witness Sheets
ρ_1 = Density of Target Sheet
ρ_p = Density of Projectile
ρ_2 = Density of Witness Sheets
t_1 = Thickness of Target Sheet
t_2 = Thickness of Witness Sheets
D = Diameter of Projectile
V = Velocity of Projectile
C = Speed of Sound in Target Sheet

Projectile - 1/16, 1/8, 3/16, 1/4 In. Dia.
Aluminum Spheres or Cylinders
Velocity Range - 15,000 to 25,000 fps

Figure 21: MULTIPLE-SHEET PENETRATION

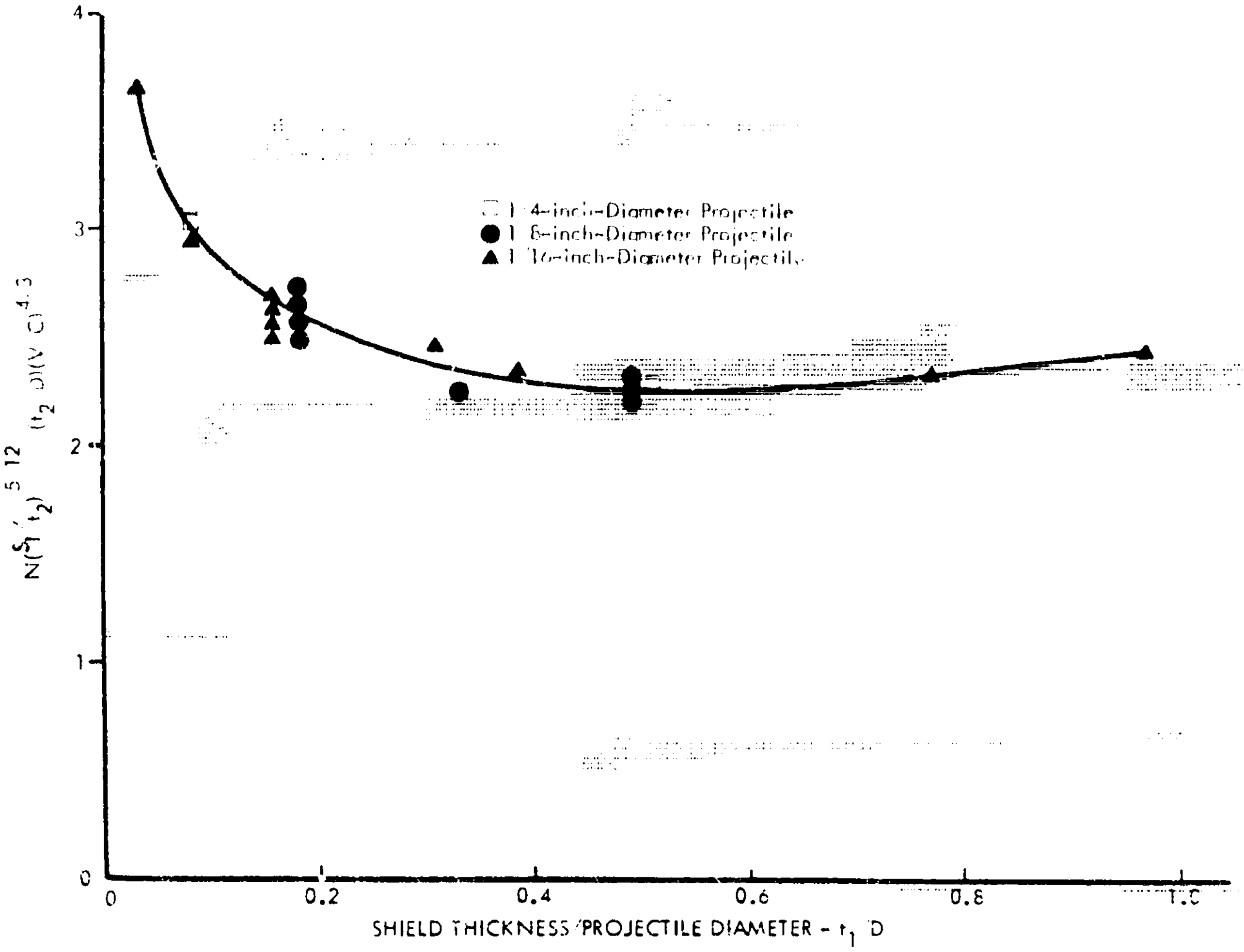

Figure 22: PENETRATION OF ALUMINUM PROJECTILES INTO ALUMINUM SHEETS

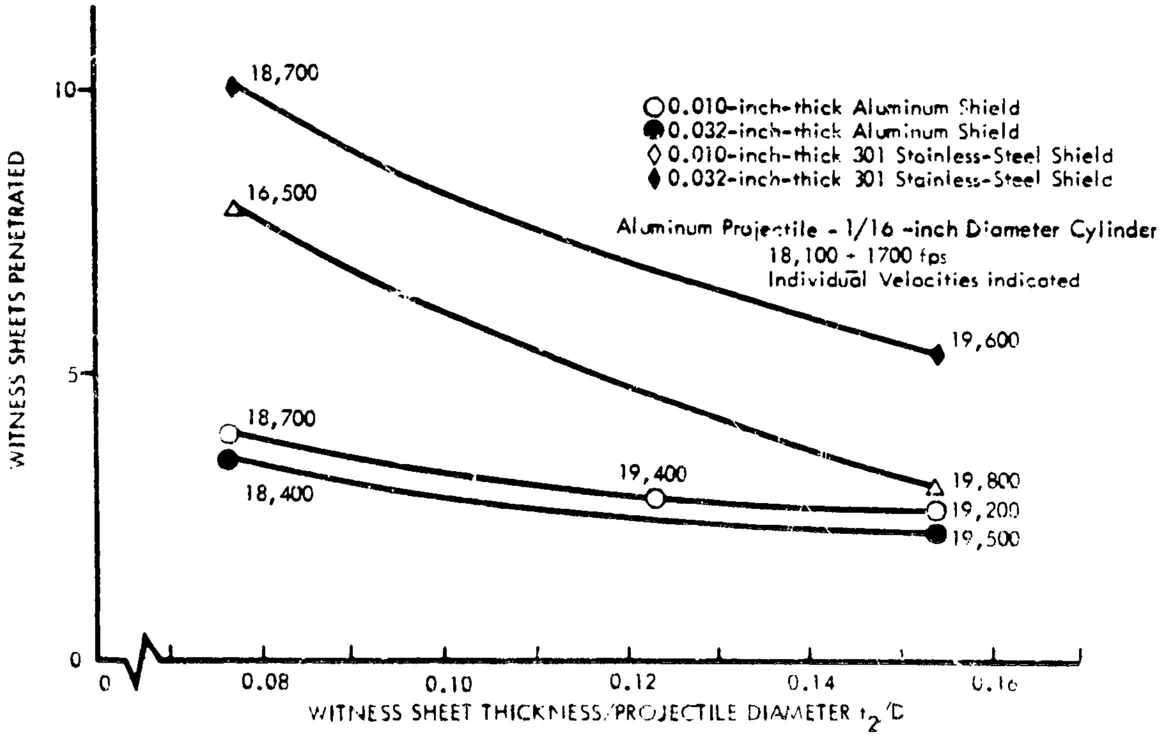

Figure 23: EFFECT OF WITNESS-SHEET THICKNESS ON PENETRATION

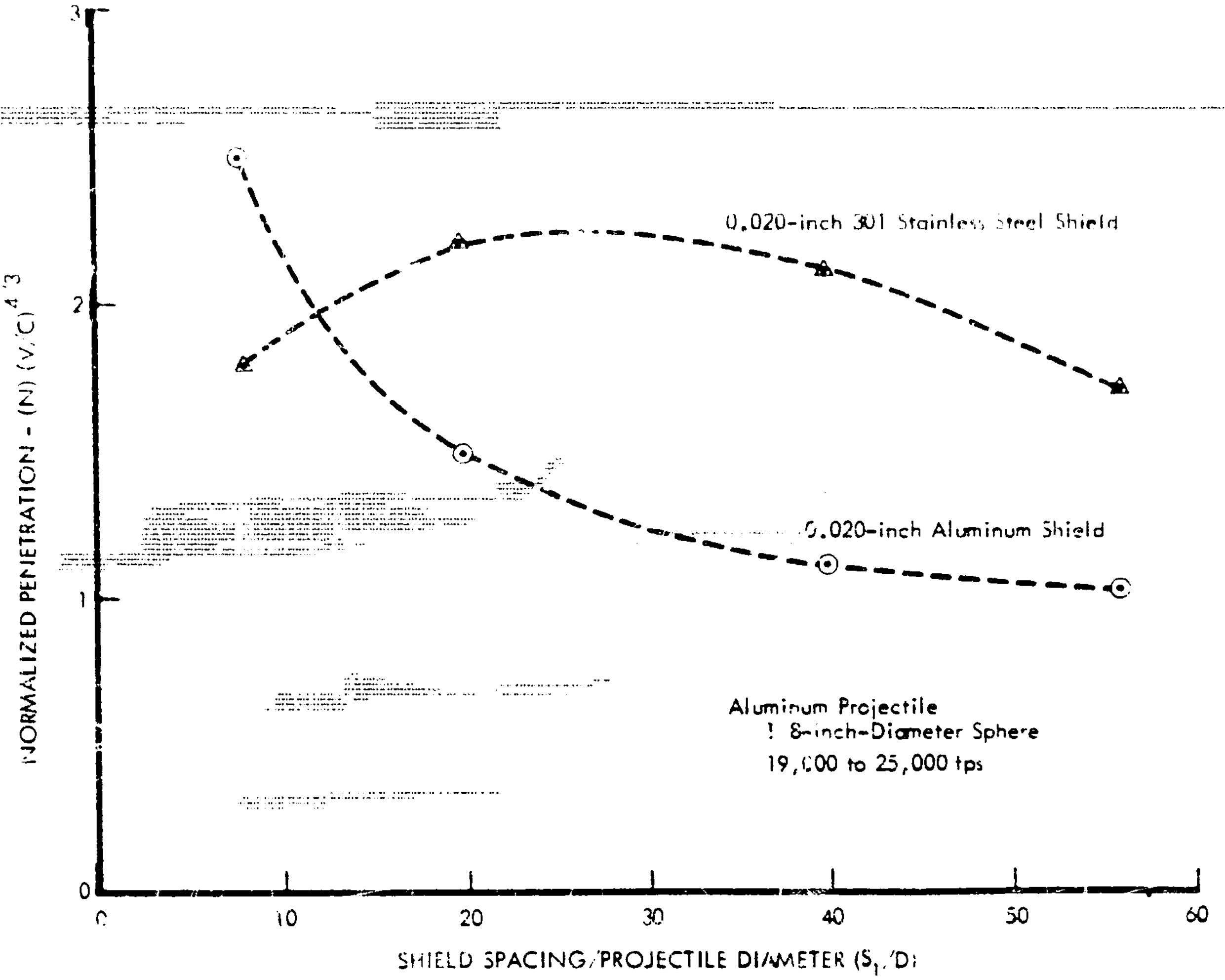

Figure 24: EFFECT OF SHIELD SPACING ON PENETRATION

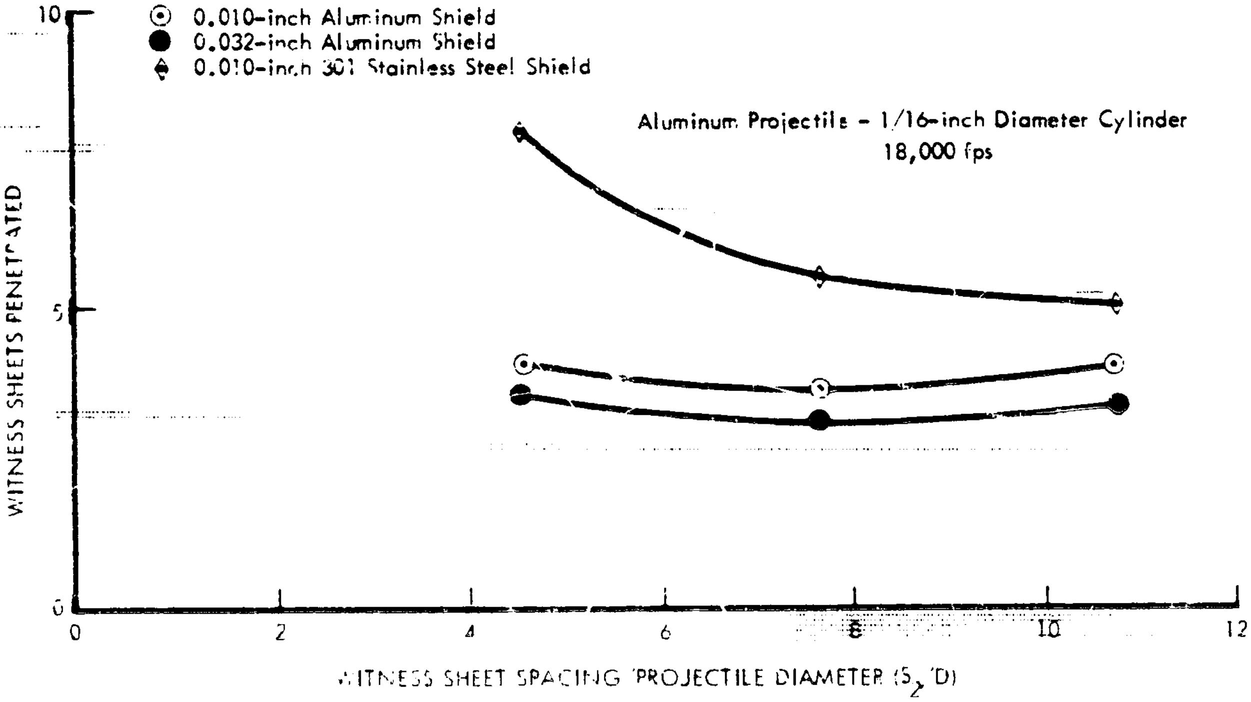

Figure 25: EFFECT OF WITNESS - SHEET SPACING ON PENETRATION

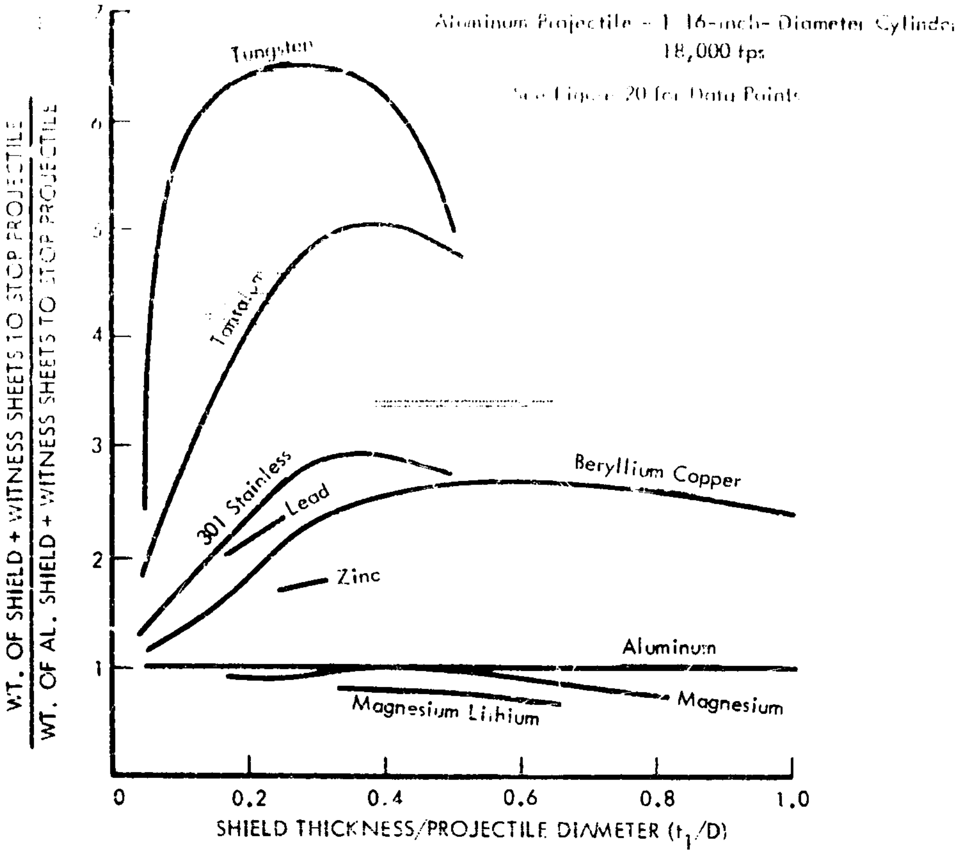

Figure 26: PENETRATION EFFICIENCY

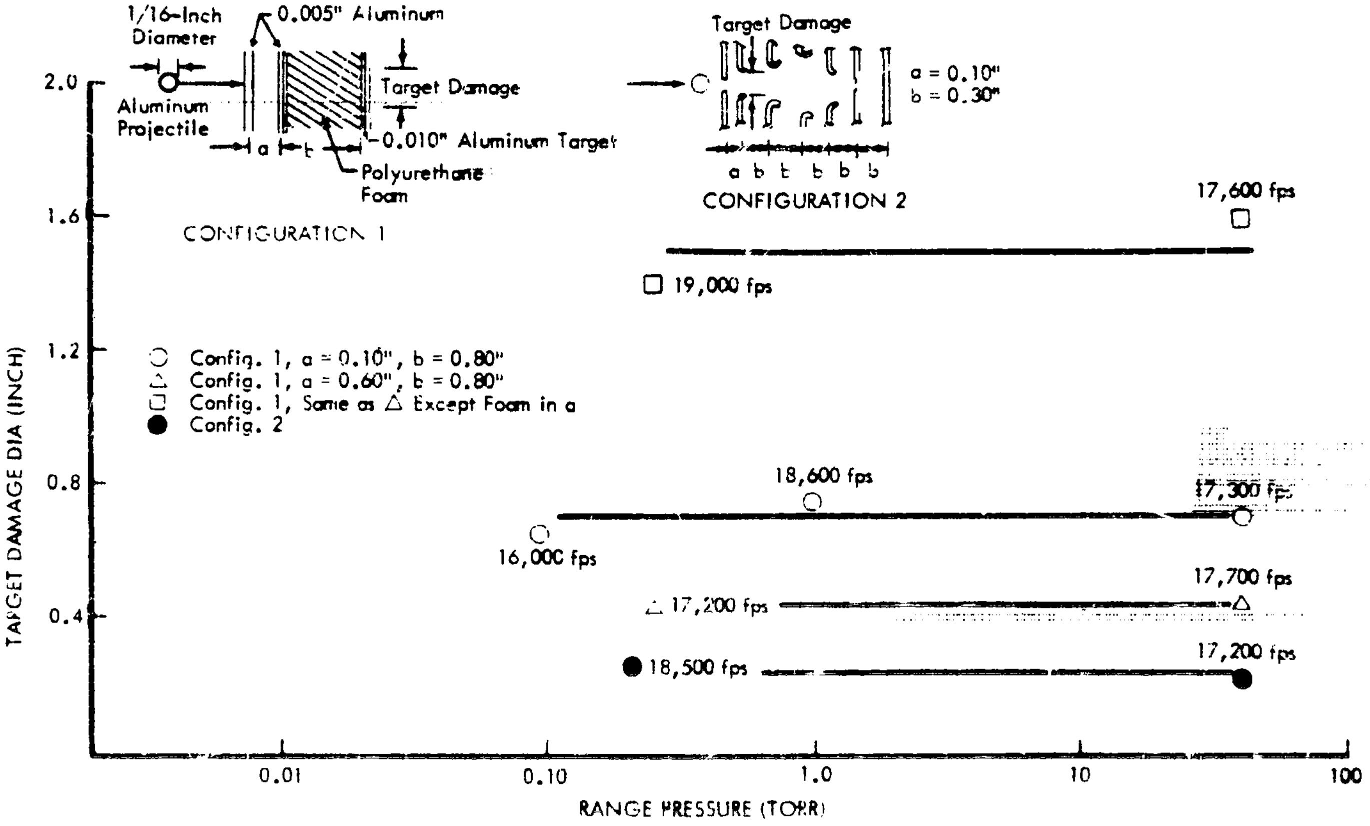

Figure 27: RANGE PRESSURE EFFECTS

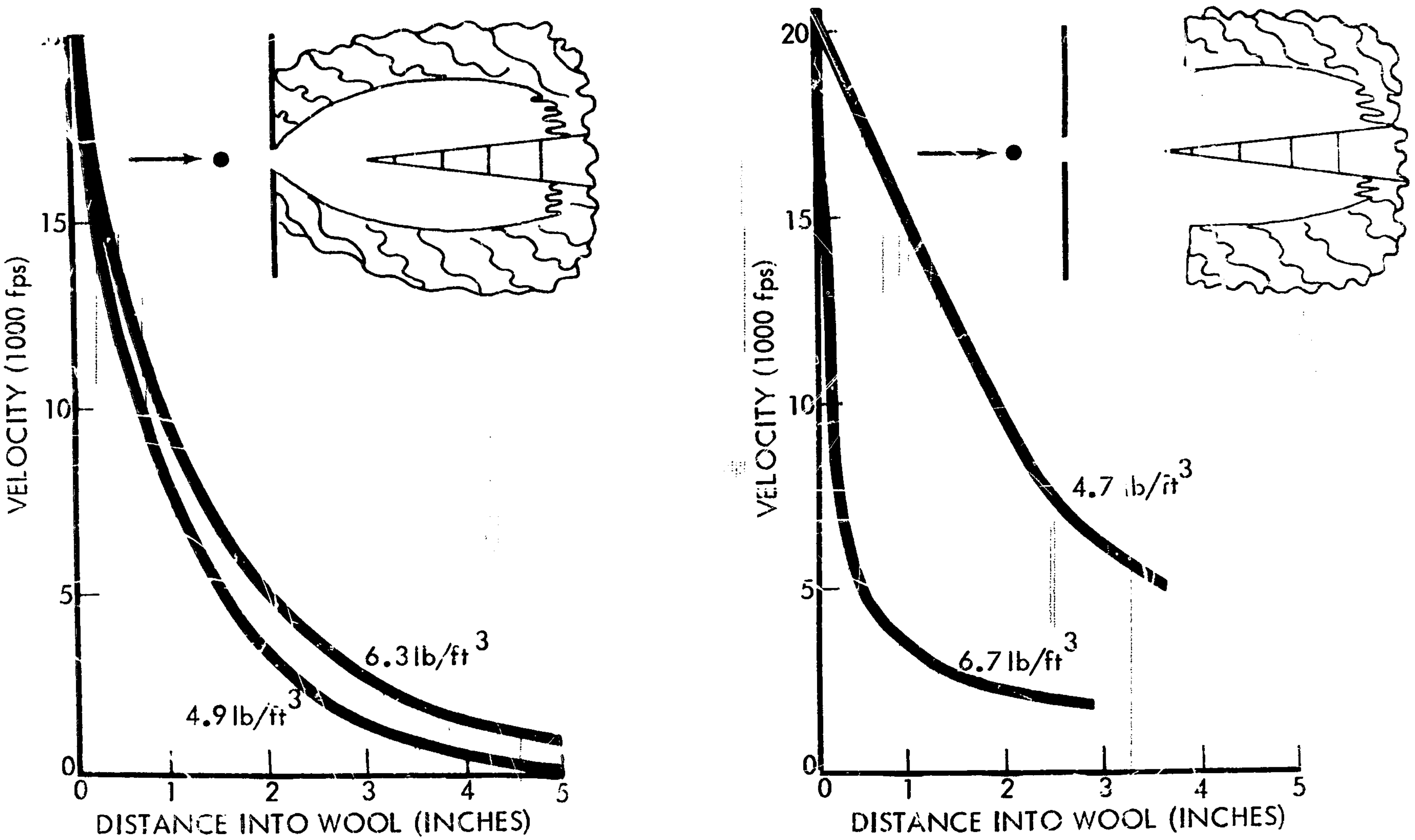

Figure 28: FRAGMENT VELOCITY DISTRIBUTION

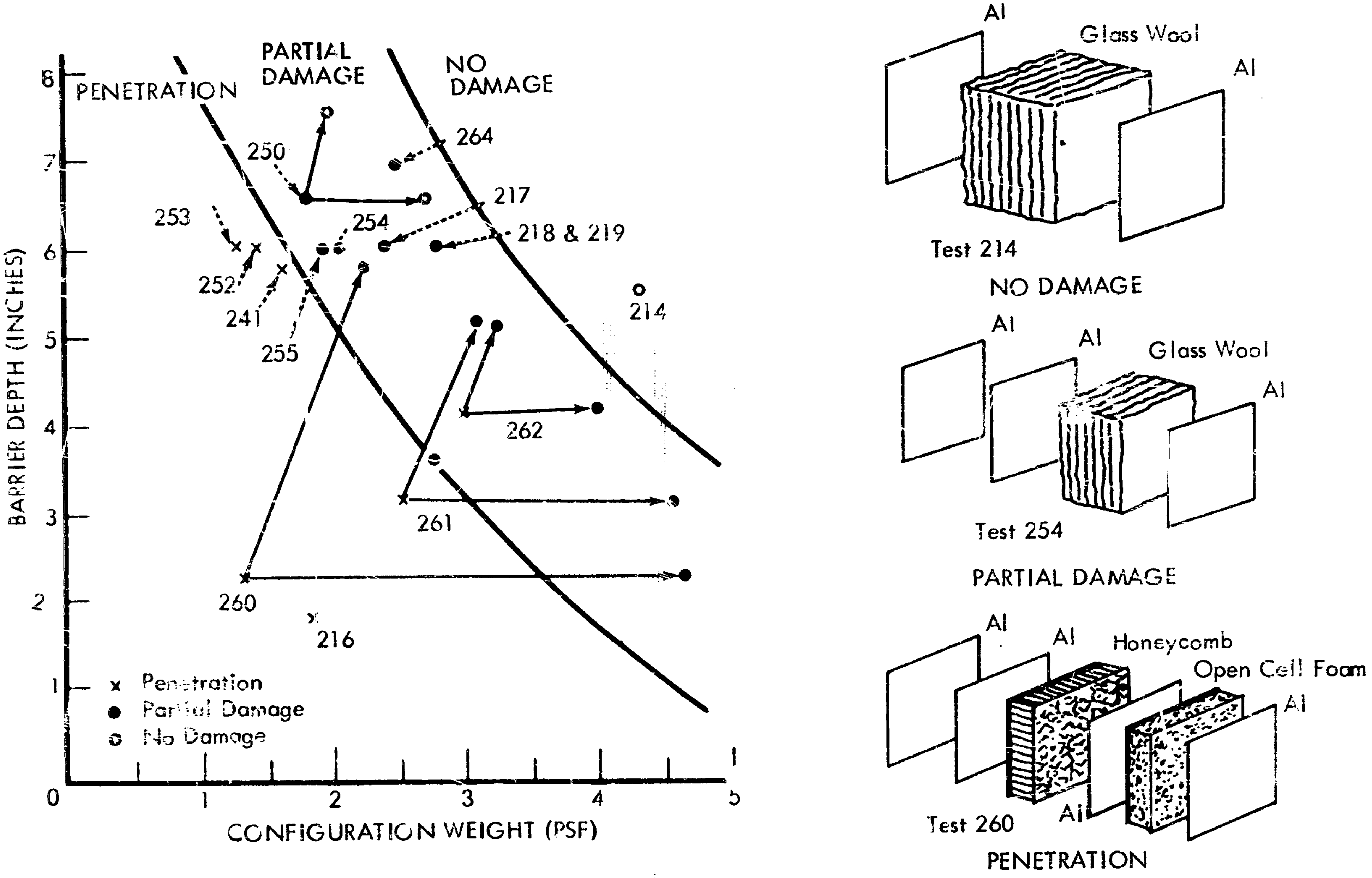

Figure 29: COMPOSITE BARRIER — 1/4-INCH-DIAMETER ALUMINUM PROJECTILE AT 20,000 FPS

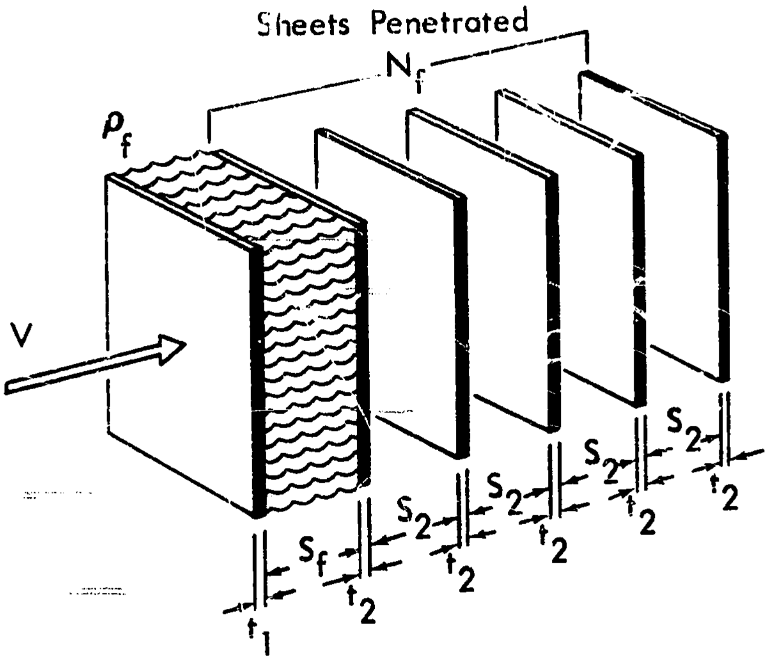

FILLER IN EXTERIOR SPACE

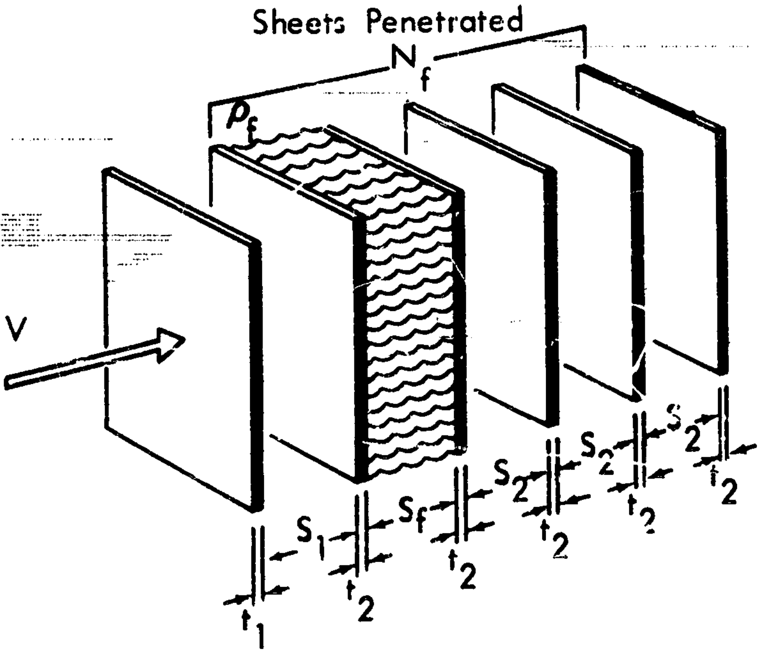

FILLER IN INTERIOR SPACE

Figure 30: LOW-DENSITY FILLER SPECIMENS

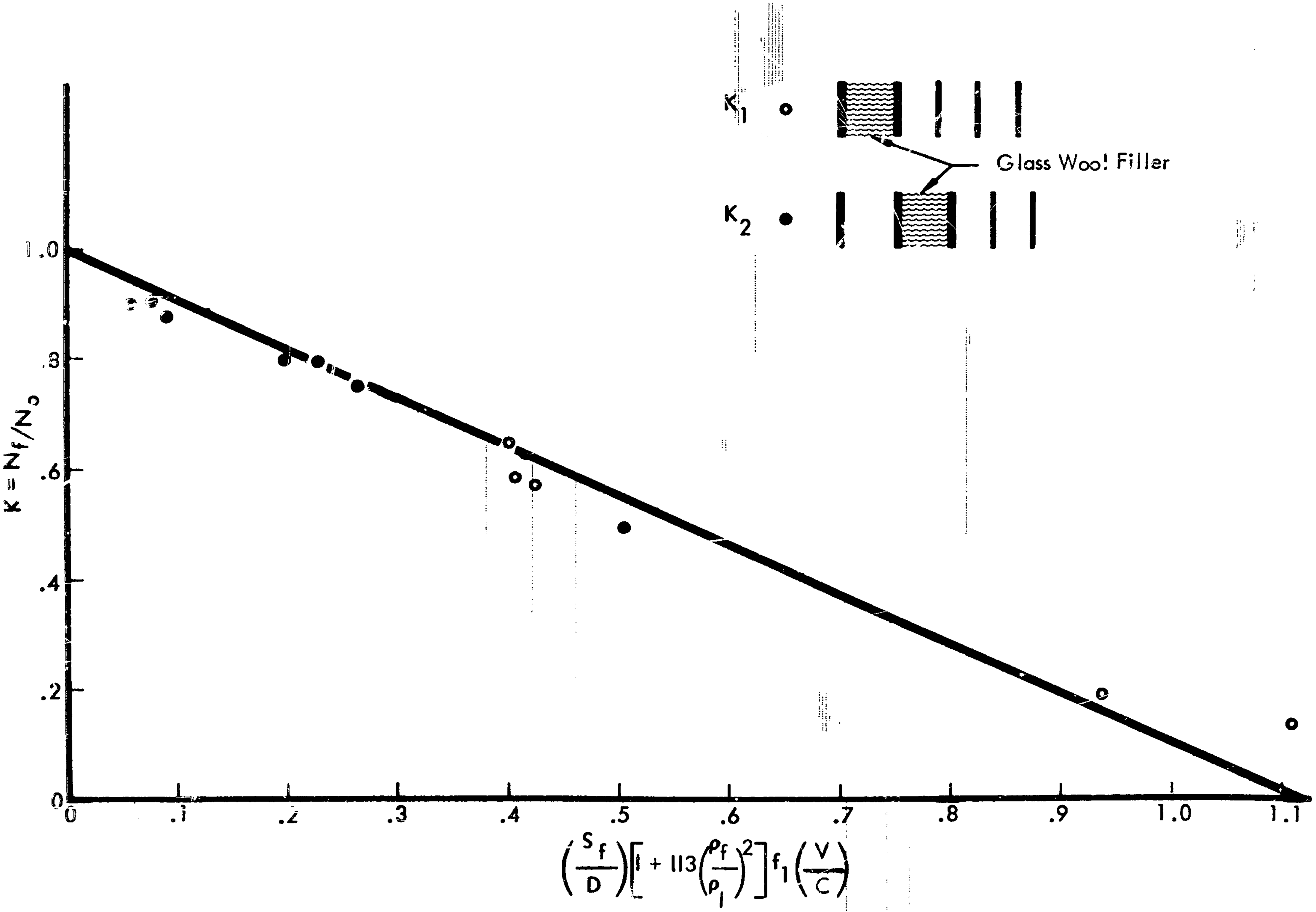

Figure 31 : PENETRATION OF THIN-SHEET AND FILLER COMBINATIONS

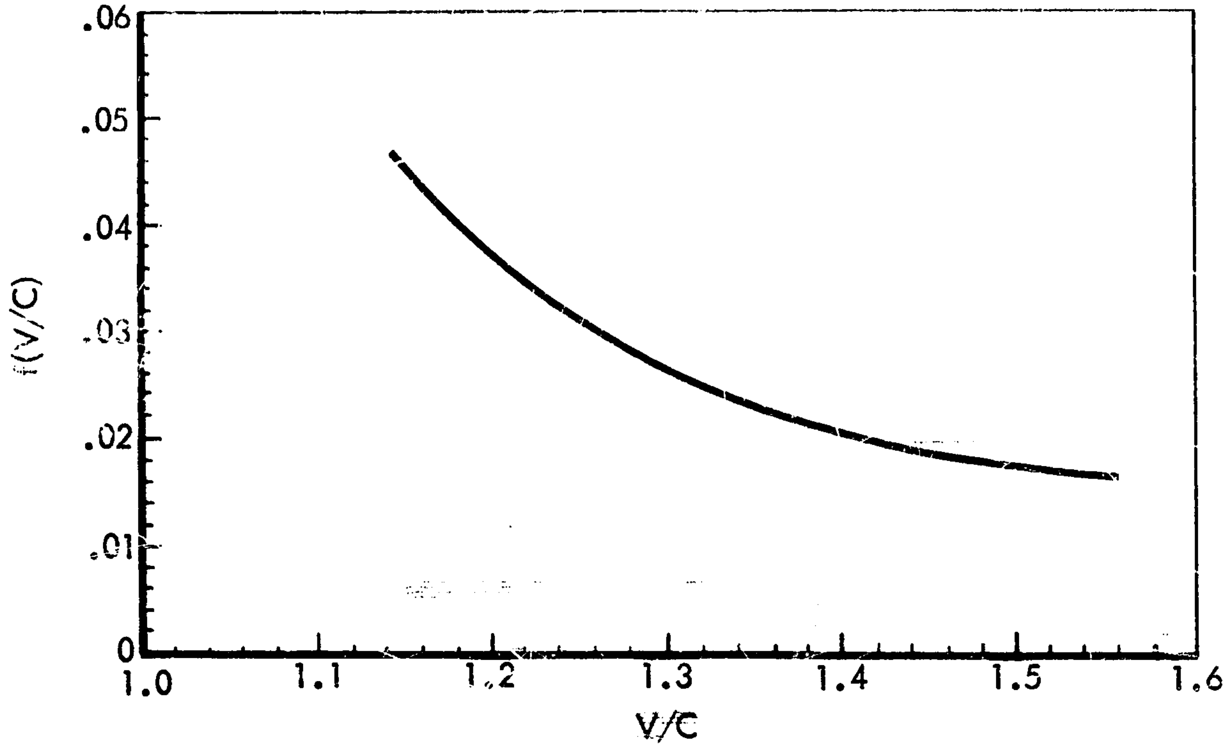

Figure 32: VELOCITY FUNCTION FOR FILLER PENETRATION

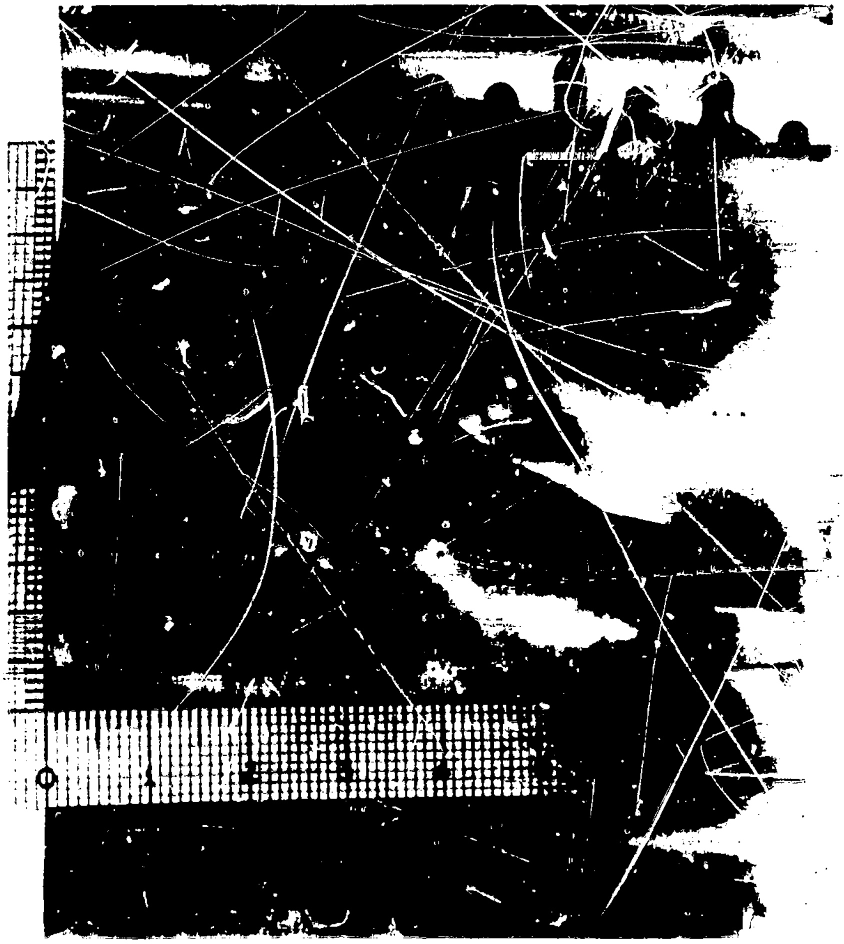

Figure 33: UNSHIELDED UNIAXIAL-STRESS SPECIMEN

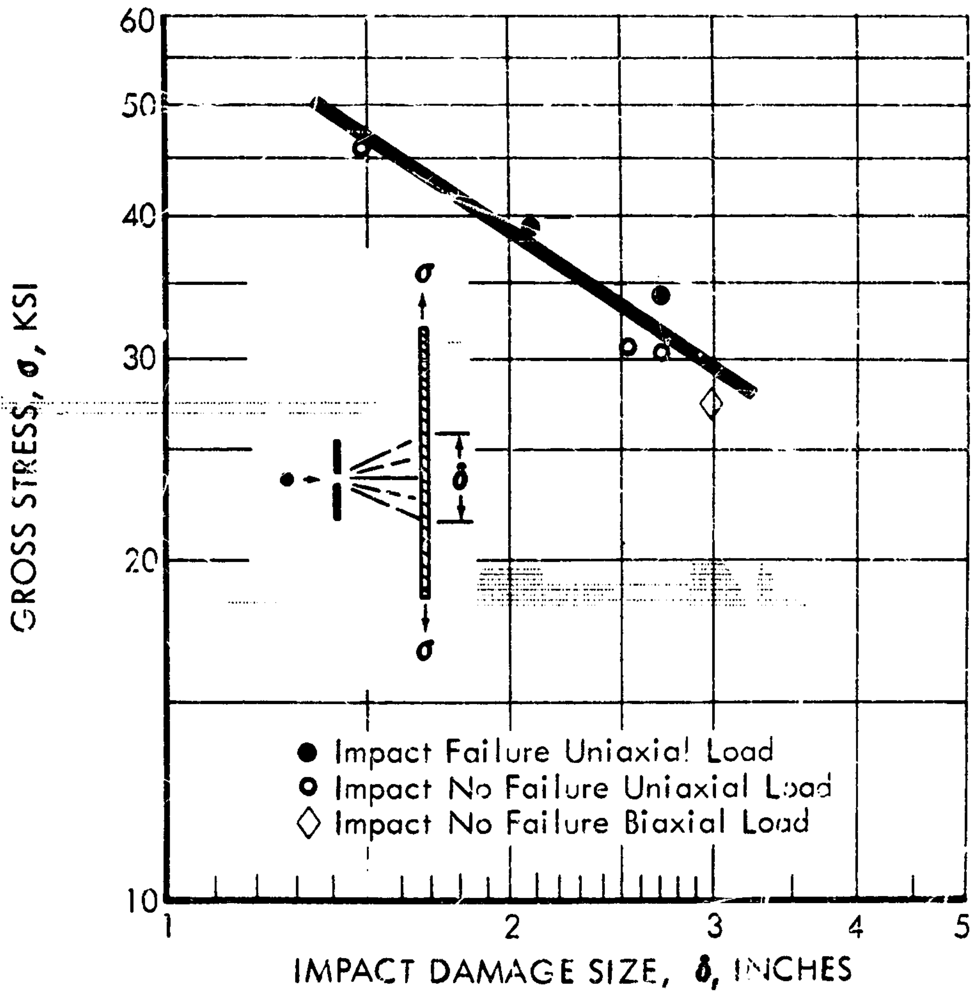

Figure 34 : IMPACT STRENGTH
0.090 INCH 2014-T6 ALUMINUM AT -200°F

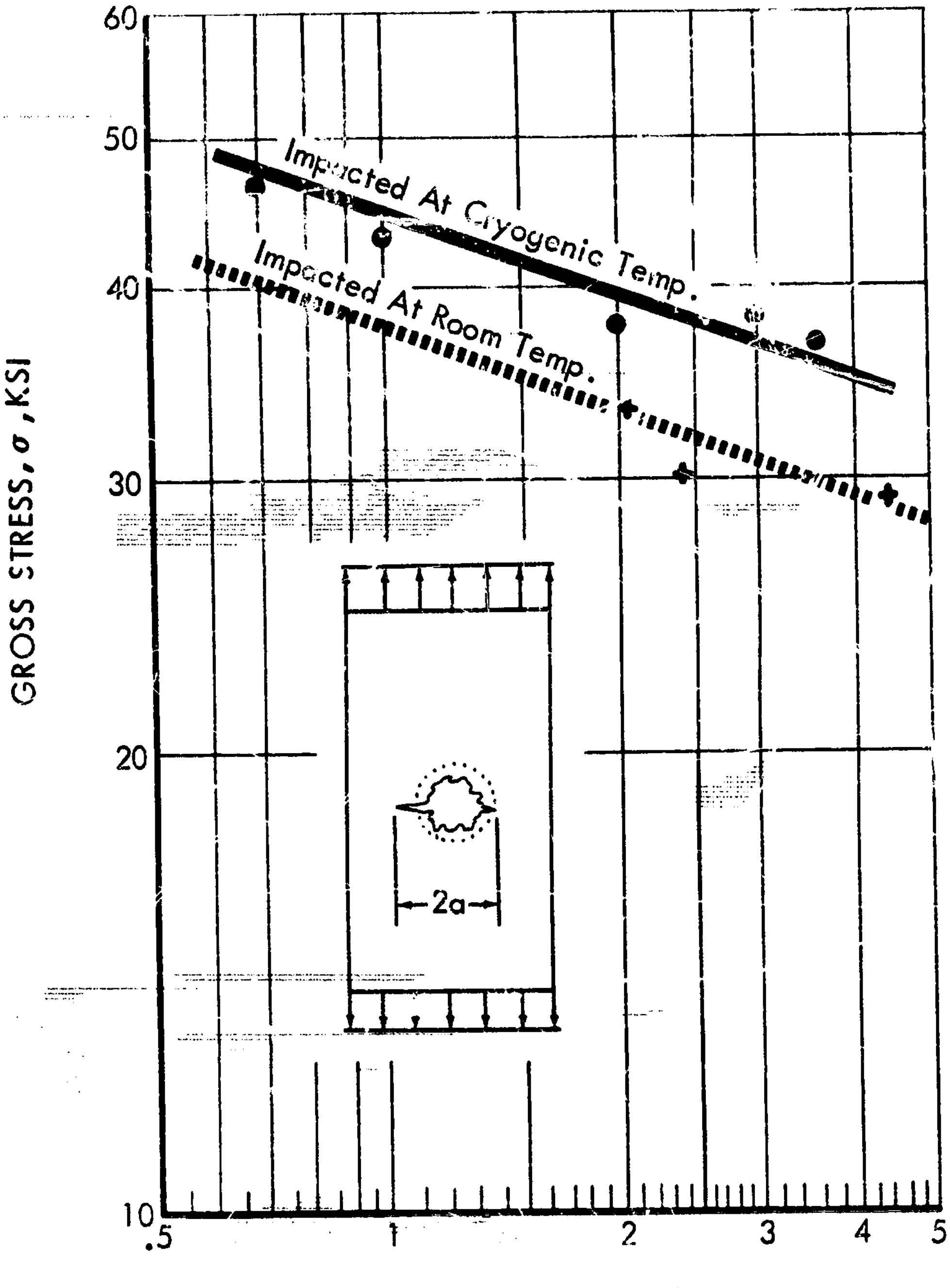

Figure 35: RESIDUAL STRENGTH
0.100 INCH 2219-T62 ALUMINUM AT 70°F

Figure 36: SHIELDED UNIAXIAL-STRESS SPECIMEN
1/4-INCH-DIAMETER ALUMINUM PROJECTILE
AT 20,000 FPS; TEST TEMPERATURE: -285°F

Figure 37: BIAXIAL-STRESS SPECIMEN IN RANGE TANK

Figure 38: UNSHIELDED BIAXIAL-STRESS SPECIMEN
3/16-INCH-DIAMETER ALUMINUM PROJECTILE AT
23,600 FPS; TEST TEMPERATURE: -300°F

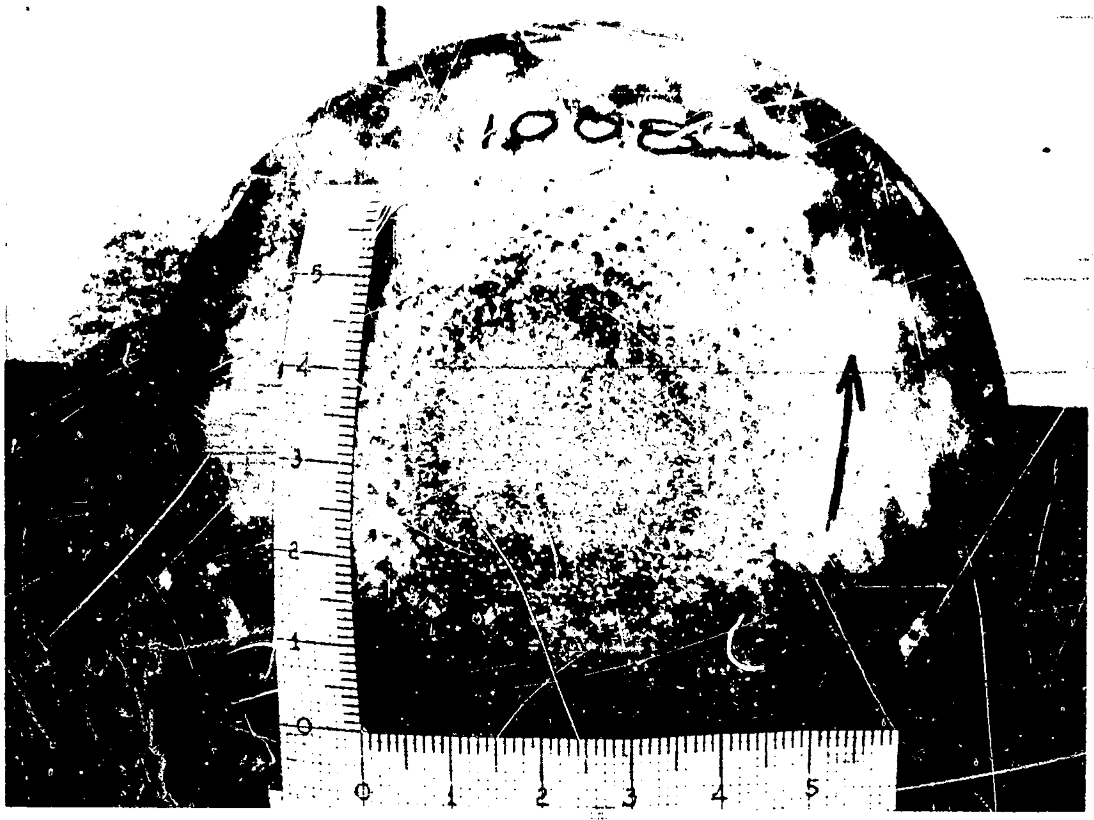

Figure 39: SHIELDED BIAXIAL-STRESS SPECIMEN - NO FAILURE
1/4-INCH ALUMINUM SPHERE AT 20,000 FPS TEST TEMPERATURE -200°F

Figure 40: SHIELDED BIAXIAL-STRESS SPECIMEN TEST - FAILURE
1/4-INCH ALUMINUM SPHERE AT 21,100 FPS TEST TEMPERATURE -220°F

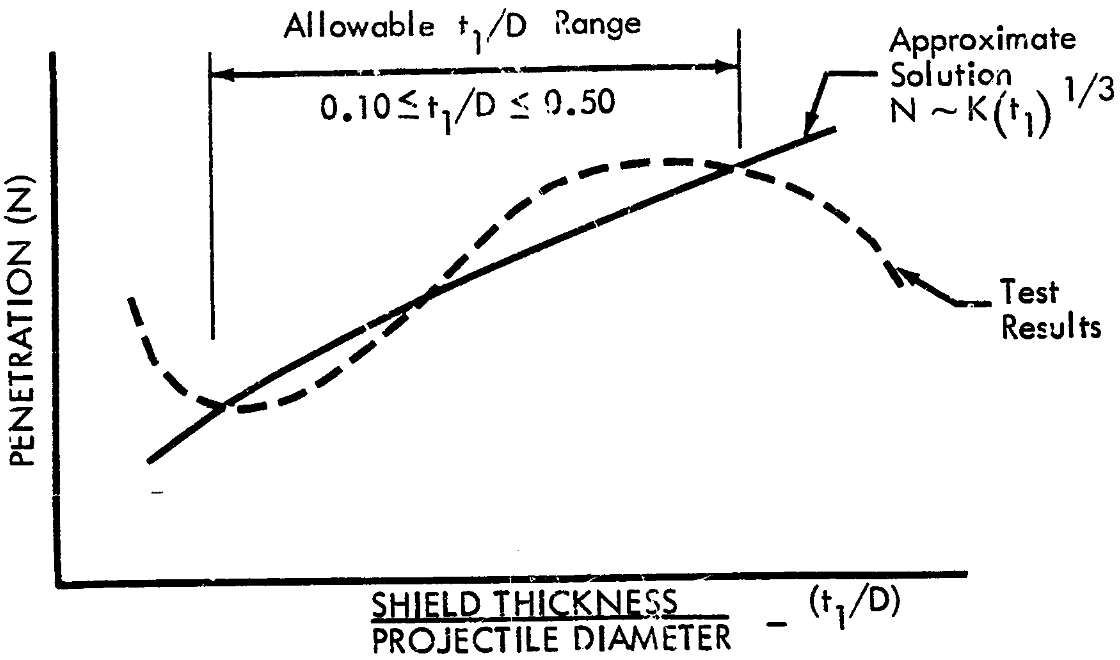

Figure 41: APPROXIMATE t_1/D FUNCTION - ANY SHIELD MATERIAL

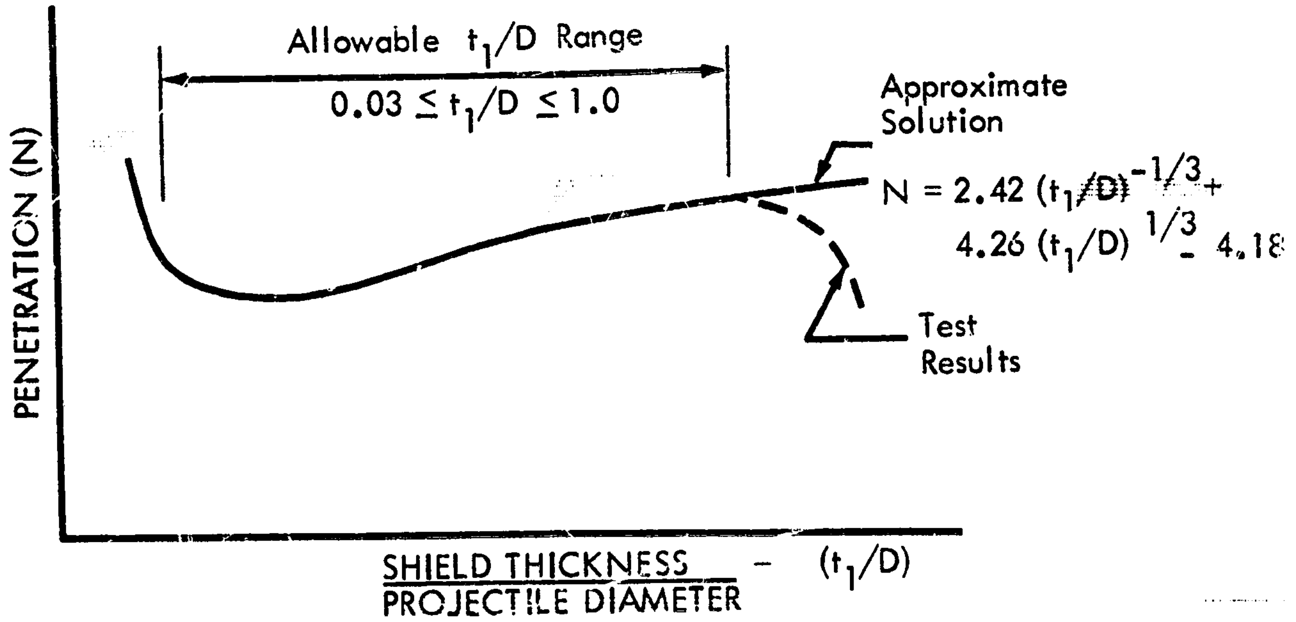

Figure 42: APPROXIMATE t_1/D FUNCTION - ALUMINUM SHIELD

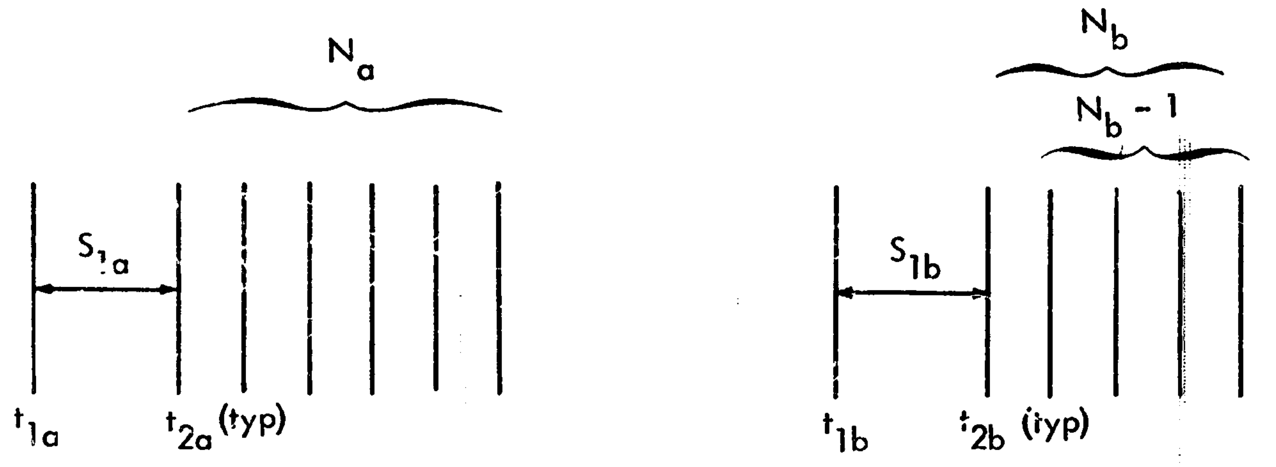

(A) TEST CONFIGURATION

(B) CALCULATED CONFIGURATION

$t_{1a} = t_{1b} = t_{1c}$

$S_{1a} = S_{1b} = S_{1c}$

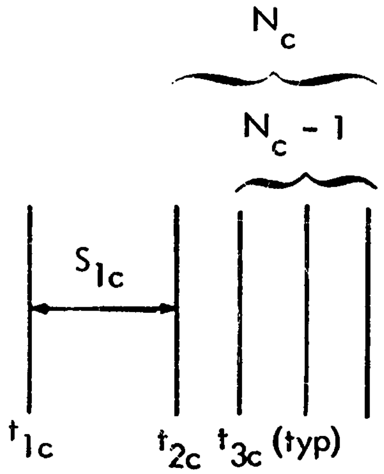

$t_{2c} = t_{2b}$

(C) DESIRED CONFIGURATION

Figure 43: MULTISHEET BARRIERS — CONFIGURATIONS FOR EXPERIMENTAL DETERMINATION

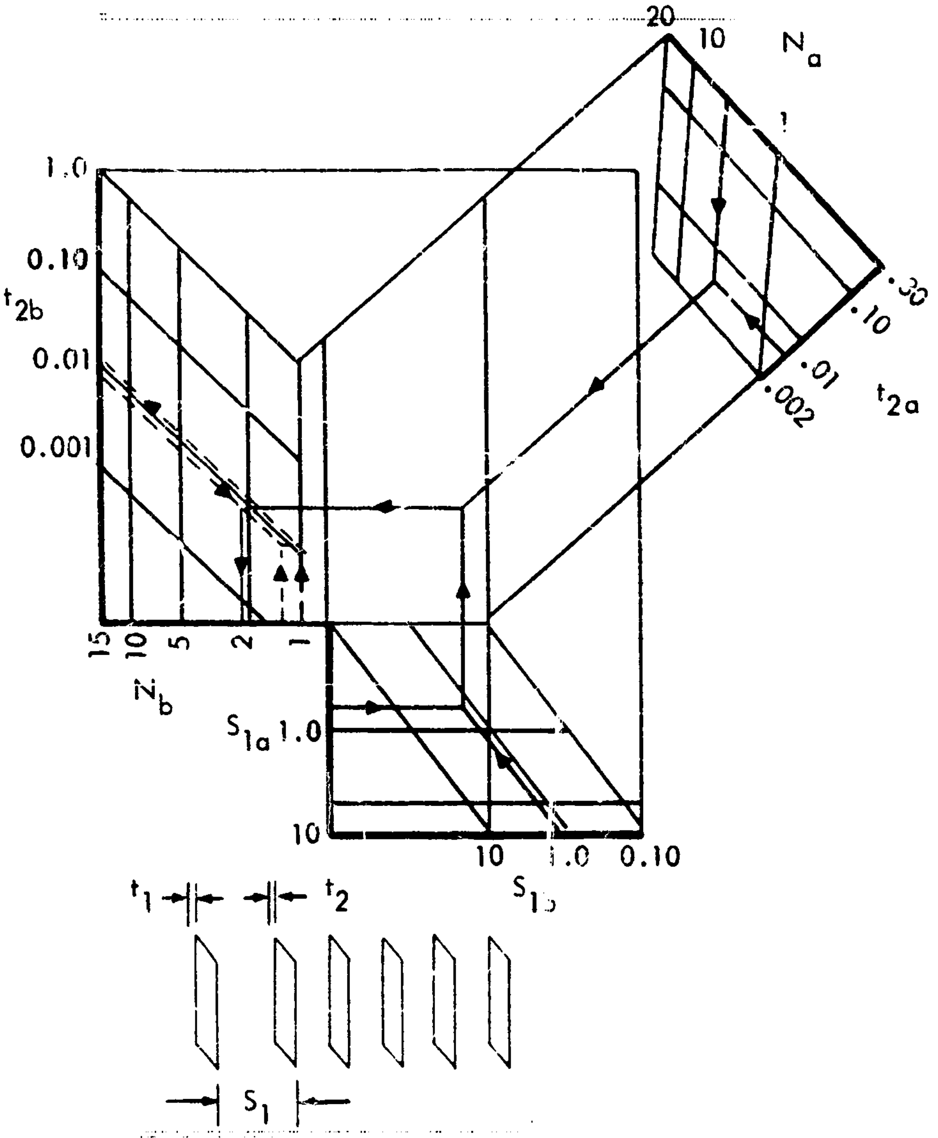

EXAMPLE	NOMINAL CONFIG.	FIRST SHEET	SECOND SHEET
t_1	0.010"	0.010'	
t_2	0.005"	0.008'	0.012"
S_1	0.60"	1.25"	
N	4	2.3	1.3

N - Penetration Beyond
First Sheet
a - Nominal (Test) Configuration
b - Required Configuration

Example Solves for 'N'
of Required Configuration

See Back Cover Pocket for Larger Version of this Figure

Figure 44: EXPERIMENTAL DETERMINATION OF MULTISHEET BARRIERS

EXAMPLE

GIVEN	REQ'D
$P(n) = .997$ $n = 0$ $A = 1040\ FT^2$ $\tau = 150$ HRS FLUX-HAWKINS $\rho_p = 0.5\ GM/CM^3$	$M = 0.0043$ GM $D = 0.10$ IN

$P(n)$ = Probability of n or Fewer Penetrations

n = Allowable Number of Penetrations

A = Exposed Area

τ = Exposed Time

ρ_p = Meteoroid Density

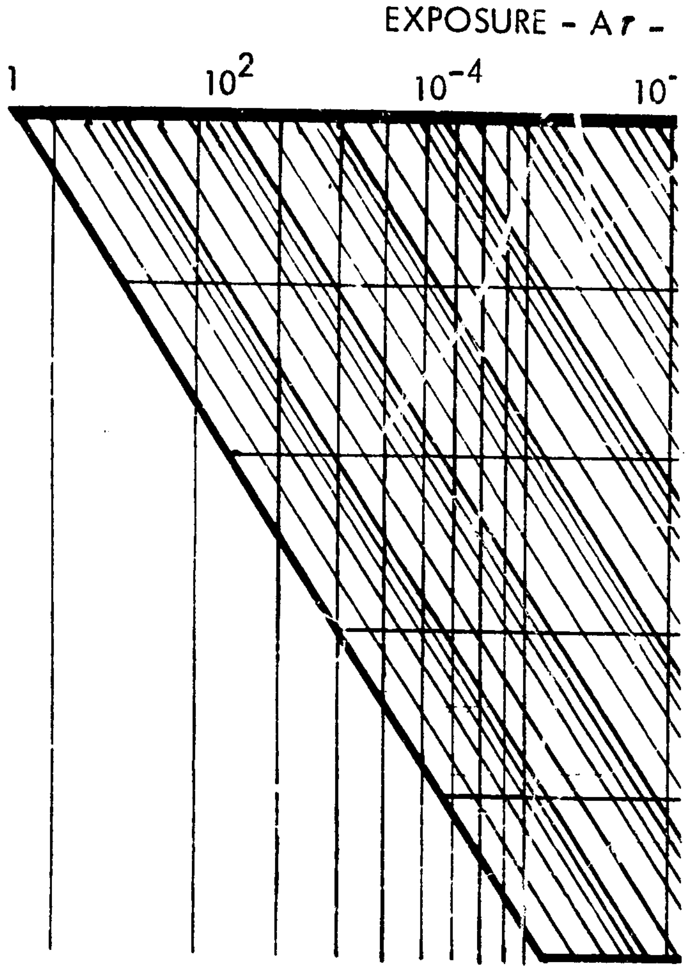

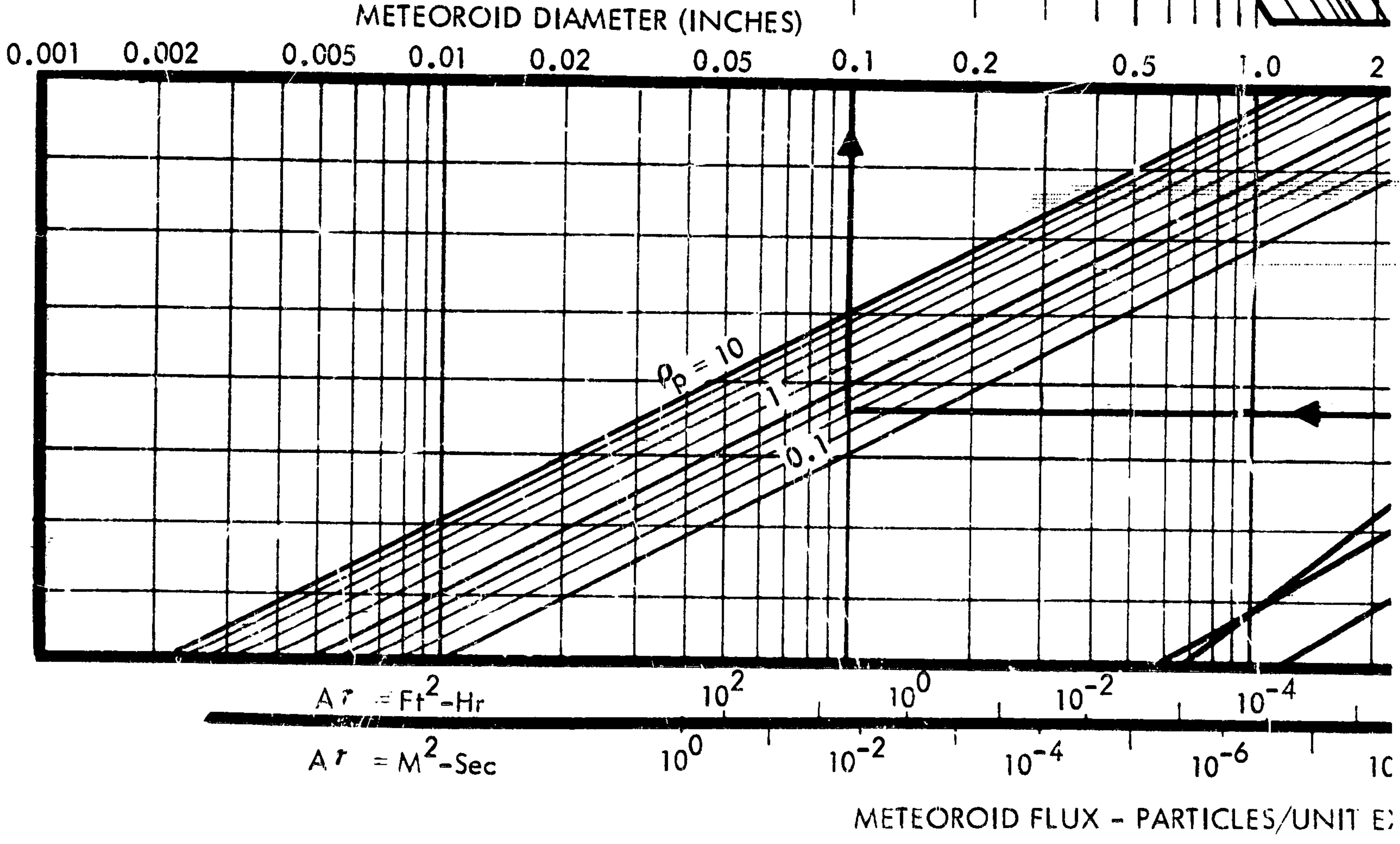

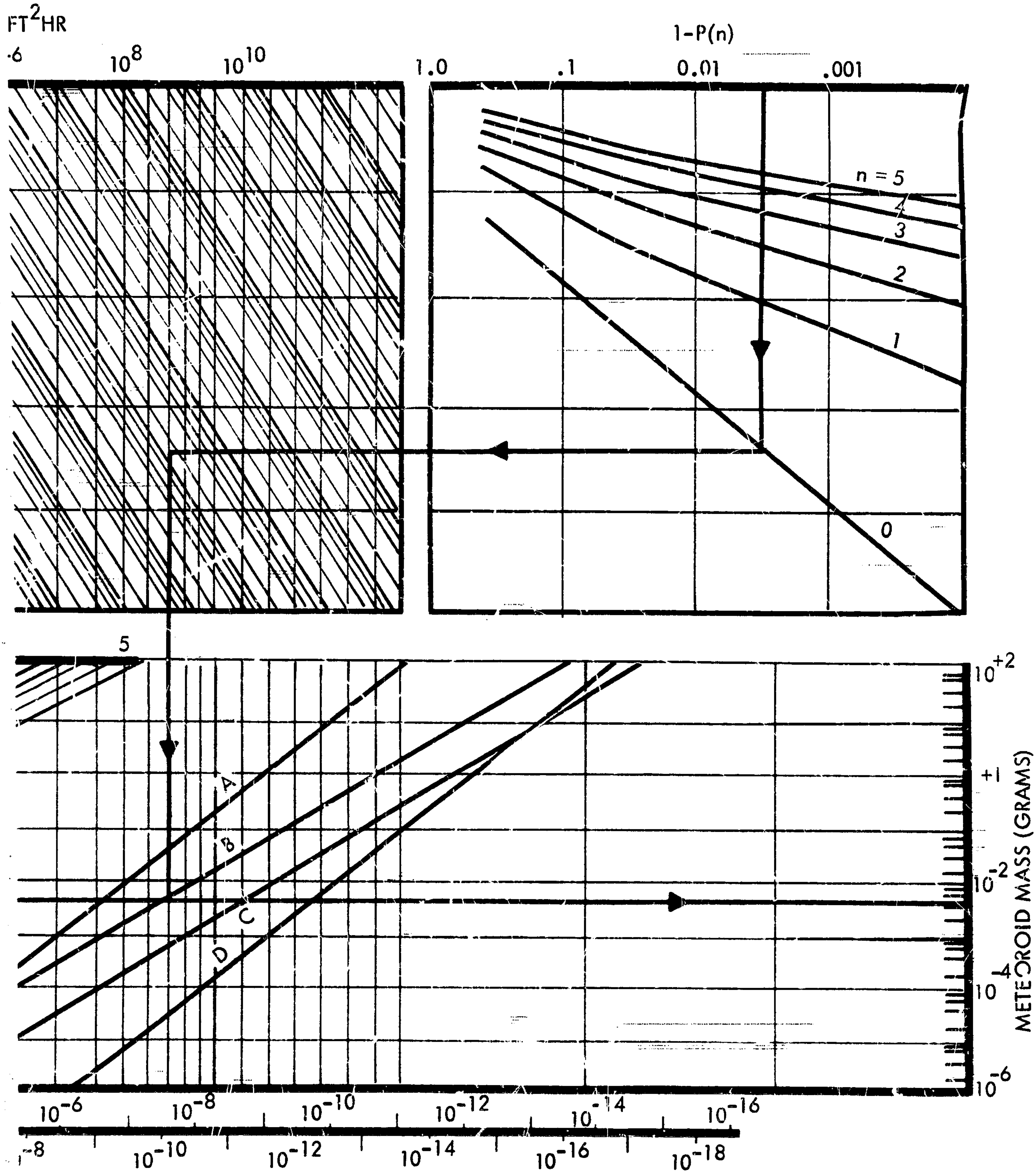

A - Pessimistic Flux = $10^{-8}/m \left(\frac{N}{M^2HR}\right)$

B - Hawkins Flux (Ref 16)

C - Whipple Flux 1963A (Ref 17)

D - Optimistic Flux = $10^{-11}/m \left(\frac{N}{M^2\ HR}\right)$

Figure 45: METEOROID SIZE

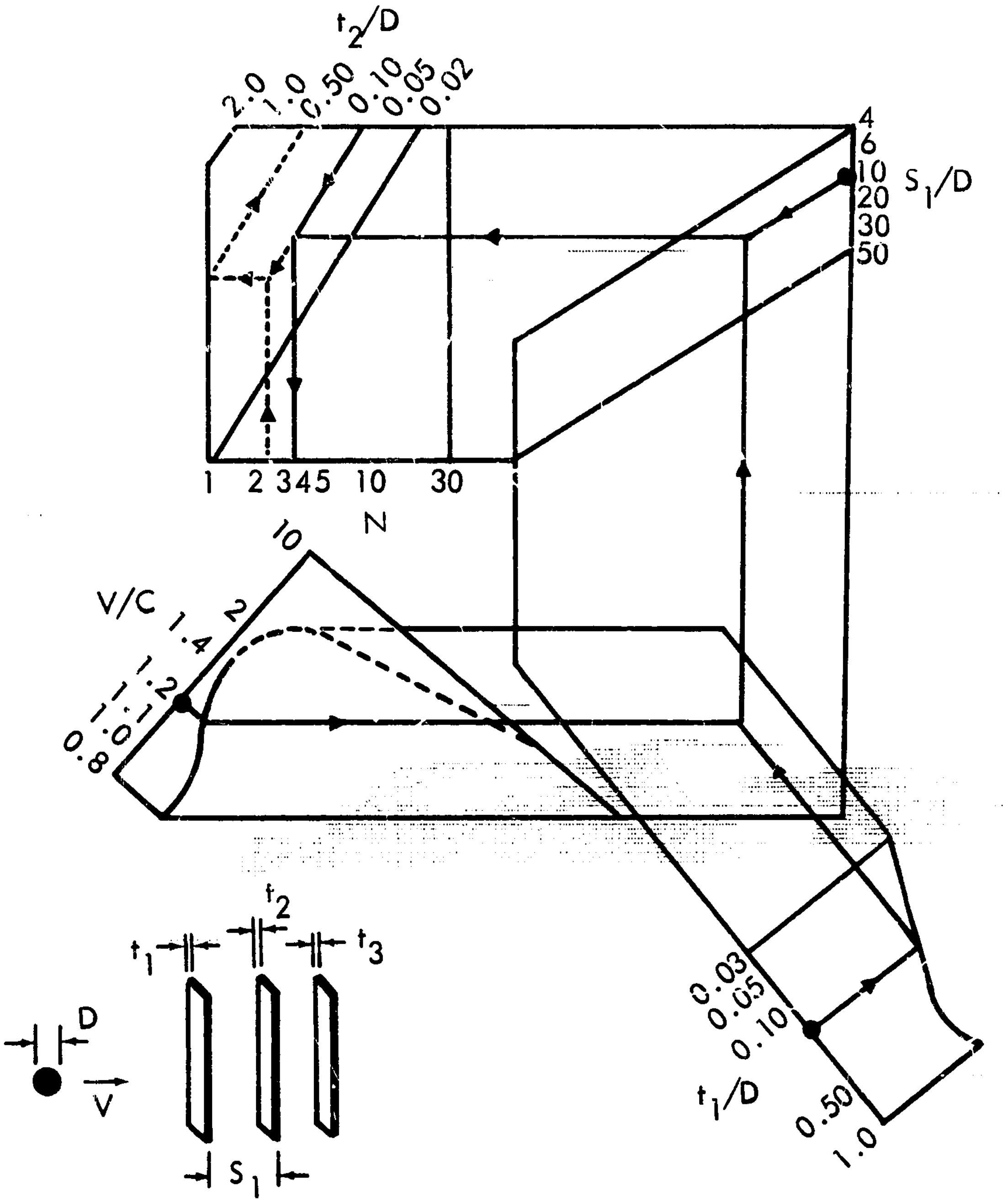

See Back Cover Pocket for Larger Version of of this Figure

EXAMPLE	GIVEN	FIRST STEP	SECOND STEP
D	0.25		
V/C	1.2	1.2	
t_1/D	0.16	0.16	
S_1/D	10	10	
t_2/D	0.08	0.08	0.08
t_3/D	?	0.08	0.36
N		3.4	2.4
PENETRATION	3 SHEET REQ'D	5	3

Figure 46: DESIGN OF MULTISHEET METEOROID BARRIERS

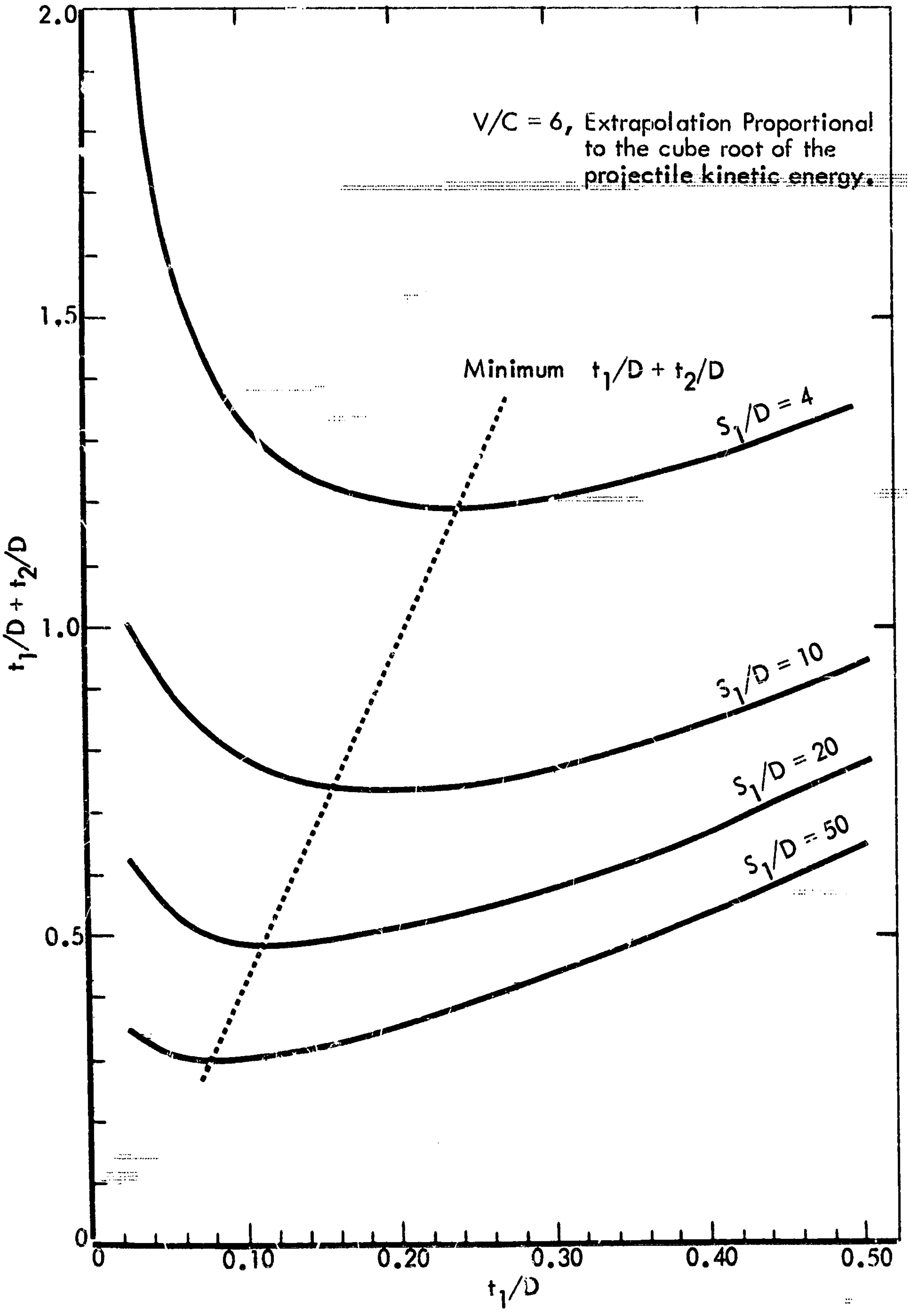

Figure 47: MINIMUM WEIGHT TWO-SHEET ALUMINUM BARRIER

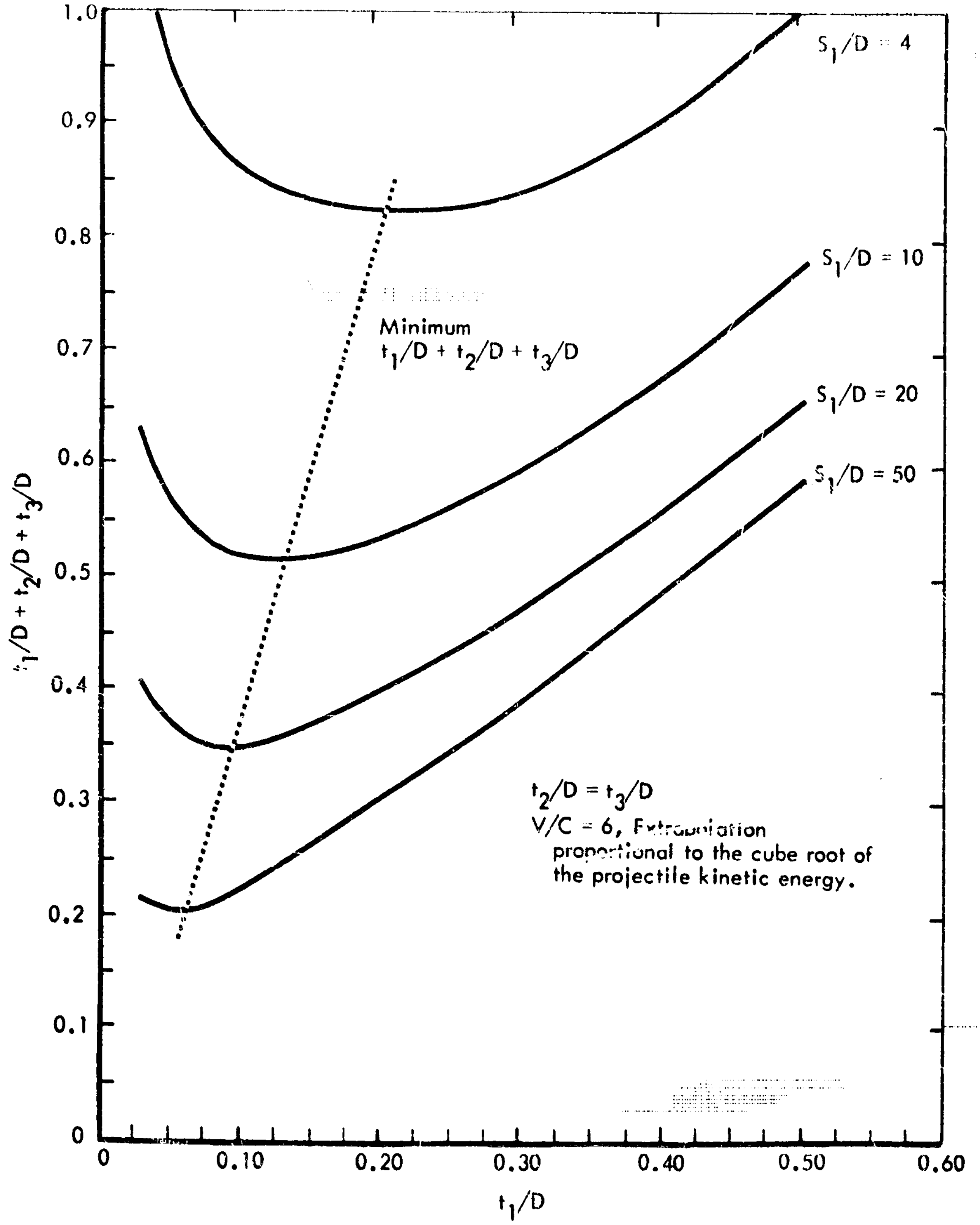

Figure 48: MINIMUM WEIGHT THREE-SHEET ALUMINUM BARRIER

"PRECEDING PAGE BLANK-NOT FILMED"

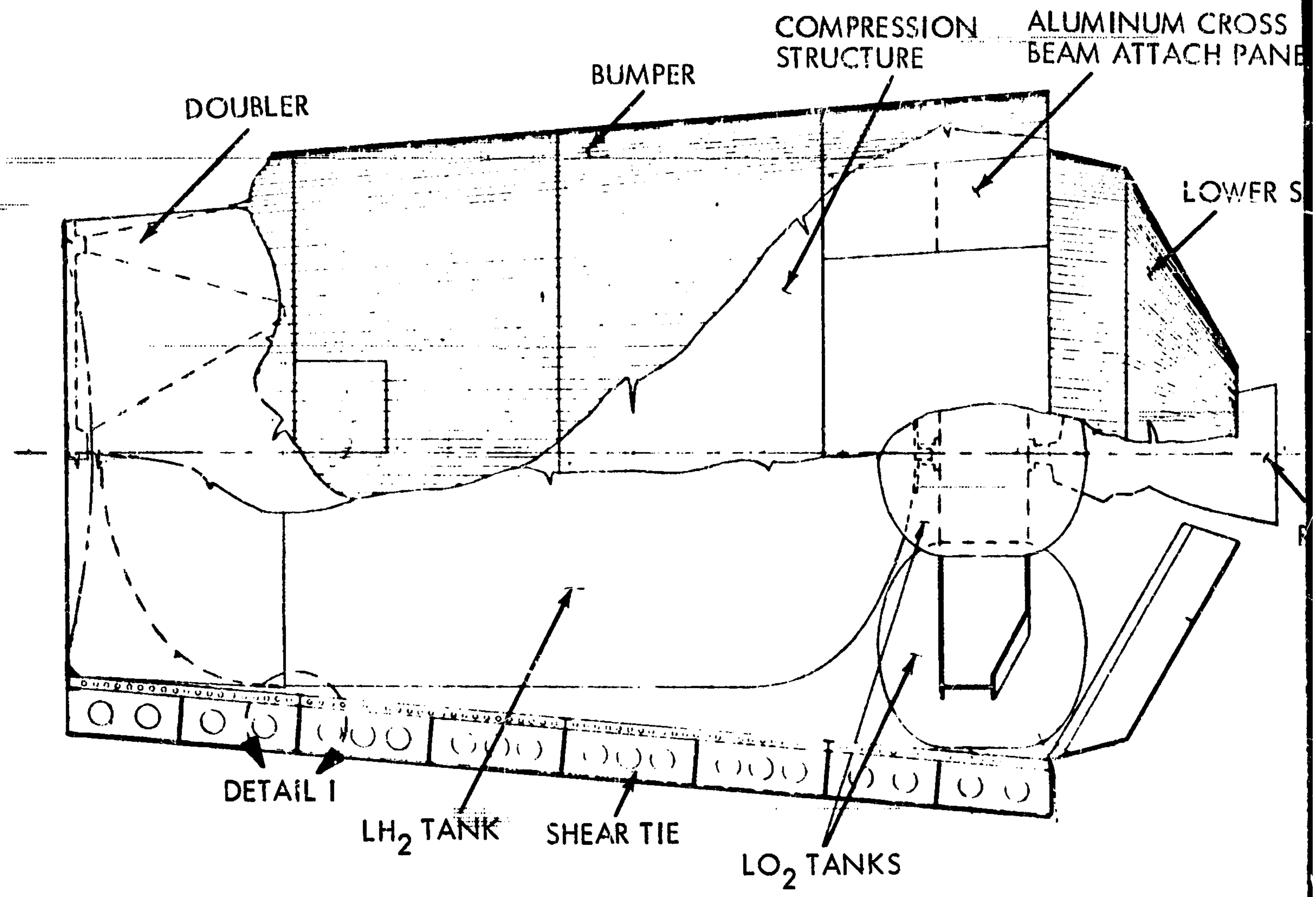

SIDE VIEW

1/50 SIZE

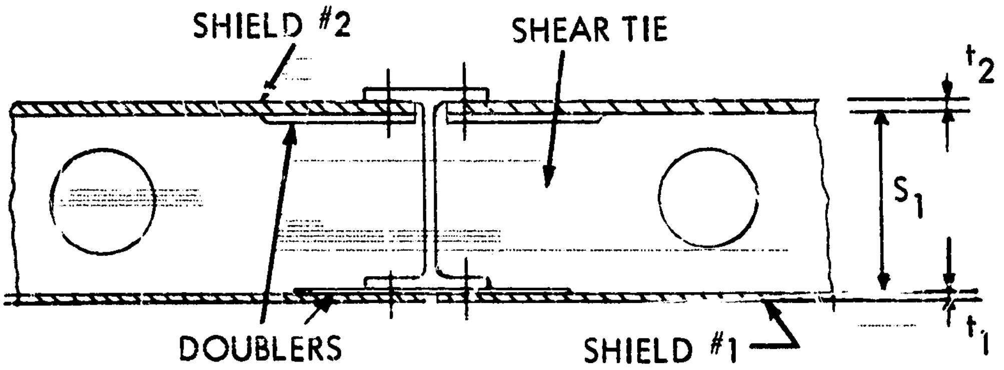

DETAIL I

TWO-SHEET CONFIGURATION

	TWO-SHEET*		
P (o)	0.9	0.999	0.999
D (in)	0.04	0.1	0.27
t_1 (in)	0.020	0.020	0.051
S_1 (in)	3.4	3.4	2.0
t_2 (in)	0.040	0.049	0.192
S_2 (in)			
t_3 (in)			

Flux: Hawkins

V = 100,000 fps

Shield Material - Aluminu
*The Thicknesses Shown He
Meteoroid to Just Penetra
Factor Must be Selected t
Thicknesses to a Safe Lev

HIELD

-10 ENGINE

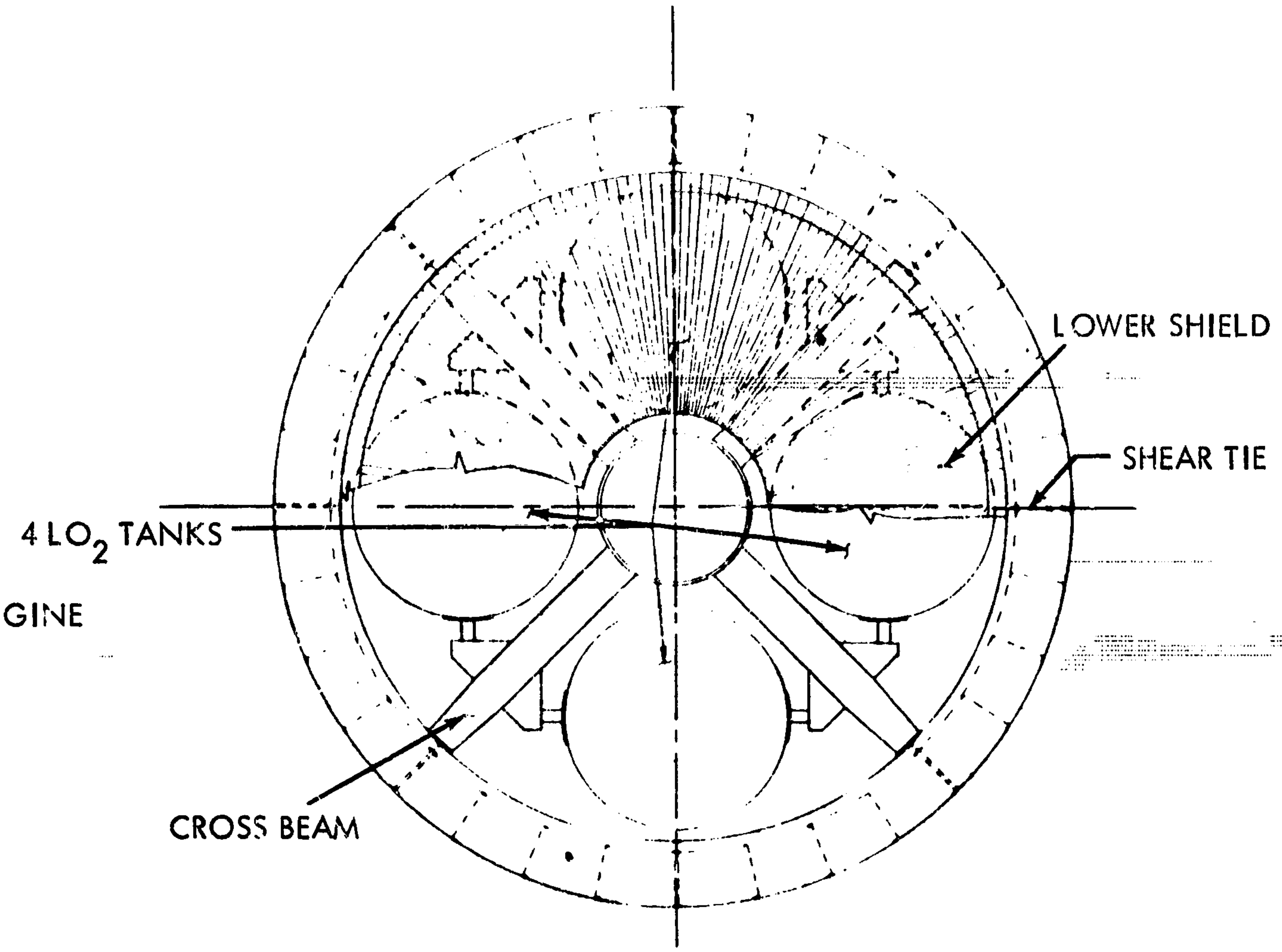

END VIEW

1/50 SIZE

	THREE-SHEET*				
	0.9	0.999	0.9999	0.9999	0.9999
	0.4	0.14	0.27	0.27	0.27
	Min	0.003	0.042	0.035	0.027
	2	2.0	2.0	3.0	5.0
	0.020	0.020	0.062	0.050	0.037
	3.4	3.4	3.4	3.4	3.4
	0.040	0.040	0.062	0.050	0.037

$\rho_p = 0.50$ gm/cc

$t = 1.56 \times 10^5$ sq ft hr

re will Allow the
a. An Arbitrary
Increase These
l.

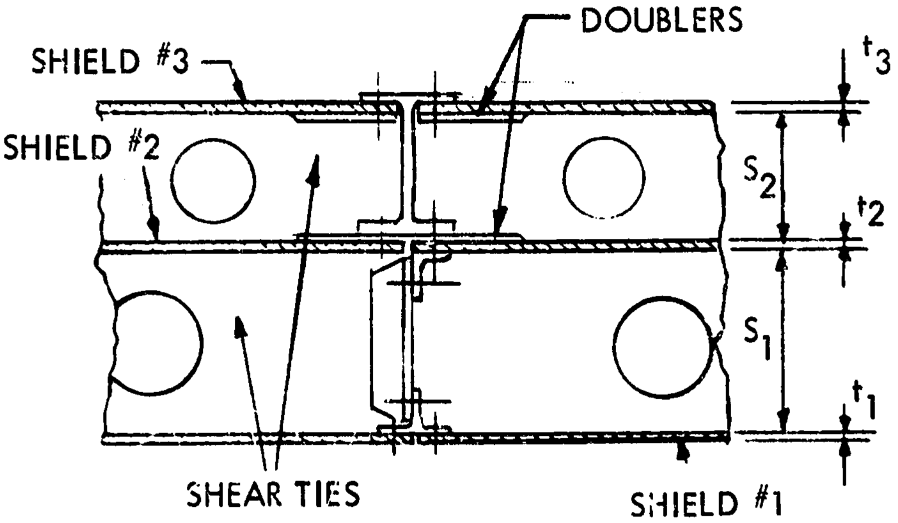

DETAIL I

THREE-SHEET CONFIGURATION

Figure 49: CRYOGENIC MODULE

BLANK PAGE

APPENDIX A — TEST DATA

Table A-1: RANGE PRESSURE EVALUATION — 1/16-INCH LIGHT-GAS GUN

Multiple-Sheet Tests; Aluminum Cylindrical Projectiles: 0.065 In. Dia by 0.065 In. Long; Mass = 9.7 x 10^{-3} Gram; All Sheets 0.005-In.-Thick Aluminum

Test Number	Velocity (fps)	Shield Spacing (in.)	Range Pressure (torr)	Shield Damage Diameter (in.)	Diameter of Perforations (in.)	Witness Sheets Penetrated
1	17,500	0.6	40	0.076	0.65	4
2	16,600	0.6	0.095	0.070	0.80	4
3	17,500	0.1	40	0.070	0.20	6
4	18,200	0.1	0.21	0.078	0.25	5

Table A-2: FILLER EVALUATION — 1/32-INCH LIGHT-GAS GUN

Magnesium-Lithium Projectile: Cylinder L/D = 1; Dia = 1/32 In.; Mass = 0.41×10^{-3} gram

Test Number	Aluminum Shield Thickness	Filler	Filler Density (lb/ft^3)	Velocity (fps)	Penetration (in.)	Remarks
5	0.003	2-in. Polyurethane	Closed cell 1.25	19,000	0.25	Projectile broken up by shield
6	0.010	1-in. Q-felt	3.5	16,600	0.5	Projectile broken up by shield
7	0.010	1-in. Q-felt	3.5	19,000	0.38	Projectile broken up by shield
8	0.010	2-in. Polystyrene	Closed cell 1.25	18,500	0.25	Projectile broken up by shield
9	0.003	2-in. Polystyrene	Closed cell 1.25	11,400	0.1	Projectile broken up by shield
10	0.005	2-in. Polystyrene	Closed cell 1.25	14,700	0.7	Projectile broken up by shield
11	0.005	2-in. Polyurethane	Closed cell 1.25	13,700	0.6	Projectile broken up by shield Filler shattered

Table A-3: FILLER MATERIAL

Test Number	Filler	Filler Density (lb/ft^3)	(4) Projectile	Velocity (fps)	Penetrati (in.)
12	Polystyrene	3.06 (5)	1/32 MgLi	16,100	0.4
13	Polystyrene	1.25 (5)	1/32 MgLi	17,700	0.75
14	Polystyrene	4.85 (5)	1/32 MgLi	17,800	0.35
15	Polystyrene	1.14 (5)	1/32 MgLi	14,600	1.4
16	Polystyrene	3.06 ( )	1/32 Al	15,100	2.0
17	Polystyrene	4.85 (5)	1/32 Al	14,300	0.32
18	Polystyrene	3.06 (5)	1/32 MgLi	18,400	0.5
19	Polystyrene	1.14 (5)	1/32 Al	14,700	2.0+
20	Polystyrene	1.25 (5)	1/32 Al	15,800	2.0+
21	Polystyrene	4.85 (5)	1/32 MgLi	15,700	
22	Polystyrene	1.14 (5)	1/32 MgLi	11,100	1.25
23	Polystyrene	1.25 (5)	1/32 MgLi	17,400	1.06
24	Dexiglass	169 (1)	1/32 Al	17,800	0.125
25	Dexiglass	169 (1)	1/32 Al	18,800	0.25+
26	Dexiglass	169 (1)	1/32 Al	17,800	0.50+
27	Dexiglass	169 (1)	1/32 Al	17,800	0.63+
28	Dexiglass	169 (1)	1/32 MgLi	20,200	0.25
29	Glass Wool	3 (2)	1/32 Al	16,500	1.25
30	Glass Wool	3 (2)	1/32 Al	18,000	1.25
31	Dexiglass	169 (1)	1/32 Al	18,400	1.25

(1) Aluminum foil density: 168.5 lb/ft^3; Dexiglass density: 0.876 lb/ft^3,
(2) Nominal density 3 lb/ft^3; Nominal thickness: 5 inches.
(3) Estimated.
(4) Cylindrical projectile: L/D = 1; Aluminum 1.02 × 10^{-3} gram; MgLi 0.
(5) Closed cell.

VALUATION — 1/32-INCH LIGHT-GAS GUN

n	Wt/Unit Area (lb/ft^2) (to stop projectile)	Thickness (in.)	Remarks
	102×10^{-3}	2	
	78×10^{-3}	2	
	141×10^{-3}	2	
	133×10^{-3}	2	
	510×10^{-3}	2	Just penetrated filler, no witness-sheet damage
	129×10^{-3}	2	
	128×10^{-3}	0.50	No witness-sheet damage
	190×10^{-3}	2	
		2	Penetrated, no breakup, crater in witness-sheet
		0.25	Projectile broke up in flight
		1.25	Penetrated, no breakup, crater in witness-sheet
	110×10^{-3}	1.06	Penetrated, no witness-sheet damage
		0.125+	12 glass, 13 Al foil, full penetration; witness-sheet crater 0.65 inch
		0.25+	24 glass, 50 Al foil, full penetration; witness-sheet crater
		0.50+	48 glass, 50 Al foil, full penetration; witness-sheet crater
		0.63+	60 glass, 61 Al foil, full penetration; witness-sheet shallow crater
	350×10^{-3}	0.50	48 glass, 49 Al foil, 22 sheets of aluminum foil penetrated
	310×10^{-3}	3	No witness-sheet damage
	310×10^{-3}	1.25	Minute pitting of witness sheet
	[illegible] $\times 10^{-3}$	1	96 glass, 97 Al foil, full penetration; 0.050-inch crater in witness sheet

10^{-3} gram

BLANK PAGE

Table A-4: SHIELD MATERIAL EVALUATION — 1/32-INCH LIGHT-GAS GUN

Test Number	Target	Target Damage Hole Dia (in.)	Projectile (1)	Velocity (fps)	Witness-Sheet Damage (3)
32	0.010 René 41	0.060	1/32 Al	12,600	Shallow craters inside 1-in. -dia circle; max crater dia 0.025 in.
33	0.010 René 41	0.047	1/32 MgLi	15,000 (2)	Shallow craters inside 0.7-in. -dia circle; max crater dia 0.030 in.
34	0.008 René 41	0.045	1/32 MgLi	15,200	Hemispherical craters inside 0.6-in. -dia circle; max crater dia 0.030 in.
35	0.008 René 41	0.060	1/32 Al	13,900	Shallow craters inside 0.8-in. -dia circle; 1 crater 0.030-in. dia; average crater dia 0.015 in.

(1) Cylindrical projectile; L/D = 1;
Aluminum 1.02×10^{-3} gram;
MgLi 0.41×10^{-3} gram.
(2) Estimated
(3) Target to witness-sheet spacing = 0.5 inch.

Table A-5: MATERIAL EVALUATION — MULTI

Test Number	Shield Material	Shield Thickness (in.)	Projectile Material	Projectile Diameter (in.)	Projectile Velocity (fps)
36	2024-T3	0.020	Al	1/8	24,400
37	2024-T3	0.040	Al	1/8	24,800
38	SS-301	0.063	Al	1/4	20,000
39	MgLi	0.040	Al	1/8	24,900
40	2024-T3	0.020	Al	1/8	21,500
41	6Al-4V Ti	0.016	Al	1/8	24,700
42	6Al-4V Ti	0.040	Al	1/8	24,500
43	6Al-4V Ti	0.040	Al	1/8	24,900
44	MgLi	0.040	Al	1/8	19,100
45	2024-T3	0.020	Al	1/8	16,500
46	2024-T3	0.020	Al	1/4	19,700
47	Tantalum	0.020	Al	1/8	25,400
48	Tantalum	0.020	Al	1/8	24,500
49	Tantalum	0.020	Al	1/8	19,800
50	Molybdenum (TZM)	0.012	Al	1/8	24,500
51	Molybdenum (TZM)	0.012	Al	1/8	24,100
52	Molybdenum (TZM)	0.012	Al	1/8	19,800
53	6Al-4V Ti	0.020	Al	1/8	24,400
54	6Al-4V Ti	0.056	Al	1/8	24,700
55	2024-T3	0.020	Al	1/4	18,900
56	2024-T3	0.020	Al	1/8	24,900

(1) Spherical projectiles (except as noted).
1/8-in. Al projectile mass = 0.05 gram.
1/4-in. Al projectile mass = 0.37 gram.
1/16-in. pyrex sphere mass = 5×10^{-3} gram.
1/8-in. foamed nickel cylinder mass = 0.086 gram.

PLE-SHIELD TESTS, 1/4-INCH LIGHT-GAS GUN

Witness Sheet Thickness (in.)	Shield Spacing (in)	Witness Sheet Spacing (in.)	Shield Damage Diameter (in.)	Diameter of Perforations (in.)	Witness Sheets Penetrated
0.020	2.5	1.0	0.225	1.5-2.0	1.7
0.020	2.5	1.0	0.31	2.2	1.1
0.020	2.5	1.0	0.505	5.4	4.2
0.020	2.5	1.0	0.30	1.4	1.9
0.020	2.5	1.0	0.21	1.8	1.9
0.020	2.5	1.0	0.20	1.2	2.0
0.020	2.5	1.0	0.20	Petals	4+
0.020	2.5	1.0	0.27	3.0	1.8
0.020	2.5	1.0	0.28	1.2	1.9
0.020	2.5	1.0	0.315	1.1	6.0
0.020	2.5	1.0	0.34	1.4	4.0
0.020	2.5	1.0	0.265	3.5	3.0
0.020	2.5	1.0	0.28	4.0	2.4
0.020	2.5	1.0	0.25	3.0	3.0
0.020	2.5	1.0	0.215	3.0	2.1
0.020	2.5	1.0	0.225	4.0	2.4
0.020	2.5	1.0	0.20	4.0	2.6
0.020	2.5	1.0	0.22	3.0	1.5
0.020	2.5	1.0	0.30	2.5	2.2
0.020	5.0	1.0	0.32	2.0	5.0
0.020	5.0	1.0	0.21	3.8	1.1

Table A-5

Test Number	Shield Material	Shield Thickness (in.)	Projectile Material	Projectile Diameter (in.)	Projectile Velocity (fps)
57	BeCu	0.005	Al	1/8	24,000
58	Soft Copper	0.012	Al	1/8	24,700
59	2024-T3	0.020	Al	1/4	20,500
60	Soft Copper	0.025	Al	1/8	25,000
61	1095 Steel	0.027	Al	1/8	19,500
62	1095 Steel	0.027	Al	1/8	20,400
63	1095 Steel	0.020	Al	1/8	22,800
64	1095 Steel	0.020	Al	1/8	24,000
65	SS-321	0.020	Al	1/8	22,500
66	6Al-4V Ti	0.040	Al	1/8	24,000
67	6Al-4V Ti	0.040	Al	1/8	23,500
68	6Al-4V Ti	0.040	Al	1/8	24,200
69	SS-321	0.020	Al	1/8	21,900
70	SS-321	0.020	Al	1/8	24,700
71	SS-321	0.032	Al	1/8	22,000
72	SS-321	0.032	Al	1/8	23,300
73	Tungsten	0.031	Al	1/8	24,600
74	SS-301	0.040	Al	1/8	19,900
75	SS-301	0.040	Al	1/8	24,800
76	SS-321	0.040	Al	1/8	24,600
77	Niobium	0.019	Al	1/8	24,700
78	Molybdenum (TZM)	0.050	Al	1/8	24,800
79	Molybdenum (TZM)	0.050	Al	1/8	24,400
80	Molybdenum (TZM)	0.012	Al	1/8	24,200
81	2024-T3	0.020	Al	1/8	24,900
82	2024-T3	0.020	Al	1/8	25,600
83	2024-T3	0.020	Al	1/8	25,700

(Cont.)

Witness Sheet Thickness (in.)	Shield Spacing (in.)	Witness Sheet Spacing (in.)	Shield Damage Diameter (in.)	Diameter of Perforations (in.)	Witness Sheets Penetrated
0.020	2.5	1.0	0.17	2.5	1.4
0.020	2.5	1.0	0.25	4.4	1.3
0.020	2.5	1.0	0.314	1.6	4+
0.020	2.5	1.0	0.30	4.4	1.4
0.020	2.5	1.0	0.27	4.5	2.3
0.020	2.5	1.0	0.27	4.0	2.1
0.020	2.5	1.0	0.26	5.0	2.5
0.020	2.5	1.0	0.265	5.0	2.3
0.020	2.5	1.0	0.240	4.6	2.1
0.020	2.5	1.0	0.325	4.5	3.0
0.020	2.5	1.0	0.345	4.5	2.1
0.020	2.5	1.0	0.34	4.5	2.0
0.020	2.5	1.0	0.25	4.2	2+
0.020	2.5	1.0	0.265	7.0	2.0
0.020	2.5	1.0	0.30	4.5	3.0
0.020	2.5	1.0	0.30	5.0	2.6
0.020	2.5	1.0	0.248	3.6	4.2
0.020	2.5	1.0	0.32 - 0.37	4.0	3.7
0.020	2.5	1.0	0.49	~8	5+
0.020	2.5	1.0	0.37	5.0	3.0
0.020	2.5	1.0	0.228	4.4	1.5
0.020	2.5	1.0	0.32	4.0	3.7
0.020	2.5	1.0	0.34	4.0	3.6
0.020	5.0	1.0	0.211	4.5	3.0
0.020	5.0	1.0	0.235	2.7	2.0
0.020	5.0	1.0	0.235	2.5	2.0
0.020	2.5	1.0	0.23	2.8	2.0

Table A-

Test Number	Shield Material	Shield Thickness (in.)	Projectile Material	Projectile Diameter (in.)	Projectile Velocity (fps)
84	Tantalum	0.020	Al	1/4	20,000
85	SS-301	0.063	Al	1/8	25,000
86	SS-301	0.050	Al	1/8	25,200
87	BeCu	0.005	Al	1/4	21,200
88	Lead	0.020	Al	1/8	24,800
89	Lead	0.032	Al	1/8	25,000
90	Lead	0.048	Al	1/8	25,400
91	2024-T3	0.020	Al	1/8	4,600
92	2024-T3	0.020	Al	1/8	10,300
93	SS-301	0.063	Al	1/4	20,100
94	Lead	0.025	Al	1/4	19,600
95	2024-T3	0.010	Pyrex	1/16	21,000
96	2024-T3	0.010	Pyrex	1/16	21,000
97	Molybdenum (TZM)	0.012	Al	1/4	20,200
98	2024-T3	0.020	Foamed Nickel	0.124x0.121	21,700
99	MgLi	0.063	Al	1/8	25,300
100	Magnesium	0.063	Al	1/8	24,500
101	6Al-4V Ti	0.063	Al	1/8	24,300
102	BeCu	0.063	Al	1/8	24,400
103	Tungsten	0.020	Al	1/8	24,400
104	Tungsten	0.006	Al	1/8	25,000
105	Tantalum	0.030	Al	1/8	25,100
106	Tantalum	0.010	Al	1/8	24,800
107	BeCu	0.020	Al	1/8	23,600
108	Magnesium	0.016	Al	1/8	24,600
109	2024-T3	0.020	Al	1/8	25,300
110	2024-T3	0.020	Al	1/8	25,500

5 (Cont.)

Witness Sheet Thickness (in.)	Shield Spacing (in.)	Witness Sheet Spacing (in.)	Shield Damage Diameter (in.)	Diameter of Perforations (in.)	Witness Sheets Penetrated
0.020	2.5	1.0	0.44	6.0	4.0
0.020	2.5	1.0	0.37	3.9	3.0
0.020	2.5	1.0	0.312	[illegible].1	2.8
0.020	2.5	1.0	0.273	4.2	5.1
0.020	2.5	1.0	0.35	---	0.7
0.020	1.5	1.0	0.437	1.9	2.0
0.020	2.5	1.0	0.52	---	0.4
0.020	2.5	1.0	0.132	0.15	4.0
0.020	2.5	1.0	0.173	0.19	3+
0.020	2.5	1.0	0.522	5.2-6.3	4.0
0.020	2.5	1.0	0.525	4.7	2.3
0.010	0.5	0.5	0.098	0.5	1.9
0.010	1.0	1.0	0.103	0.43	2.3
0.020	2.5	1.0	0.337	4.8	4.3
0.020	2.5	1.0	0.189x0.198	0.8	2.4
0.020	2.5	1.0	0.365	2.1	1.5
0.020	2.5	1.0	0.40	1.9	1.2
0.020	2.5	1.0	0.334	4.0	2.3
0.020	2.5	1.0	0.370	4.0	3.1
0.020	2.5	1.0	0.232	3.9	4.3
0.020	2.5	1.0	0.179	4.6	2.1
0.020	2.5	1.0	0.289	4.0	3.3
0.020	2.5	1.0	0.216	4.5	2.1
0.020	2.5	1.0	0.251	4.3	1.2
0.020	2.5	1.0	0.211	1.2	2.1
0.020	2.5	1.0	0.213	1.1	3.0
0.020	7.0	1.0	0.212	0.1	1.0

Test Number	Shield Material	Shield Thickness (in.)	Projectile Material	Projectile Diameter (in.)
111	SS-301	0.020	Al	1/8
112	SS-301	0.020	Al	1/8
113	SS-301	0.020	Al	1/8
114	Tungsten	0.020	Al	1/4
115	2024-T3	0.020	Foamed Al	1/4
116	2024-T3	0.020	Foamed Al	1/4
117	2024-T3	0.020	Al	1/16
118	2024-T3	0.020	Al	1/16

Table A-5 (Cont.)

Projectile Velocity (fps)	Witness Sheet Thickness (in.)	Shield Spacing (in.)	Witness Sheet Spacing (in.)	Shield Damage Diameter (in.)	Diameter of Perforations (in.)	Witness Sheets Penetrated
24,400	0.020	7.0	1.0	0.227	2.1	1.8
24,600	0.020	5.0	1.0	0.224	8.4	2.1
24,700	0.020	7.0	1.0	0.228	9.6	1.7
20,400	0.020	2.5	1.0	0.403	4.9	6.0
13,000	0.020	2.5	1.0	0.312	2.8	2.9
13,800	0.020	2.5	1.0	0.285	3.1	3.9
16,500	0.010	1.25	0.5	0.128x0.132	1.6	1.9
20,200	0.010	1.25	0.5	0.141x0.142	1.5	2.4

Table A-6. MATERIAL EVALU

Aluminum Projectiles: Cylinders L/D

Test Number	Shield Material	Shield Thickness (in.)	Projectile Velocity (fps)
119	Al	0.005	17,500
120	Al	0.005	16,600
121	Al	0.005	17,500
122	Al	0.005	18,200
123	Magnesium	0.020	17,000
124	Magnesium	0.025	17,200
125	Magnesium	0.040	15,700
126	Tungsten	0.002	18,100
127	Tungsten	0.006	17,500
128	Tungsten	0.010	18,700
129	2024-T3	0.010	18,700
130	2024-T3	0.020	18,600
131	2024-T3	0.025	17,200
132	2024-T3	0.032	18,400
133	Zinc	0.016	16,600
134	Zinc	0.020	17,000
135	MgLi	0.010	18,700
136	MgLi	0.040	18,900
137	MgLi	0.050	18,900
138	Tantalum	0.002	17,400
139	Tantalum	0.005	20,000
140	Tantalum	0.015	17,800
141	Lead	0.006	17,900
142	Lead	0.010	16,700

(1) All witness sheets penetrated.

(2) Steel projectile: Dia = 0.065 in.; Mass = 25 x 10-3

(3) Lexan cylindrical projectile: L/D = 3/4; Dia 0.0

TION — MULTIPLE-SHIELD TESTS, 1/16-INCH LIGHT-GAS GUN

1; Dia = 0.065 in.; Mass = 9.7 x 10^{-3} Gram; All Witness Sheets Aluminum

Shield Spacing (in.)	Witness-Sheet Thickness (in.)	Witness-Sheet Spacing (in.)	Shield Damage Diameter (in.)	Diameter of Perforations (in.)	Witness Sheets Penetrated
0.6	0.005	0.3	0.076	0.40	4.0
0.6	0.005	0.3	0.07	0.40	4.0
0.1	0.005	0.3	0.07	0.20	5.0
0.1	0.005	0.3	0.10	0.25	5.0
0.6	0.005	0.3	0.12	0.85	4.1
0.6	0.005	0.3	0.128	1.05	4.5
0.6	0.005	0.3	0.152	1.0	3.5
0.6	0.005	0.3	0.067	1.45	4+ (1)
0.6	0.005	0.3	0.089	1.25	10+ (1)
0.6	0.005	0.3	0.102	1.15	11+ (1)
0.6	0.005	0.3	0.107	1.2	4.0
0.6	0.005	0.3	0.144	1.2	3.8
0.6	0.005	0.3	0.152	1.2	4.0
0.6	0.005	0.3	0.170	0.95	3.5
0.6	0.005	0.3	0.153	1.1	3.5
0.6	0.005	0.3	0.163	1.0	3.5
0.6	0.005	0.3	0.106	0.80	4.0
0.6	0.005	0.3	0.16	0.85 - 0.95	3.9
0.6	0.005	0.3	0.185	1.10	3.0
0.6	0.005	0.3	0.077	1.4	7.0
0.6	0.005	0.3	0.100	1.3	7.0
0.6	0.005	0.3	0.122	1.22	13
0.6	0.005	0.3	0.121	1.15	3.8
0.6	0.005	0.3	0.148	0.98	3.2

gram.

5 in.; Mass = 2.97 x 10^{-3} gram.

Test Number	Shield Material	Shield Thickness (in.)	Projectile Velocity (fps)
143	Lead	0.017	18,100
144	BeCu	0.006	17,500
145	BeCu	0.010	18,400
146	BeCu	0.015	18,500
147	SS-301	0.006	17,300
148	SS-301	0.010	16,500
149	SS-301	0.016	17,500
150	BeCu	0.002	18,100
151	2024-T3	0.010	17,000
152	2024-T3	0.010	18,600
153	2024-T3	0.010	16,300
154	2024-T3	0.032	15,100
155	2024-T3	0.032	19,400
156	2024-T3	0.032	17,[illegible]00
157	2024-T3	0.032	18,200
158	SS-301	0.010	17,900
159	SS-301	0.010	14,800
160	SS-301	0.010	17,700
161	SS-301	0.032	18,300
162	SS-301	0.032	18,000
163	SS-301	0.032	18,700
164	2024-T3	0.010	16,600
165	2024-T3	0.010	17,300
166	2024-T3	0.032	17,200
167	2024-T3	0.032	17,600
168	SS-301	0.010	19,700
169	SS-301	0.010	18,400
170	SS-301	0.032	17,700
171	SS-301	0.032	18,400

Table A-6 (Cont)

Shield Spacing (in.)	Witness-Sheet Thickness (in.)	Witness-Sheet Spacing (in.)	Shield Damage Diameter (in.)	Diameter of Perforations (in.)	Witness Sheets Penetrated
0.6	0.005	0.3	0.203	1.15	3.0
0.6	0.005	0.3	0.093	1.4	3.1
0.6	0.005	0.3	0.107	1.4	3.1
0.6	0.005	0.3	0.124	1.45	5.0
0.6	0.005	0.3	0.081	1.45	4.6
0.6	0.005	0.3	0.097	1.45	8.6
0.6	0.005	0.3	0.120	1.63	8.5
0.6	0.005	0.3	0.068	0.7	4.0
0.3	0.010	0.3	0.072	0.34 - 0.42	3.4
1.0	0.005	0.3	0.103	1.45	3.2
1.5	0.005	0.3	0.088	2.1 - 2.6	4.2
0.3	0.005	0.3	0.126	0.63	4.7
1.0	0.005	0.3	0.163	1.6 - 1.9	2.3
1.0	0.005	0.4	0.142	0.94	3.9
1.5	0.005	0.3	0.146	3.2	2.2
0.3	0.005	0.3	0.112	0.65 - 0.85	5.0
1.0	0.005	0.3	0.098	1.63 - 1.73	8.9
1.5	0.005	0.3	0.098	2.90	7.7
0.3	0.005	0.3	0.130	1.0	3.8
1.0	0.005	0.3	0.133	1.6 - 1.9	9.8
1.5	0.005	0.3	0.130	3.2 - 4.6	10.7
0.6	0.005	0.5	0.085	0.96	3.7
0.6	0.005	0.7	0.093	0.86 - 1.08	4.0
0.6	0.005	0.5	0.153	1.0	3.1
0.6	0.005	0.7	0.142	1.15	3.3
0.6	0.005	0.5	0.108	1.2 - 1.25	6.0
0.6	0.005	0.7	0.101	1.3 - 1.43	5.0
0.6	0.005	0.5	0.128	1.6	6+ (1)
0.6	0.005	0.7	0.128	1.6 - 1.75	9+ (1)

Test Number	Shield Material	Shield Thickness (in.)	Projectile Velocity (fps)
172	2024-T3	0.010	19,400
173	2024-T3	0.010	19,200
174	2024-T3	0.010	19,500
175	SS-301	0.010	19,800
176	SS-301	0.032	19,600
177	2024-T3	0.010	19,600
178	SS-301	0.032	18,700
179	BeCu	0.063	18,800
180	Tungsten	0.032	19,600
181	Tungsten	0.002	19,800
182	Tungsten	0.006	12,900
183	Tungsten	0.010	18,200
184	2024-T3	0.050	19,100
185	SS-301	0.002	19,100
186	MgLi	0.050	17,400
187	Tantalum	0.032	20,200
188	SS-301	0.016	19,200
189	2024-T3	0.020	18,000
190	2024-T3	0.005	8,500 (2)
191	2024-T3	0.002	17,800
192	2024-T3	0.063	18,400
193	Tungsten	0.020	20,000
194	BeCu	0.032	18,600
195	2024-T3	0.005	19,000
196	2024-T3	0.040	17,000
197	Tungsten	0.030	20,400
198	MgLi	0.010	9,900 (3)
199	MgLi	0.010	22,100 (3)
200	MgLi	0.010	27,400 (3)

Table A-6 (Cont)

Shield Spacing (in.)	Witness-Sheet Thickness (in.)	Witness-Sheet Spacing (in.)	Shield Damage Diameter (in.)	Diameter of Perforations (in.)	Witness Sheets Penetrated
0.6	0.008	0.3	0.107	0.85	2.8
0.6	0.010	0.3	0.09	0.7	2.7
0.6	0.010	0.3	0.153	0.8	2.3
0.6	0.010	0.3	0.096	1.1	3.0
0.6	0.010	0.3	0.132	0.96	5.4
1.25	0.010	0.5	0.092	0.65 - 0.80	2.0
0.6	0.005	0.3	0.332	1.43 - 1.5	10.4
0.6	0.005	0.3	0.143	1.2 - 1.35	13.3
0.6	0.005	0.3	0.102	0.8 - 0.9	7.8
0.6	0.005	0.3	0.068	1.35 - 1.6	7.1
0.6	0.005	0.3	0.078	0.87 - 1.12	19.0
0.6	0.005	0.3	0.097	1.09	20+ (1)
1.25	0.010	0.5	0.169	1.3 - 1.35	2.0
0.6	0.005	0.3	0.065	1.17	4.8
0.6	0.005	0.3	0.168	0.9 - 1.15	4.5
0.6	0.005	0.3	0.147	1.15 - 1.43	11.6
1.25	0.010	0.5	0.108	1.8 - 2.48	3.7
1.25	0.010	0.5	0.115	1.3 - 1.5	2.0
0.3	0.005	0.3	0.067	0.34	43+ (1)
0.60	0.005	0.3	0.056	0.45 - 0.80	6.0
0.60	0.005	0.3	0.165	1.13 - 1.35	3.8
0.60	0.005	0.3	0.110	0.98	17.3
0.60	0.005	0.3	0.153	1.1 - 1.43	10.4
0.60	0.005	0.3	0.068	0.5 - 0.75	4.4
0.60	0.005	0.3	0.142	1.0 - 1.4	3.6
0.60	0.005	0.3	0.122	0.87	14.3
0.60	0.005	0.3	0.087	0.35	4.3 (3)
0.60	0.005	0.3	0.104	0.50	5.5 (3)
0.60	0.005	0.3	0.116	0.40	5.9 (3)

Table A-7: COMPOSITE CONFIGURATION TESTS — 1/32- AN

Projectiles

	Projectile				Range	Shield No. 1 (Al)		Filler		
Test Number	Material	Size (in.)	Weight (gram)	Velocity (fps)	Pressure (torr)	Thick. (in.)	Damage (in.)	Material	Thick. (in.)	Density (lb/ft^3)
201	MgLi	1/32	$4.1x10^{-4}$	17,800	5	0.003	0.042	Flexible Polyurethane	0.19	1.78
202	MgLi	1/32	$4.1x10^{-4}$	16,400	5	0.003	0.053	Flexible Polyurethane	0.19	1.78
203	MgLi	1/32	$4.1x10^{-4}$	18,100	5	0.003	0.040	Rigid Styrafoam	0.19	1.80
204	MgLi	1/32	$4.1x10^{-4}$	17,000	5	0.003	0.046	Rigid Styrafoam	0.19	1.80
205	Al	1/16	$9.7x10^{-3}$	12,400	40	0.005	0.10	Air	0.60	
206	Al	1/16	$9.7x10^{-3}$	17,700	40	0.005	0.10	Air	0.60	
207	Al	1/16	$9.7x10^{-3}$	17,200	0.20	0.005	0.10	Air	0.60	
208	Al	1/16	$9.7x10^{-3}$	17,600	40	0.005	0.070	Polyurethane foam	0.60	2
209	Al	1/16	$9.7x10^{-3}$	19,000	0.25	0.005	0.072	Polyurethane foam	0.60	2
210	Al	1/16	$9.7x10^{-3}$	17,300	40	0.005	0.075	Air	0.10	
211	Al	1/16	$9.7x10^{-3}$	18,600	1	0.005	0.076	Air	0.10	
212	Al	1/16	$9.7x10^{-3}$	16,000	0.1	0.005	0.070	Air	0.10	

1/16-INCH LIGHT-GAS GUNS (ALL SHIELDS ALUMINUM)

Cylinders L/D = 1

Shield No. 2			Filler			Skin		
Material	Thick. (in.)	Damage (in.)	Material	Thick. (in.)	Density (lb/ft^3)	Material	Thick. (in.)	Damage (in.)
						Al	0.005	0.13 x 0.16
						Al	0.010	0.026 x 0.072
						Al	0.010	0.10 x 0.16
						Al	0.005	0.12 x 0.22
Al	0.005	0.4x0.5	Polyurethane foam	0.80	2	Al	0.010	Buckled
Al	0.005	0.35x0.4	Polyurethane foam	0.80	2	Al	0.010	Blown out of jig
Al	0.005	0.25	Polyurethane foam	0.80	2	Al	0.010	Blown out of jig
Al	0.005	Blown in two	Air	0.80		Al	0.010	Dented
Al	0.005	1.5	Air	0.80		Al	0.010	Dented
Al	0.005	0.20	Polyurethane foam	0.80	2	Al	0.010	0.7 x 0.8
Al	0.005	0.20x0.25	Polyurethane foam	0.80	2	Al	0.010	1.0
Al	0.005	0.25	Polyurethane foam	0.80	2	Al	0.010	0.6

Table A-8: COMPOSITE CONFIGURA

	Projectile (10)				Shield No. 1			Filler		
Test Number	Material	Size (in.)	Weight (gram)	Velocity (fps)	Material	Thick. (in.)	Damage (in.)	Material	Thick. (in.)	Density (lb/ft^3)
213	Al	1/4	0.38	19,200	2024-T3	0.020	0.33	(1)	12	7.21
214	Al	1/4	0.38	19,800	2024-T3	0.020	0.325	(1)	5.5	7.15
215	Al	1/4	0.38	19,300	2024-T3	0.020	0.320	(1)	3.3	7.16
216	Al	1/4	0.38	19,700	2024-T3	0.020	0.320	(1)	1.5	7.13
217	Al	1/4	0.38	20,400	2024-T3	0.020	0.325	Air	2.5	
218	Al	1/4	0.38	19,900	2024-T3	0.040	0.410	Air	2.5	
219	Al	1/4	0.38	18,700	2024-T3	0.040	0.42	(1)	2.5	6.3
220	Al	1/4	0.38	19,600	2024-T3	0.040	0.405	(1)	2.5	6.3
221	Al	1/8	0.05	18,200	2024-T3	0.010	Sabot	Air	2.5	
222	Al	1/8	0.05	20,300	2024-T3	0.010	0.16	Air	2.5	
223	Al	1/8	0.05	23,500	2024-T3	0.010	0.16	Air	2.5	
224	Al	1/8	0.05	22,700	2024-T3	0.010	Sabot	Air	2.5	
225	Al	1/8	0.05	23,500	2024-T3	0.010	0.16	Air	2.5	
226	Al	1/8	0.05	24,700	2024-T3	0.010	0.30	Air	2.5	
227	Al	1/8	0.05	24,900	2024-T3	0.010	2.25	Air	2.5	
228	Al	1/8	0.05	25,400	2024-T3	0.010	0.16	Air	2.5	
229	Al	1/8	0.05	21,600	2024-T3	0.020	0.196	Air	2.5	
230	Al	1/8	0.05	25,000	2024-T3	0.020	0.24	Air	2.5	
231	Al	1/8	0.05	16,900	2024-T3	0.040	Sabot	Air	2.5	
232	Al	1/8	0.05	22,100	2024-T3	0.040	0.290	Air	2.5	
233	Al	1/8	0.05	23,400	2024-T3	0.040	Sabot	Air	2.5	
234	Al	1/8	0.05	25,100	2024-T3	0.040	0.30	Air	2.5	
235	Al	1/8	0.05	18,000	2024-T3	0.050	0.305	Air	2.5	
236	Al	1/8	0.05	24,500	2024-T3	0.050	0.33	Air	2.5	
237	Al	1/8	0.05	25,000	2024-T3	0.050	0.34	Air	2.5	

(1) Owens-Corning TW-F fiberglass wool.
(2) Johns-Manville microlite AA fiberglass.
(3) Johns-Manville unbonded B fiberglass.
(4) Closed-cell rigid polyurethane foam.
(5) Stafoam 1901.
(6) Honeycomb: 1/4-in. cell, 0.002-in.
(7) Open-cell flexible polyurethane foam.
(8) Bonded aluminum honeycomb.
(9) Bonded sandwich weighs 1.64 lb/ft^2 =
(10) Aluminum projectile-spheres and Le

TION TESTS — 1/4-INCH LIGHT-GAS GUN

Shield No. 2			Filler			Skin		
Material	Thick. (in.)	Damage (in.)	Material	Thick. (in.)	Density (lb/ft^3)	Material	Thick. (in.)	Damage
						2024-T3	0.050	None
						2024-T3	0.050	None
						2024-T3	0.040	Pitting, local deformation
						2024-T3	0.050	2.5- x 3.5-in. hole
2024-T3	0.020	1.4	(1)	3.4	4.4	2024-T3	0.040	Pitting, local deformation
2024-T3	0.020	1.8	(1)	3.4	4.4	2024-T3	0.040	Pitting, local deformation
2024-T3	0.020	4x4.5	Air	3.4		2024-T3	0.040	Melted glass
2024-T3	0.020	4x4.5	Air	3.4		2024-T3	0.040	Melted glass
2024-T3	0.020		Air	3.4		2024-T3	0.040	None
2024-T3	0.020	0.95	(1)	3.4	4.4	2024-T3	0.040	None
2024-T3	0.020	0.8	(1)	3.4	4.4	2024-T3	0.040	Pitting, melted glass
2024-T3	0.020	2x2.5	(1)	3.4	4.4	2024-T3	0.040	0.4-in. hole
2024-T3	0.020	2	(1)	3.4	4.4	2024-T3	0.040	Shallow dent
2024-T3	0.020	Petaling	(1)	1.5	4.4	2024-T3	0.040	Shallow dent
2024-T3	0.020	Petaling	(1)	1.5	4.4	2024-T3	0.040	Melted glass
2024-T3	0.020	1.15	(1)	1.5	4.4	2024-T3	0.040	Melted glass, local deformation
2024-T3	0.020	2x2.5	(1)	3.4	4.4	2024-T3	0.040	None
2024-T3	0.020	1.5	(1)	3.4	4.4	2024-T3	0.040	None
2024-T3	0.020	Sabot	(1)	3.4	4.4	2024-T3	0.040	None
2024-T3	0.020	2x2	(1)	3.4	4.4	2024-T3	0.040	None
2024-T3	0.020	3	(1)	3.4	3.1	2024-T3	0.040	Shallow dent
2024-T3	0.020	0.8	(1)	1.5	5.0	2024-T3	0.040	None
2024-T3	0.020	1.5	(1)	3.4	5.0	2024-T3	0.040	None
2024-T3	0.020	0.02	(1)	3.4	5.0	2024-T3	0.040	None
2024-T3	0.020	1.6x2.3	(1)	1.5	5.0	2024-T3	0.040	None

vall thickness.

an projectile-cylinders, L/D shown.

Table

	Projectile (10)				Shield No. 1			Filler		
Test Number	Material	Size (in.)	Weight (gram)	Velocity (fps)	Material	Thick. (in.)	Damage (in.)	Material	Thick. (in.)	Densit (lb/ft^3
238	Lexan	0.3x0.27	0.32	16,000	2024-T3	0.020	0.35	Air	2.5	
239	Al	3/16	0.162	16,200	2024-T3	0.050	0.365	Air	2.5	
240	Lexan	0.32x0.25	0.33	23,100	2024-T3	0.020	0.31x0.51	Air	2.5	
241	Al	1/4	0.38	28,100	2024-T3	0.020	0.31	Air	2.5	
242	Lexan	0.322x 0.25	0.31	17,900	2024-T3	0.020	0.33	Air	2.5	
243	Lexan	0.177x 0.25	0.16	18,600	2024-T3	0.020	0.335	Air	2.5	
244	Lexan	0.322x 0.25	0.31	22,900	2024-T3	0.020	0.465	Air	2.5	
245	Lexan	0.177x 0.25	0.22	22,600	2024-T3	0.020	0.345	Air	2.5	
246	Lexan	0.322x 0.25	0.31	22,400	2024-T3	0.020	0.43	Air	2.5	
247	Lexan	0.295x 0.25	0.27	21,400	2024-T3	0.020	0.335	Air	2.5	
248	Lexan	0.295x 0.25	0.27	22,500	2024-T3	0.020	0.340	Air	2.5	
249	Lexan	0.295x 0.25	0.27	19,000	2024-T3	0.020	0.435	Air	2.5	
250	Lexan	0.295x 0.25	0.27	19,700	2024-T3	0.032	0.390	Air	2.5	
251	Lexan	0.295x 0.25	0.27	22,400	2024-T3	0.040	0.42	Air	2.5	
252	Al	1/4	0.38	19,900	2024-T3	0.020	0.335	(2)	2.5	1.02
253	Al	1/4	0.38	20,000	2024-T3	0.020	0.34	(3)	2.5	0.85
254	Al	1/4	0.38	20,000	2024-T3	0.020	0.35	(2)	2.5	4
255	Al	1/4	0.38	20,100	2024-T3	0.040	0.44	(3)	2.5	4.2
256	Al	1/4	0.38	22,900	301 S S	0.020	0.24	(1)	2.0	4.2
257	Al	1/8	0.05	24,700	2024-T3	0.020	0.24	Air	1.5	
258	Al	1/8	0.05	24,700	2024-T3	0.020	0.22	(5)	1.5	2.0
259	Al	1/8	0.05	22,000	301 S S	0.020	0.207	(4)	2.5	1.98

A-8: (Cont)

Shield No. 2			Filler			Skin		
Material	Thick. (in.)	Damage (in.)	Material	Thick. (in.)	Density (lb/ft^3)	Material	Thick. (in.)	Damage
2024-T3	0.040	1.4	(1)	3.4	4.4	2024-T3	0.040	0.1-in local deformation
2024-T3	0.080	0.4x0.4	(1)	3.4	4.4	2024-T3	0.050	None
2024-T3	0.040	2.5x3	(1)	3.4	4.4	2024-T3	0.040	Small dimples
2024-T3	0.020	1.1	(4)	3.0	2.0	2024-T3	0.040	Complete failure
2024-T3	0.040	1.1	(1)	3.4	4.4	2024-T3	0.040	Pitting, local deformation
2024-T3	0.040	0.65	(1)	3.4		2024-T3	0.025	None
2024-T3	0.040	2x2.5	(1)	3.4		2024-T3	0.040	Pitting, large deformation
2024-T3	0.040	1.3x2	(1)	3.4		2024-T3	0.040	Pitting, large deformation
2024-T3	0.040	2	(1)	3.4		2024-T3	0.040	Pitting, large deformation
2024-T3	0.040	1x1.5	(1)	3.4		2024-T3	0.040	Pitting, large deformation
2024-T3	0.040	1x1.5	(1)	3.4		2025-T3	0.050	Pitting, large deformation
2024-T3	0.040	2x2.5	Air	3.4		2024-T3	0.040	Penetrated
2024-T3	0.040	2x2.5	Air	3.4		2024-T3	0.040	0.2-in. hole and craters
2024-T3	0.040	2x4	Air	3.4		2024-T3	0.040	Some local cratering
2024-T3	0.020	5	Air			2024-T3	0.040	2.2-in. hole
2024-T3	0.020	3x4	Air	3.4		2024-T3	0.040	Penetrated
2024-T3	0.020	Torn	Air	3.4		2024-T3	0.040	Dented
2024-T3	0.020	4.5	Air	3.4		2024-T3	0.020	Dented
7075-T6	0.040	5	(8)	2.0	9	7075-T6	0.040	Dented
2024-T3	0.020	1.2	(5)	1.5	2.0	2024-T3	0.025	Dented
2024-T3	0.025	2	(6)	0.62	4.0	2024-T3	0.025	Dented
2024-T3	0.020	Dented	Air	1.0		2024-T3	0.020	Dented

Test Number	Projectile (10) Material	Size (in.)	Weight (gram)	Velocity (fps)	Shield No. 1 Material	Thick. (in.)	Damage (in.)	Filler Material	Thick. (in.)
260	Al	1/4	0.38	19,800	2024-T3	0.020	0.34	(7)	1.5
261	Al	1/4	0.38	19,800	301 S S	0.020	0.36	(1)	2.0
262	Al	1/4	0.38	20,400	301 S S	0.020	0.37	(1)	2.0
263	Al	1/8	0.05	20,500	2024-T3	0.010	0.16	Air	0.75
264	Al	1/4	0.38	21,000	2024-T3	0.020	0.34	Air	1.5

Table A-8: (Cont)

	Shield No. 2			Filler			Skin		
Density (lb/ft^3)	Material	Thick. (in.)	Damage (in.)	Material	Thick. (in.)	Density (lb/ft^3)	Material	Thick. (in.)	Damage
1.5	2024-T3	0.025	2.5	(6)	0.62	4.0	2024-T3	0.025	4.5-in. hole
3.5	2024-T3	0.025	3.5	(6)	1.0	4.0	2024-T3	0.025	4-in. hole
4.2	2024-T3	0.025	3.5	(6)	2.0	4.0	2024-T3	0.025	1.3-in. hole
				(1)	1.5	4.0	2024-T3	0.025	Dented
				(1)	4.0	3.7	2024-T3	0.050	0.75-in. hole

Table

SPECIMEN							
Test Number	Material	Thickness (in.)	Stress (ksi)	Temperature (°F)	Cryogen Tank	Tank Contents	Materia
265	2014-T6	0.090	27.0	70	None		2014-T6
266	2014-T6	0.090	38.0	70	None		2014-T6
267	2014-T6	0.090	38.7	70	Yes	Air	2014-T6
268	2014-T6	0.090	30.9	-120	Yes	GN_2	2014-T6
269	2014-T6	0.090	30.7	-230	Yes	GN_2	2014-T6
270	2014-T6	0.090	37.8	-182	Yes	GN_2	2014-T6
271	2014-T6	0.090	39.0	-200	Yes	GN_2	2014-T6
272	2014-T6	0.090	45.5	-200	Yes	GN_2	2014-T6
273	2014-T6	0.040	51.5	-270	Yes	LN_2	7075-T6
274	2014-T6	0.040	40.7	-285	Yes	LN_2	7075-T6
275	2014-T6	0.040	35.3	-300	Yes	LN_2	7075-T6
276	2014-T6	0.040	22.4	-290	Yes	LN_2	7075-T6
277	2219-T62	0.100	25.5	70	None		7075-T6
278	2219-T62	0.100	33.1	70	None		7075-T6
279	2219-T62	0.100	40.3	70	None		2014-T6
280	2219-T62	0.100	9.9	-170	Yes	GN_2	2014-T6
281	2219-T62	0.100	24.7	-130	Yes	GN_2	2014-T6
282	2219-T62	0.100	38.3	-140	Yes	GN_2	2014-T6
283	2219-T62	0.100	49.7	-180	Yes	GN_2	2014-T6
284	2219-T62	0.100	40.1	-250	Yes	LN_2	7075-T6
285	2219-T62	0.100	66.1	-275	Yes	LN_2	7075-T6
286	2219-T62	0.100	19.3	-290	Yes	LN_2	None
287	2014-T6	0.040	0	-260	Yes	LN_2	None
288	2014-T6	0.090	0	-270	Yes	LN_2	None
289	2014-T6	0.100	0	-280	Yes	LN_2	None
290	2014-T6	0.100	0	-280	Yes	LN_2	None
291	2014-T6	0.090	0	-287	Yes	LN_2	None
292	2219-T62	0.100	0	-300	Yes	LN_2	None
293	2219-T62	0.100	0	300	Yes	LN_2	None

CF	Complete Failure	F-1	Failed One Side	NF	No Failure
DD	Doubler Delaminated	MF	Midsection Blown Out	RF	Rapid Fractur

-9: STRESSED-SPECIMEN TESTS — 1/4-INCH LIGHT-GAS GUN

SHIELD		PROJECTILE				IMPACT TEST		
Thickness (in.)	Space (in.)	Material	Sphere Diameter (in.)	Mass (gram)	Velocity (fps)	Hole Diameter (in.)	Damage Diameter (in.)	Crack Length (in.)
0.090	4.0	Al	1/4	0.38	20,000	0.4	3.0	5.0
0.090	4.0	Al	1/4	0.38	20,600	0	2.9	8.0
0.090	4.0	Al	1/4	0.38	20,400	0	2.8	4.2
0.090	4.0	Al	1/4	0.38	20,300	0	2.5	2.5
0.090	4.0	Al	1/4	0.38	20,900	0	2.7	2.5
0.090	4.0	Al	1/4	0.38	20,800	0.1	2.7	4.5
0.090	2.5	Al	1/4	0.38	20,600	2.5	2.1	8.0
0.090	2.0	Al	1/4	0.38	20,600	1.6	1.5	2.6
0.040	5.0	Al	1/4	0.38	20,800	2.0	3.4	8.0
0.040	5.0	Al	1/4	0.38	20,400	2.0	3.5	5.6
0.040	3.0	Al	1/4	0.38	20,600	2.0	2.2	8.0
0.040	3.0	Al	1/4	0.38	20,600	1.7	2.3	4.9
0.090	4.0	Al	1/4	0.38	20,700	0	2.8	1.7
0.040	5.0	Al	1/4	0.38	20.300	0.5	2.2	2.6
0.090	4.0	Al	1/4	0.38	20,600	0	2.8	2.0
0.090	4.0	Al	1/4	0.38	20,300	0	2.4	0.6
0.090	4.0	Al	1/4	0.38	21,000	0	2.5	0
0.090	4.0	Al	1/4	0.38	20,600	0	2.6	0.70
0.090	4.0	Al	1/4	0.38	20,500	0	2.8	0.6
0.020	4.0	Al	1/4	0.38	20,900	0.8	1.8	0
0.020	4.0	Al	1/4	0.38	20,000	0.7	1.9	2.0
		Al	1/4	0.38	20,700			8.0
		Al	1/4	0.38	21,000			8.0
		Al	1/8	0.05	18,400	0.3	None	0
		Al	1/8	0.05	25,000	0.4	None	0
		Al	3/16	0.16	24,000			8.0
		Al	1/4	0.38	20,000			8.0
		Al	3/16	0.16	24,600	0.55	None	0
		Al	1/4	0.38	19,500	0.6	None	0

SG = Slow Growth

	STATIC TEST (70°F)					
Failure Mode	Maximum Load (kips)	Gross Stress (ksi)	Net Stress (ksi)	Critical Crack (in.)	Slow Growth Crack (in.)	Failure Mode
F-1						
CF						
MF						
NF	28.1	39.0	55.0	2.9	2.9	RF
NF	22.4	31.1	41.5	2.6	2.6	RF
MF						
CF						
NF	28.0	38.9	53.3	2.75	2.8	SG
CF						
F-1						
CF						
F-1						
NF	26.6	33.3	45.0	2.1	2.1	SG
NF	23.3	29.2	66.8	4.5	4.5	SG
NF	23.9	29.9	45.9	2.8	2.8	SG
NF	29.5	36.9	57.9	2.9	2.9	SG
DD						
NF	36.6	45.8	49.0	0.7		RF
NF	34.0	42.5	48.5	1.0	1.0	RF
NF	28.8	36.0	64.0	3.5	3.5	SG
NF	29.4	36.8	49.0	2.0		RF
MF						
CF						
NF						
NF						
CF						
CF						
NF	35.0	43.8				
NF	32.5	40.7				

Table A-10: BIAXIAL-STRESSED-SPECIMEN TESTS –

	SPECIMEN					SHIELD	
Test Number	Thickness (in.)	Pressure (psia)	Stress (ksi)	Tank Contents	Temperature (°F)	Thickness (in.)	Material
294	0.127	0	0	LN_2	-320	None	
295	0.103	1010	27.5	(1)	-200	0.090	2014-T6
296	0.10	1030	28.0	(1)	-200	0.090	2014-T6

(1) Supercritical mixture.

- 1/4-INCH LIGHT-GAS GUN (11-INCH-DIA 2014-T6 SPHERICAL TANK)

	PROJECTILE					IMPACT TEST	
Spacing (in.)	Shape	Diameter (in.)	Material	Mass (gram)	Velocity (fps)	Impact Damage Diameter (in.)	Failure Mode
	Sphere	3/16	Al	0.16	24,000	0.60	Split
4	Sphere	1/4	Al	0.37	20,000	2.7	No failure
3	Sphere	1/4	Al	0.37	21,100	2.7	Catastrophic

Table A-11: PROPERTIES OF PROJECTILE AND SPECIMEN MATERIALS

Material	Density (gm/cm^3)	Yield Strength (ksi)	Ultimate Strength (ksi)	Melting Temperature (°F)	Sonic Velocity (fps)	Modulus of Elasticity (10^3 ksi)	Specific Heat (Btu/lb/°F)	Coefficient of Thermal Expansion (in./in./°F)
Foamed Aluminum	1.2							13.7 x 10^{-6}
2219-T62	2.77	37.3	55.8	930-1200	16,650	10.5	0.22	13 x 10^{-6}
2024-T3	2.77	50	70	935-1180	16,650	10.5	0.22	12.9 x 10^{-6}
2014-T3	2.77	61.5	69.1	950-1180	16,650	10.5	0.22	12.8 x 10^{-6}
Beryllium-Copper	8.24	25-35	60-80	1600-1800	13,100	19	0.10	9.3 x 10^{-6}
Niobium	10.8	35	40	4470	13,800	15	0.065	3.82 x 10^{-6}
Copper	8.95	10	32	1980	11,600		0.092	9.8 x 10^{-6}
Lead	11.3	1.6	2.2	620	3,620	2	0.031	16.3 x 10^{-6}
Magnesium	1.74	32	42	1050-1170	15,700	6.5	0.245	16 x 10^{-6}
Magnesium-Lithium	1.35	15-24	19-25	1070	18,000	6	0.346	21.8 x 10^{-6}
TZM Molybdenum	10.2	105	125	4750	17,400	46	0.061	3.1 x 10^{-6}
Foamed Nickel	2.52-3.6			2630				9.2 x 10^{-6}
Pyrex	2.2							
Sapphire	3.9							
301 Stainless Steel	7.84	40	110	2570	16,100	28	0.12	9.4 x 10^{-6}
321 Stainless Steel	7.92	30	90	2570	16,100	28	0.12	9.5 x 10^{-6}
1095 Steel	7.84	75-120	110-190	2570	16,750	29-30	0.10-0.11	8.1 x 10^{-6}
Tantalum	16.6	48	60	5425	11,000	27	0.036	3.6 x 10^{-6}
Titanium	4.73	137.8	142.9	2800-3000	16,400	15-17.5	0.135	5.8 x 10^{-6}
Tungsten	19.3	220	220	6170	14,200	59	0.034	2.5 x 10^{-6}
Zinc	7.14		20-25	790	12,100		0.094	19.3 x 10^{-6}

BLANK PAGE

APPENDIX B — QUALITY ASSURANCE

QUALITY ASSURANCE

The items manufactured under this program were the specimens used for testing in the Boeing hypervelocity ranges. The critical characteristics of these test specimens were material identification and thickness; the critical characteristics of the cellular or fibrous materials were their identification and density. These were verified, measured, and recorded as part of the test data log.

The thickness of plates and tensile specimens was measured to the nearest five ten-thousands of an inch using calibrated micrometers. A vidigage was used to measure thickness of the spherical specimens to the nearest half-thousandth of an inch in the impact area.

Suppliers were required to submit certified test reports, as applicable, containing data on material chemistry, physical properties, and density. Raw materials, manufacturing processes, and test specimens were inspected for conformance to engineering design specifications, and appropriate records have been documented. Test instruments were calibrated at regular intervals using primary standards maintained in the Boeing Metrology Laboratory. These standards are periodically calibrated by the National Bureau of Standards. Instrumentation performance was monitored daily.

Quality assurance records are identified, documented, and preserved in accessible form in accordance with standard Boeing policy. Test conditions were recorded for each test series on standardized data sheets to ensure that all relevant information necessary for evaluation of the test was obtained.

APPENDIX C — FRAGMENT DIAGNOSTICS

FRAGMENT DIAGNOSTICS

Commercial equipment adequate to establish the characteristics of the spray debris cloud emanating from a perforated sheet is not available. Therefore, a variety of instrumentation was designed, built, and used to measure temperature, pulse pressure, and fragment velocity during hypervelocity impact tests. The instrumentation and the progress achieved in improving the quality of the data is described in this appendix.

TEST SPECIMEN

Various target configurations were used, most of which consisted of 0.020- and 0.040-inch-thick aluminum plates separated from a solid backplate by various thicknesses and densities of fiberglass wool. A special test fixture, Figure C-1, was designed to hold the target material and instrumentation in the light-gas-gun test chamber.

INSTRUMENTATION

Three types of special instrumentation were used in this test series. These consisted of temperature measurement by a series of thermocouples on a thin plate behind the fiberglass, measurement of the shock-wave velocity as it progressed through the fiberglass, and dynamic measurement of pressure caused by the shock wave in the fiberglass hitting the solid backplate. Each of these will be considered in the following discussion.

Temperature

For the series of temperature measurement tests, several aluminum plates (0.010- and 0.020-inch thick) were fabricated with 24 thermocouples welded in place. The thermocouple pattern is shown in Figure C-2. Each of the first six thermocouple plates were actually two plates in one, the upper half 0.010-inch thick and the lower half 0.040-inch thick. Some tests were run with the entire plate either 0.030- or 0.040-inch thick.

The photocell and pulse generator were part of the light-gas-gun instrumentation setup. Their purpose was to establish a reference point in time for the particle position as it traveled in the vacuum chamber before hitting the target. Knowing the particle velocity, the time of impact could be calculated and compared with the time the first data appeared.

The d.c. source and vacuum-tube voltmeter were used to supply a calibration voltage to the tape. This voltage was equivalent to a calibrated temperature and appeared in the data readout.

Figure C-1: TEST FIXTURE AND COMPOSITE SPECIMEN

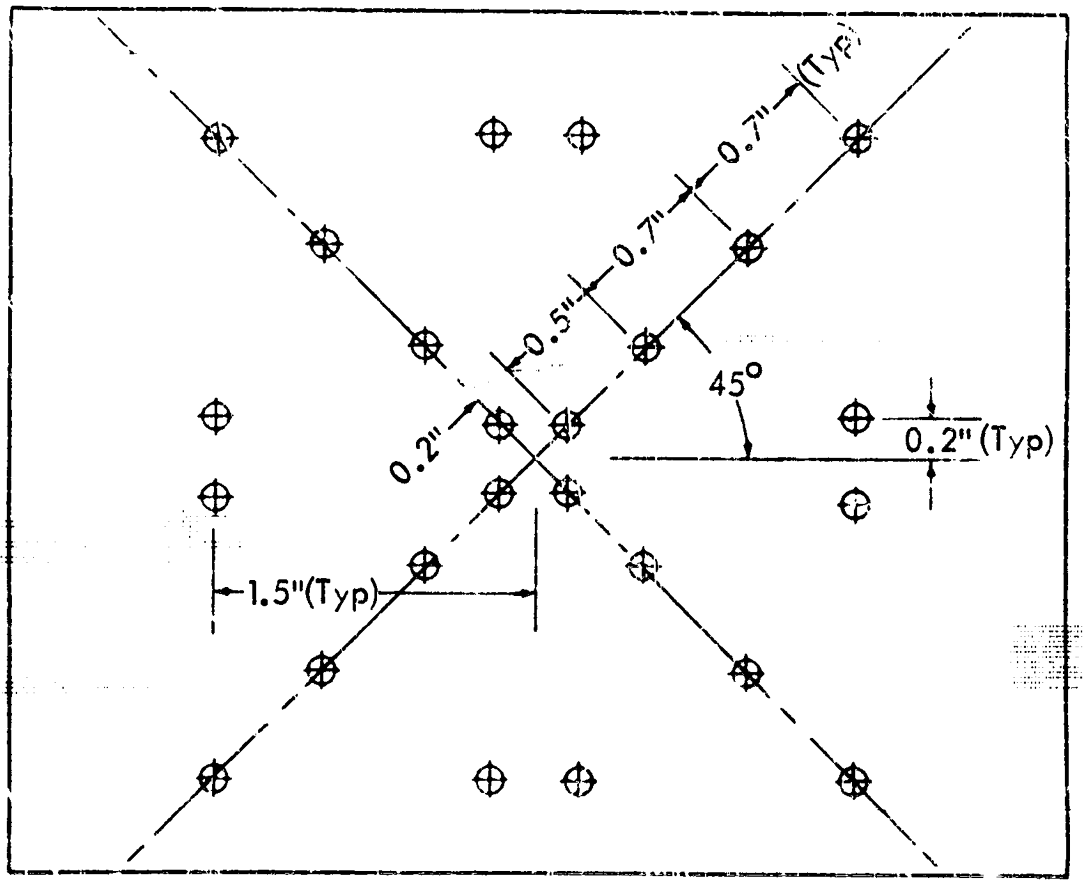

Figure C-2: THERMOCOUPLE LOCATIONS

Data reduction for temperature was obtained by slowing the tape recorder by a factor of 16:1 and making an oscillograph record of the data. Temperatures were then read by direct measurement of the oscillograph.

Velocity

A special probe was constructed to measure the propagation velocity of the penetrating disturbance in the specimen. This probe consisted of four pairs of closely-spaced wire rings mounted on a conical probe extending from the backplate of the specimen into the glass wool. Figure C-3 shows a probe and associated thyratron tubes. The outer rings of all pairs were connected together to a source of +60 volts d.c. The inner ring of each pair was connected to the grid of a thyratron (2D21) tube, which was held at cutoff by a -6-volt bias acting through a a 5-megohm resistor. The voltage across the 50-ohm cathode resistor was applied to a tape recorder operating at 60 ips, giving a rise time of approximately 1 microsecond.

The operation of this instrumentation was based on the assumption that the shock wave disturbance in the glass wool would be sufficient to ionize some of the surrounding material. This in turn would allow conduction between the wire rings to overcome the thyratron's 6-volt grid bias.

Pressure

The initial pressure measurement tests used pressure transducers that consisted of a solid steel piston mounted on the back of the test fixture through a hole into the test fixture interior. Strain gages, connected in a four-arm bridge circuit, were cemented to the piston base. Figure C-4 shows the transducer installation in the test fixture.

After the initial test shots, the test fixture was modified so the transducer base could not be accelerated backwards before the pressure pulse reached the end of the transducer. The transducer tip protruded through the second 3/4-inch-thick plate, which was relatively free to deflect without affecting the mounting plate. New transducers were designed and installed as shown in Figures C-5 and C-6.

After a question arose as to the validity of the transducer's static force calibration used for dynamic excitation calibration, a transducer was designed so that a 2-pound weight could be screwed directly to the end of the piston. The transducer was placed on a shaker and vibrated at a resonance such that the weight experienced 500 g's peak. This is equivalent to a peak force of 1000 pounds, or a dynamic pressure of about 10,000 psi, since the area of the piston is 0.1 square inch. The resonant frequency of the weight and piston was approximately 4000 cps. Six millivolts (mv) peak was obtained from the strain-gage bridge. The piston was then subjected to 100 pounds of static force and again 6 mv (±5 percent) were obtained from the strain-gage bridge. This meant that a static

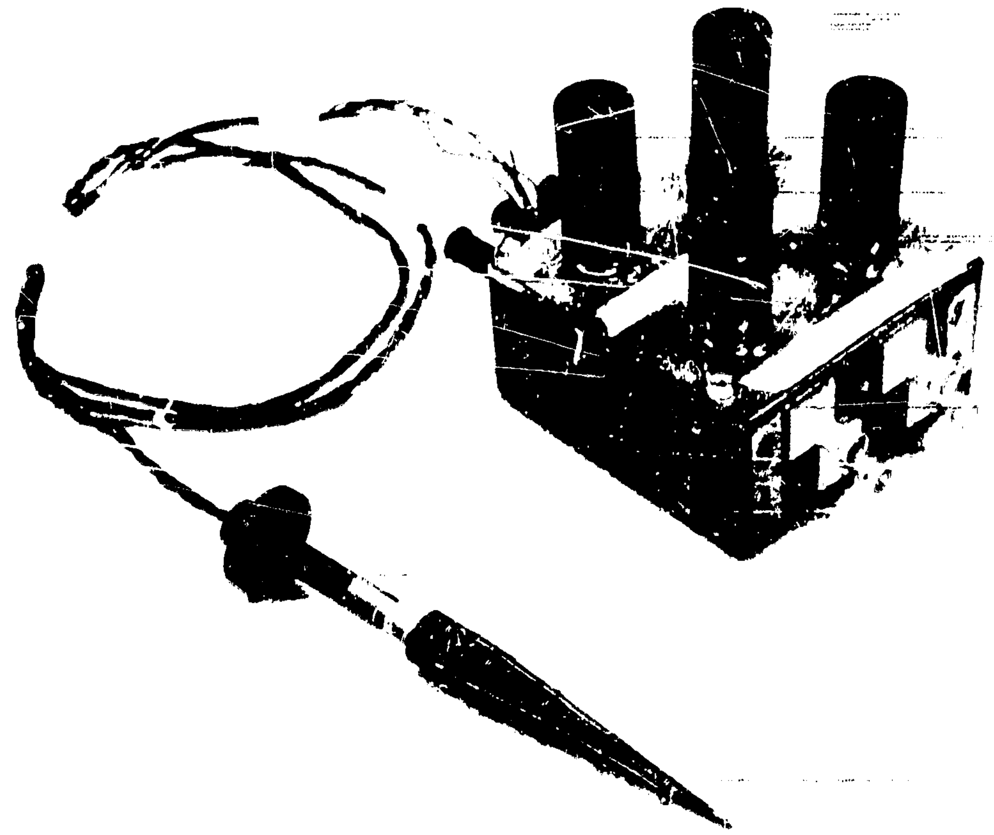

Figure C-3: VELOCITY MEASURING PROBE AND THYRATRON TUBES

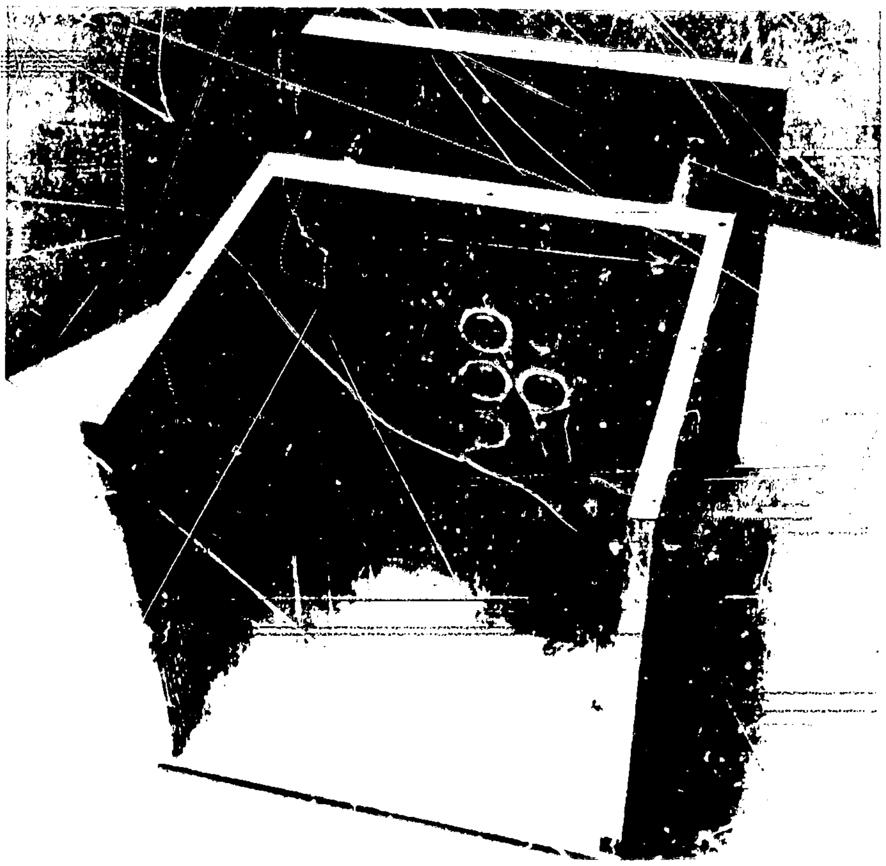

Figure C-4: TEST FIXTURE SHOWING PRESSURE TRANSDUCERS

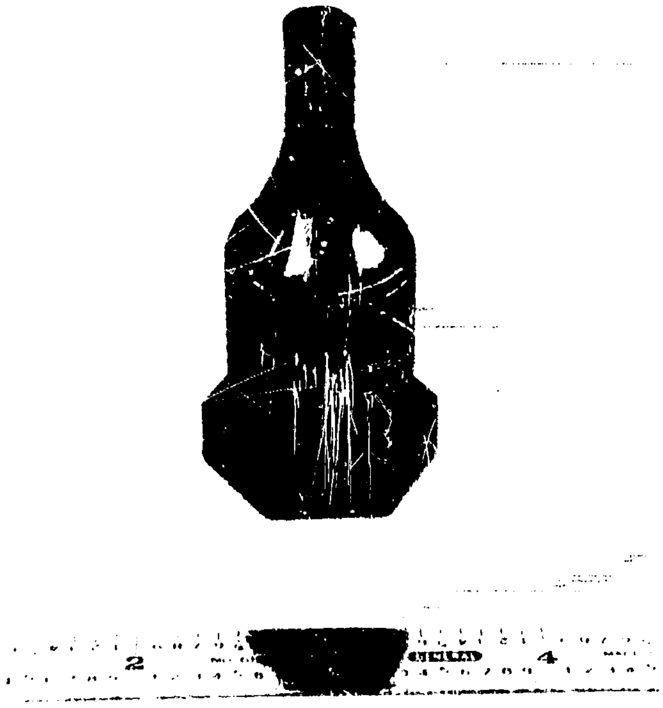

Figure C-5: MODIFIED PRESSURE TRANSDUCER
STRAIN GAGES NOT SHOWN

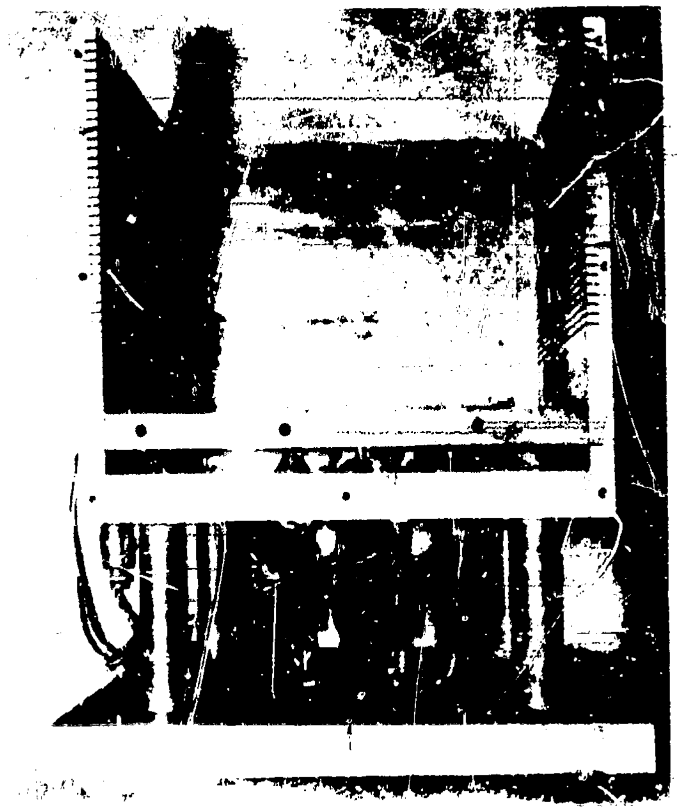

Figure C-6: INSTALLATION OF MODIFIED PRESSURE TRANSDUCERS calibration would hold for dynamic loads up to 10,000 psi at 4000 cps within the required accuracy of the measurement to be made.

TEST RESULTS AND DISCUSSION

Temperature Data

All temperature data for a series of 10 test shots were tabulated with pertinent test configuration information and plotted. The temperature curves were extremely difficult to plot to any resemblance of smooth contours. This appeared to indicate that hot particles were hitting the plates, resulting in hot spots and a nonuniform temperature pattern. Figure C-7 shows a typical contour for a successful shot.

Velocity Data

Velocity data for a series of four shots are plotted in Figure 28. The significance of these data has been discussed previously (see section entitled "Fragment Velocity").

Pressure Data

An interesting aspect of the first series of tests using the original transducers was that the FM-recorded indicated pressure went negative before going positive, whereas the direct-recorded indicated pressure went positive. The negative pulses lasted about 30 microseconds, after which there was some oscillation (12,000 to 18,000 cps) about the zero point. After approximately 3 milliseconds, another pulse appeared, also in the negative direction in most of the FM-recorded channels. This behavior of the negative pulse appearing just after impact may have been the result of the transducer and the recording system's inability to respond to an extremely short-duration pulse (shorter than 10 microseconds), in which case the first shock pulse would not be observed. An evaluation should be made to determine the recording characteristic of the pressure data system when subjected to various pulse widths.

A series of five tests was performed using the redesigned pressure transducers. The pressure data recorded for this series were very noisy. This was taken to be indicative of loose strain gages. Subsequent static testing showed the bond holding the strain gages to the pistons had indeed failed under impact. No further tests using these instruments were performed.

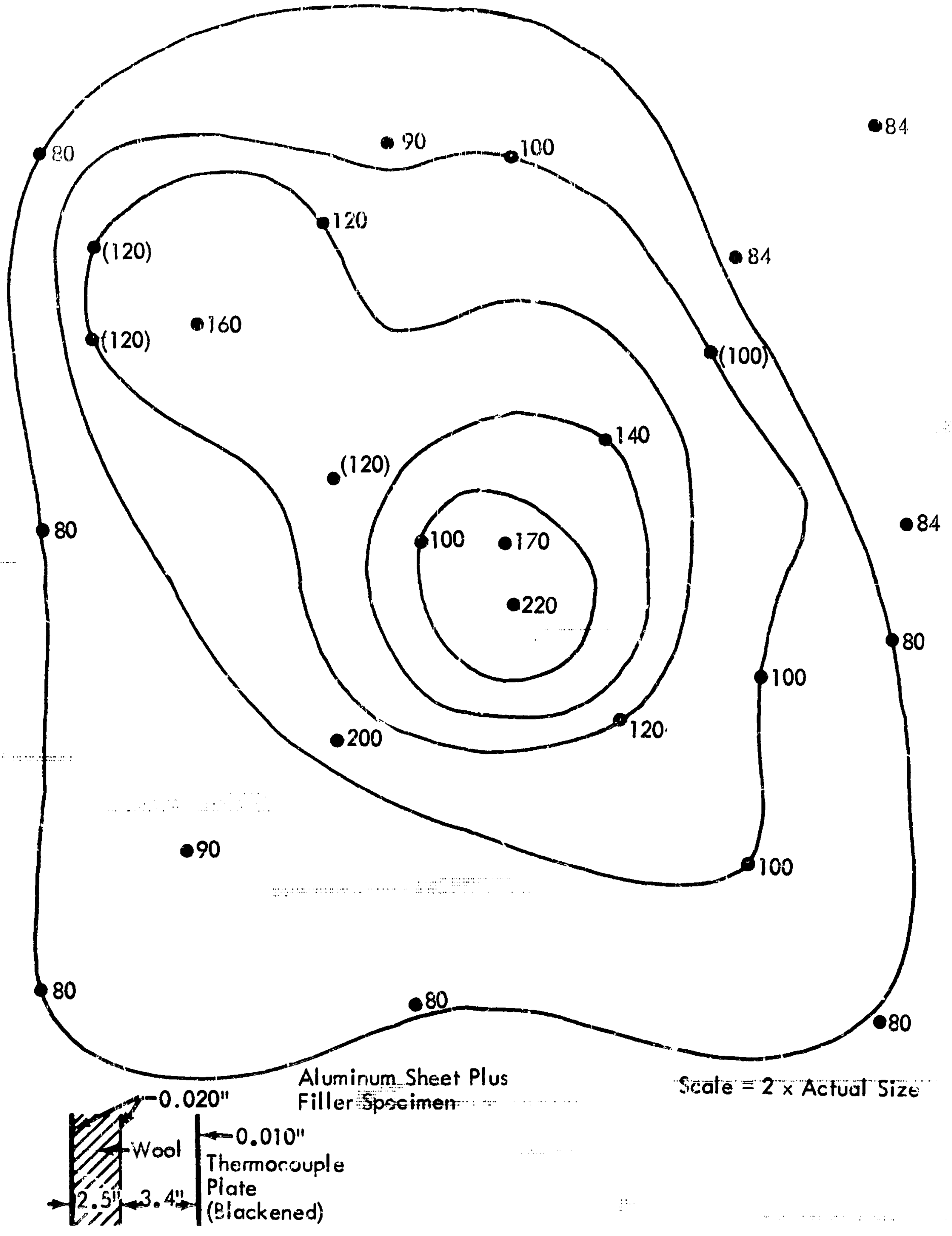

Figure C-7: TEMPERATURE CONTOURS — 0.75 MS AFTER IMPACT
1/4 — INCH ALUMINUM PROJECTILE AT 19,900 FPS

FINAL REPORT DISTRIBUTION LIST

"Meteoroid Protection for Spacecraft Structures"

Contract NAS3-2570

The Boeing Company

National Aeronautics and Space Administration
Lewis Research Center
21000 Brookpark Road
Cleveland, Ohio 44135

		Copies
Attn:	Contracting Officer, Mail Stop 500-210	1
	Liquid Rocket Technology Branch, M.S. 500-209	3
	Gordon T. Smith, M.S. 500-209	5
	Technical Report Control, M.S. 5-5	1
	Technology Utilization Office, M.S. 3-16	1
	AFSC Liaison Office, M.S. 4-1	2
	Library	2

National Aeronautics and Space Administration
Langley Research Center
Langley Station
Hampton, Virginia 23365

Attn:	E. R. Gilman, Librarian	2
	D. Davis, Jr.	1
	J. R. Dawson	1
	R. Heldenfels	1
	W. Kinard	1
	E. T. Kruszewski	1
	R. S. Osborne	1
	J. Williams	1

National Aeronautics and Space Administration
Ames Research Center
Moffett Field, California

Attn:	D. E. Gault	1
	C. R. Nysmith	1
	J. L. Summers	1
	Library	2

National Aeronautics and Space Administration
George C. Marshall Space Flight Center
Huntsville, Alabama

Attn:	Technical Documents Library	1
	Research Projects Division (M-RP-R)	1

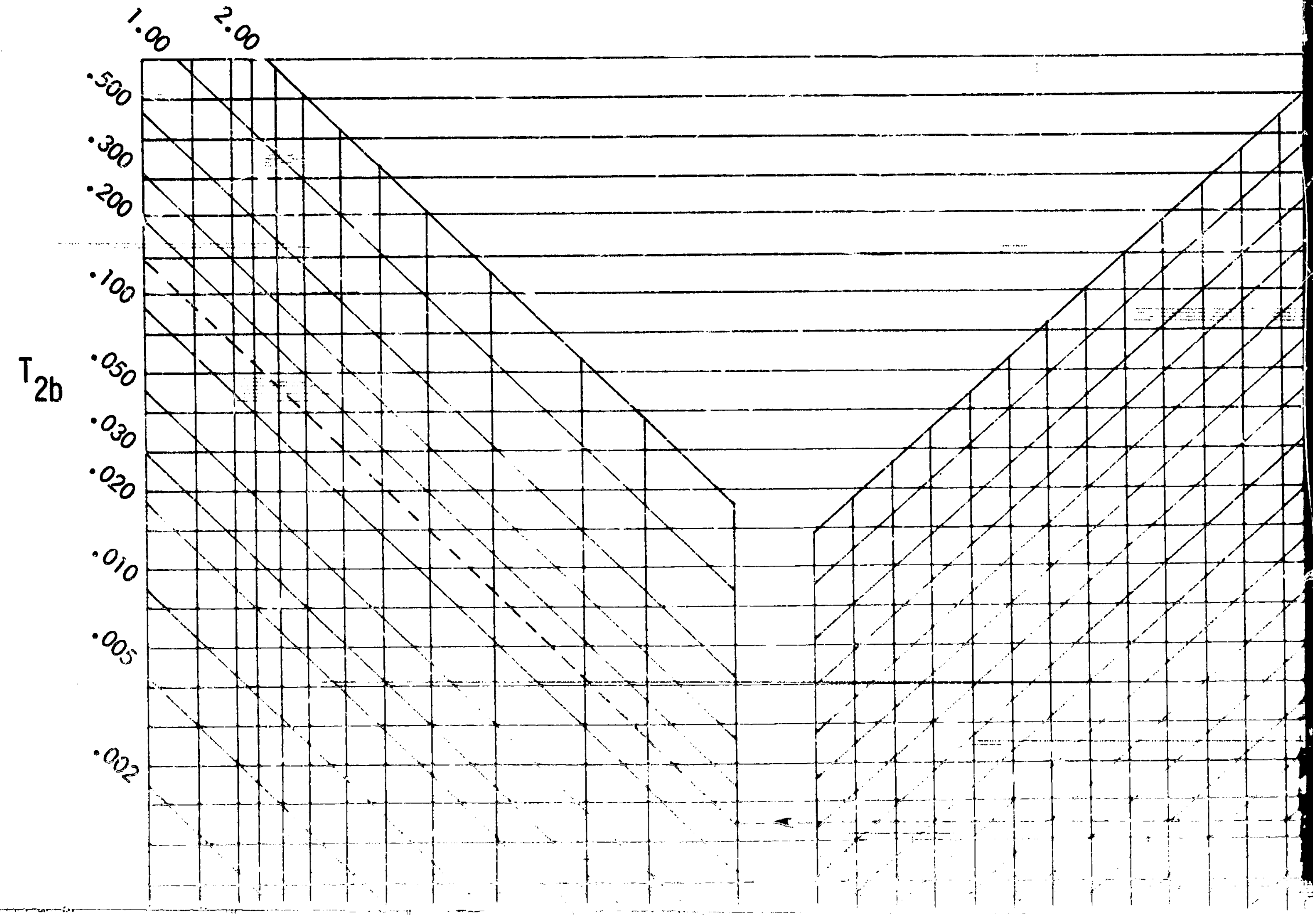
1.00
2.00
.500
.300
.200
.100
.050
.030
.020
.010
.005
.002
T_{2b}

2

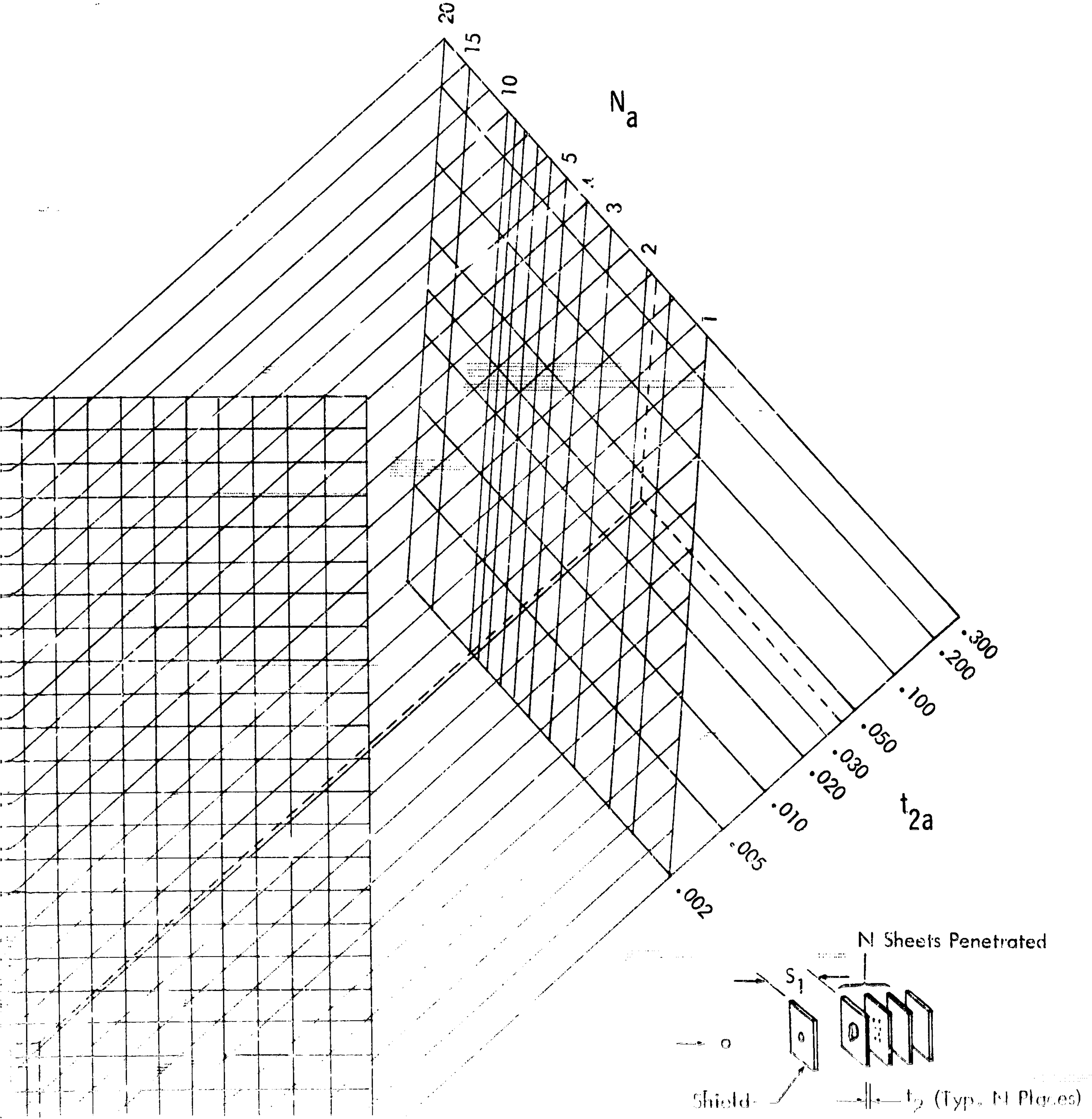
20
15
10
5
4
3
2
1
N_a
.300
.200
.100
.050
.030
.020
.010
.005
.002
t_{2a}
N Sheets Penetrated
S_1
Shield
t_2 (Typ. N Places)

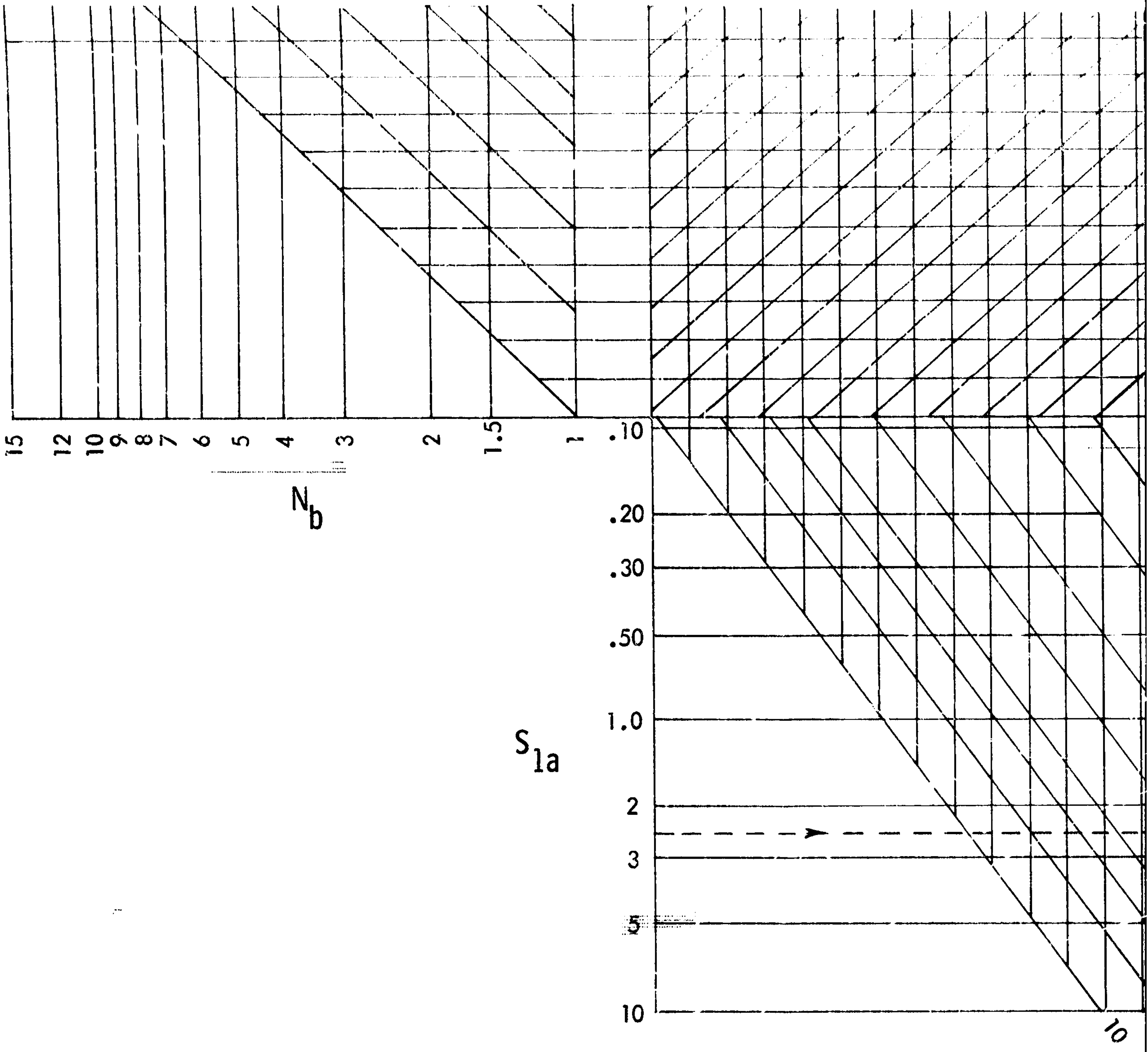
15
12
10
9
8
7
6
5
4
3
2
1.5
1
N_b
.10
.20
.30
.50
1.0
S_1a
2
3
5
10
10

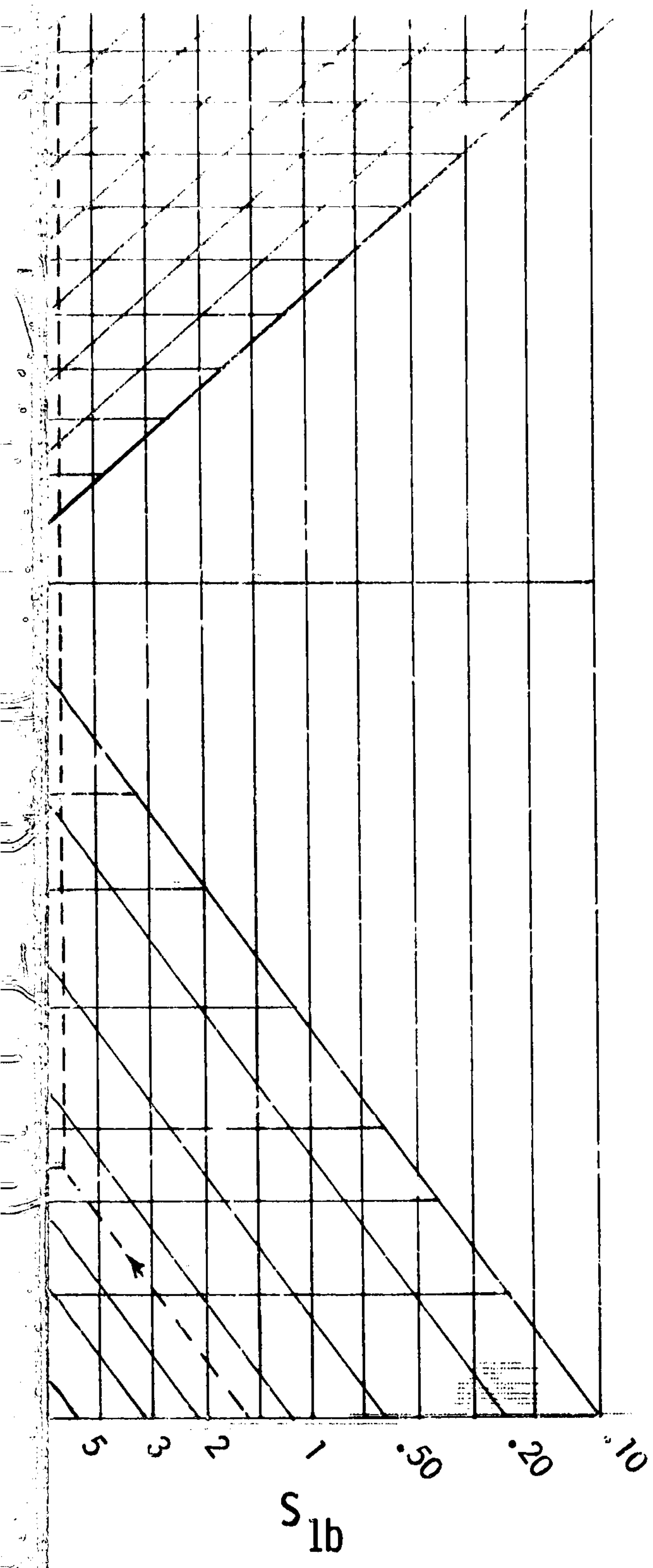

Subscript a – Test Configuration
Subscript b – Req'd Configuration
t_3 = Thickness of Third Sheet in a Three Sheet Barrier

Directions

1. For aluminum projectiles into aluminum shields –
   a. Assume S_{1a}, t_{2a}, and N_a are known from a test having the same shield as that required and impacted by a similar projectile at the same velocity.
   b. Enter with known & required quantities as shown in the example.
   c. To design a two-sheet structure, let $N_b = 1$. For a three-sheet structure, find N_b for the required t_{2b}. To find the required t_{3b}, re-enter chart letting $t_{2a} = t_{2b}$ and $N_a = 1$. For a new $N_b = 1$, t_{3b} is given on the t_{2b} line.
2. For aluminum projectiles into any metallic shield-follow the same procedure as above, except S_{1b} must equal S_{1a}.
3. Apply safety factor as required
4. This chart not applicable for projectile velocities less than 15,000 fps.

Example –

For S_{1a} = 2.5" & t_{2a} = 0.040", a test showed N_a = 1.8. It is required that the spacing S_{1b} = 1.5" and that the projectile stop on the sheet following the shield (N_b = 1). Following the arrows on the chart, it is seen that t_2 required = 0.15".

EXPERIMENTAL DETERMINATION OF MULTISHEET BARRIERS

Top

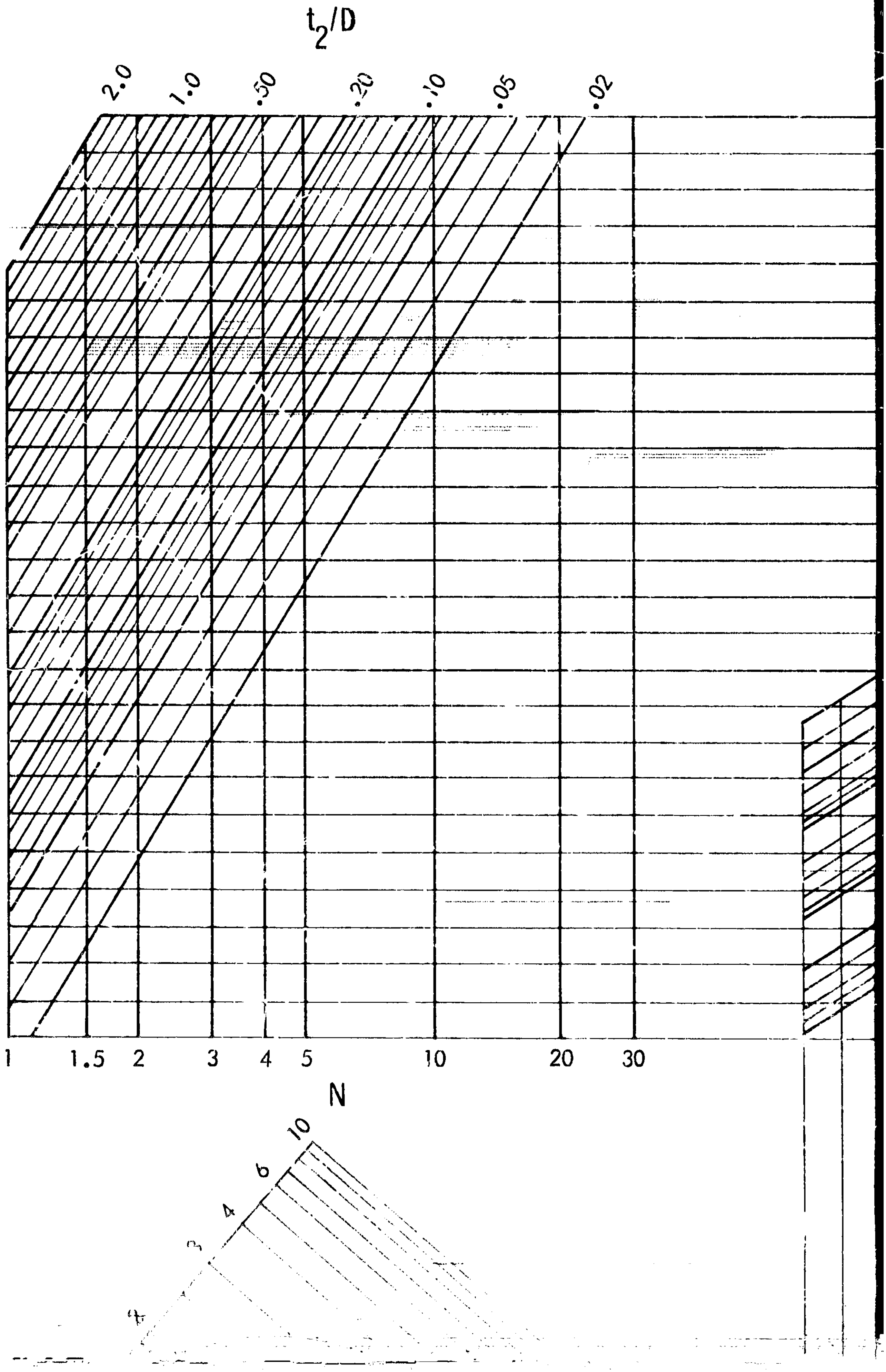

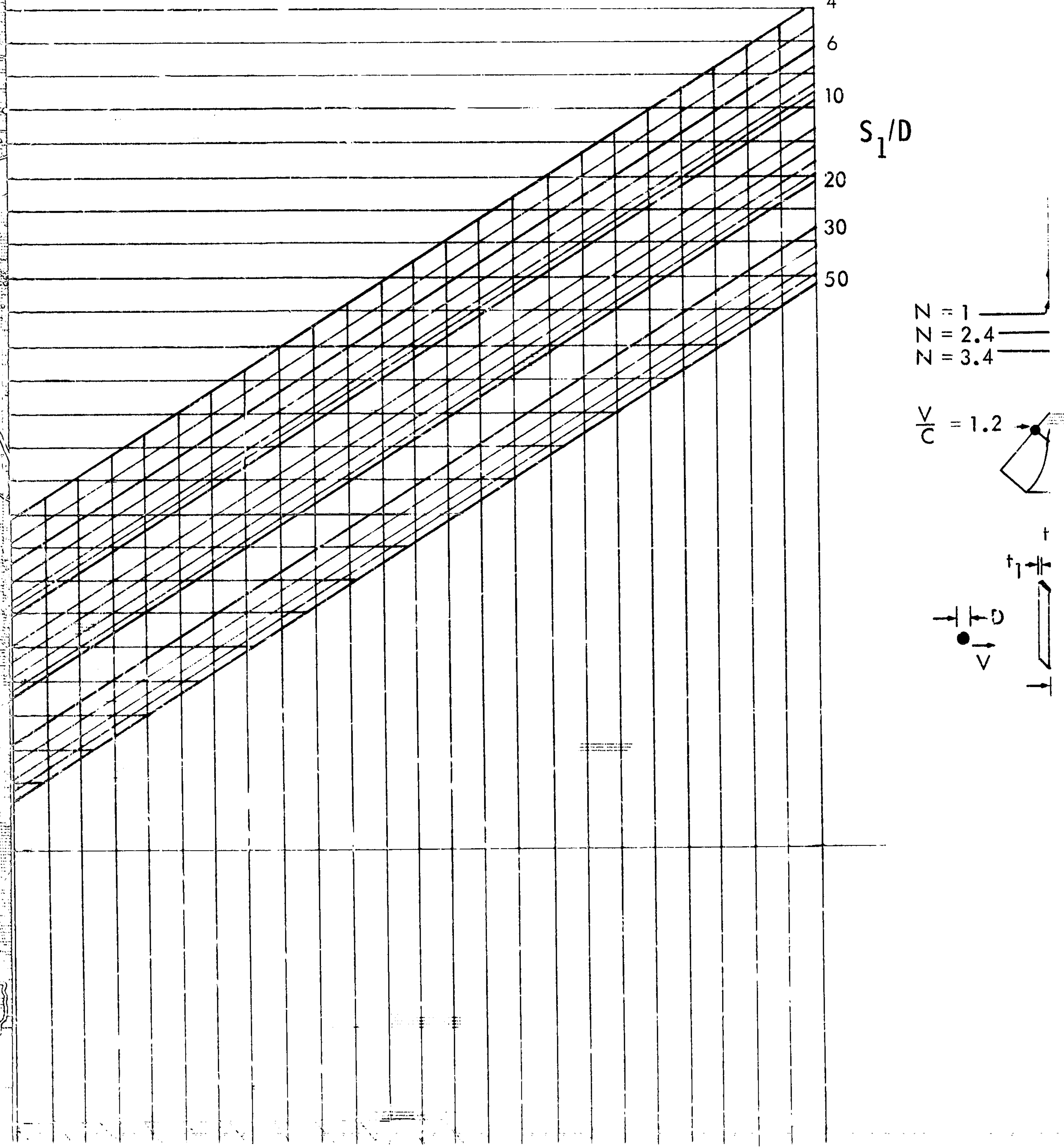
4
6
10
S$_1$/D
20
30
50
N = 1
N = 2.4
N = 3.4
V/C = 1.2
t
t$_1$
D
V

[illegible]

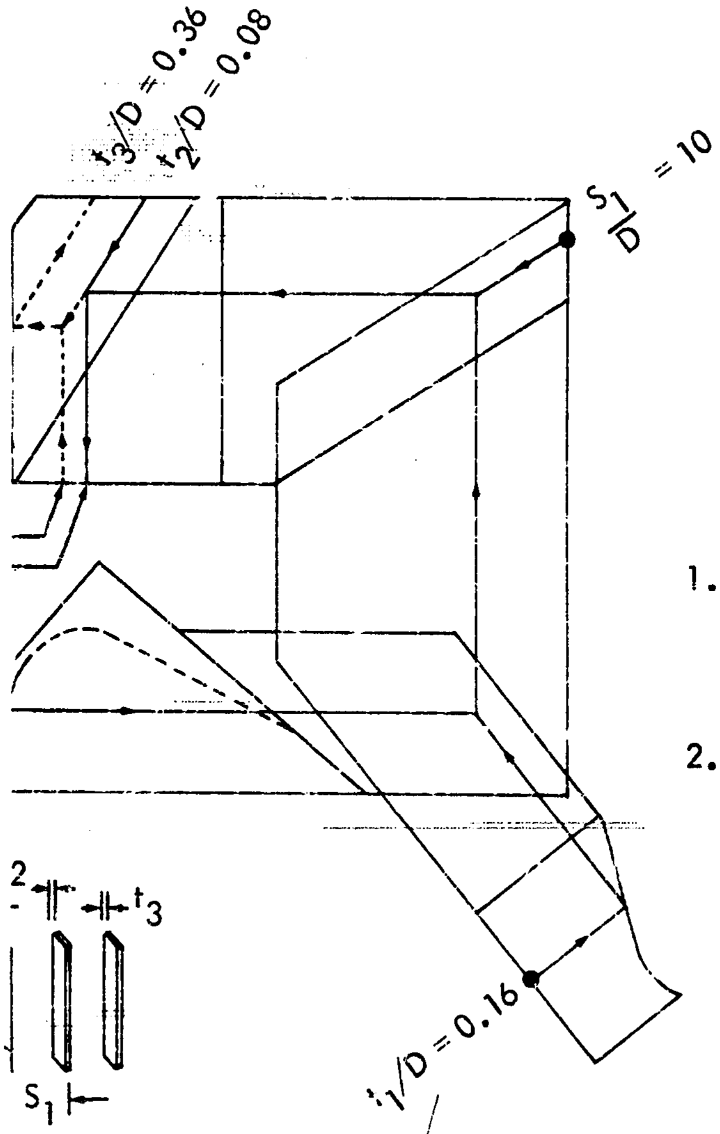

EXAMPLE 1 - DESIGN OF THIRD SHEET OF A THREE-SHEET BARRIER

1. Find number sheets penetrated if there were a series of sheets of thickness t_2 following the shield. Enter nomogram at $t_1/D = 0.16$, $V/C = 1.2$, $S_1/D = 10$ ~~and~~ $t_2/D = 0.08$. The result is N = 3.4.

2. All but one of these sheets must be combined into one sheet of equivalent penetration resistance. Enter the nomogram at the number sheets to be combined (N = 2.4) and $t_2/D = 0.08$. Move horizontally to the desired N (one) and read off the required t_2/D.

EXAMPLE	GIVEN	STEP 1	STEP 2
D	0.25		
V/C	1.2	1.2	
t_1/D	0.16	0.16	
S_1/D	10	10	
t_2/D	0.08	0.08	0.08
t_3/D	?	0.08	0.36
N		3.4	2.4
PENETRATION	3 SHEET REQ'D	5	3

2/D = 0.148

/D = 0.074

BLANK PAGE

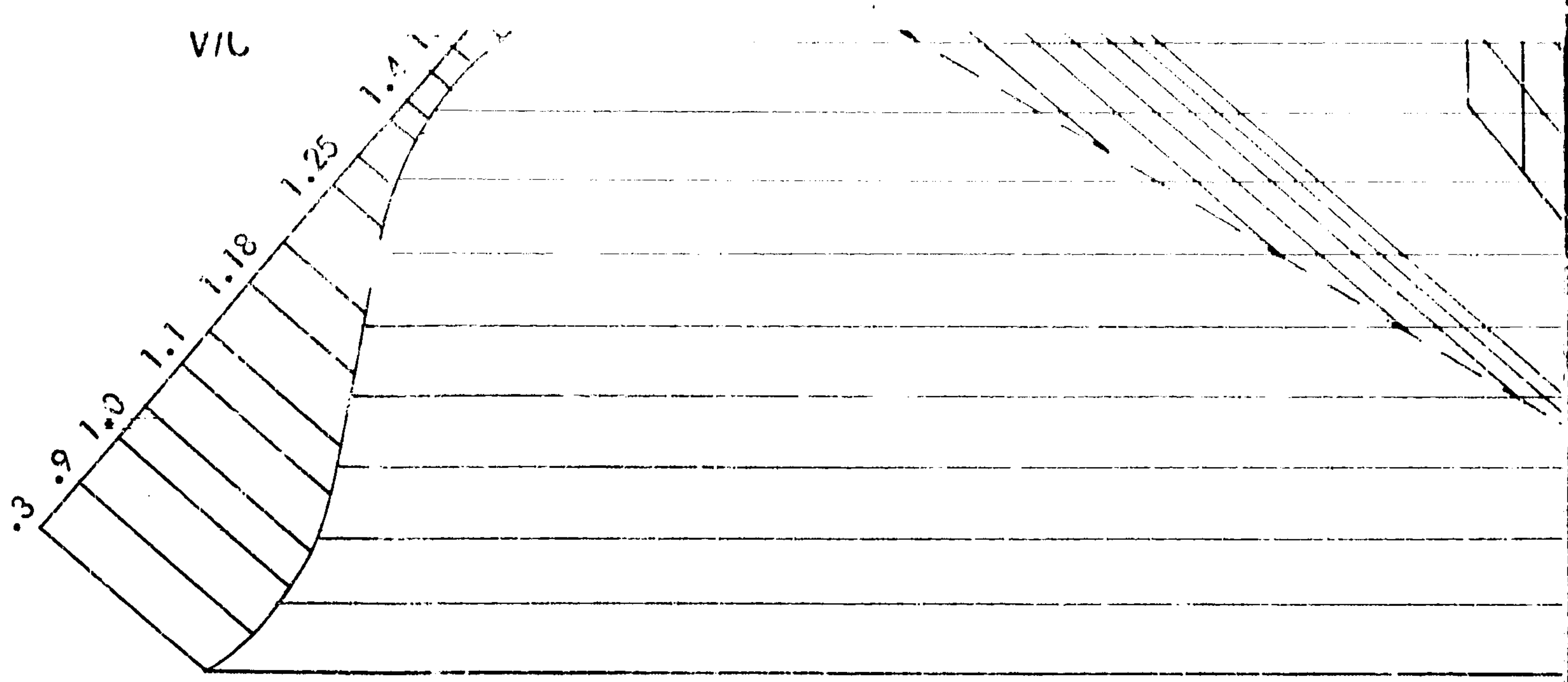

V = Meteoroid Velocity
C = Speed of Sound in Shield (first sheet)
D = Meteoroid Diameter
S_1 = First to Second Sheet Spacing
t_1 = First Sheet (shield) Thickness
t_2 = 2nd Sheet Thickness
t_3 = 3rd Sheet Thickness
N = Number of Sheets Penetrated Beyond Shield (first sheet)

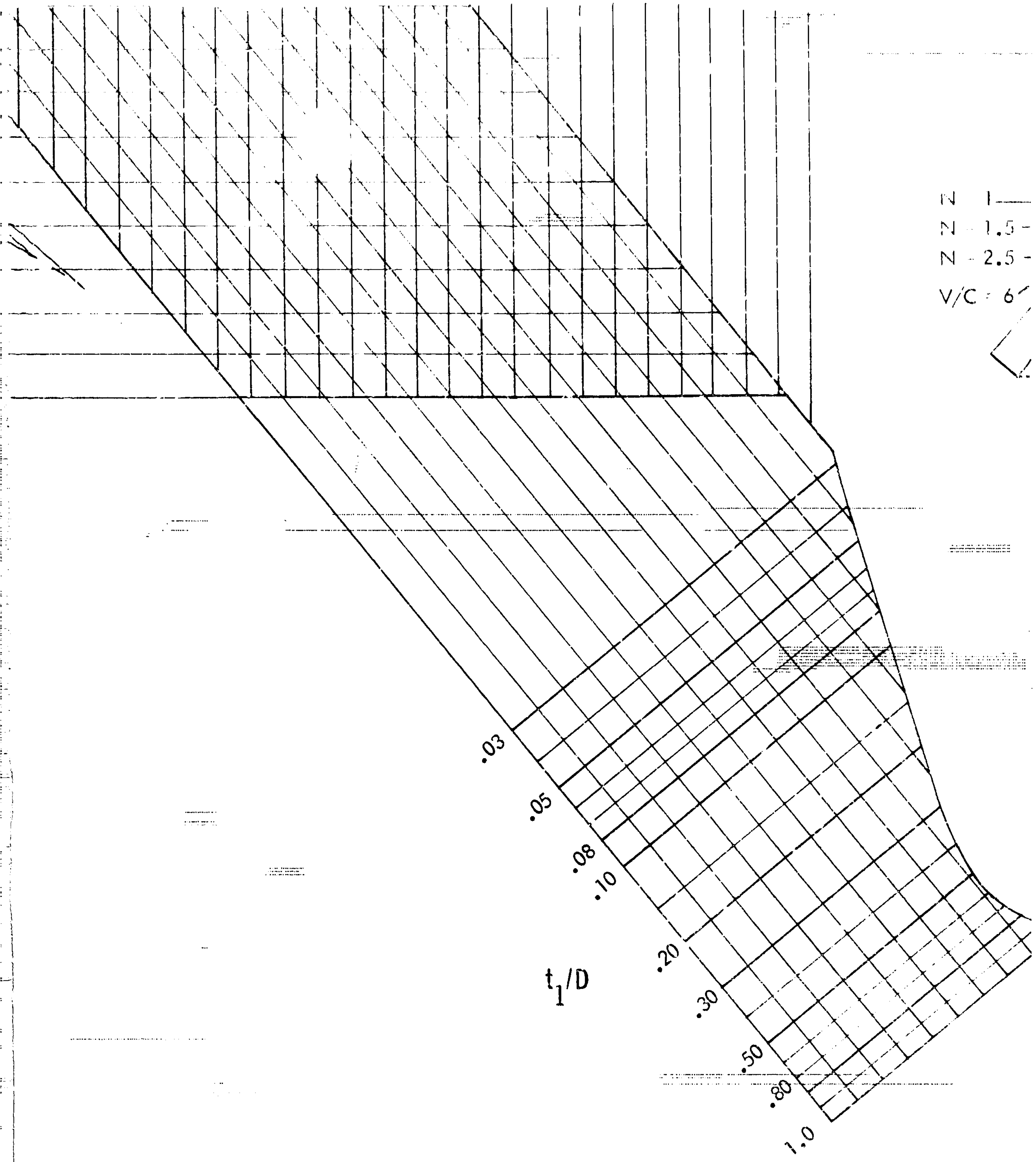
N = 1
N = 1.5
N = 2.5
V/C = 6
.03
.05
.08
.10
.20
.30
.50
.80
1.0
t_1/D

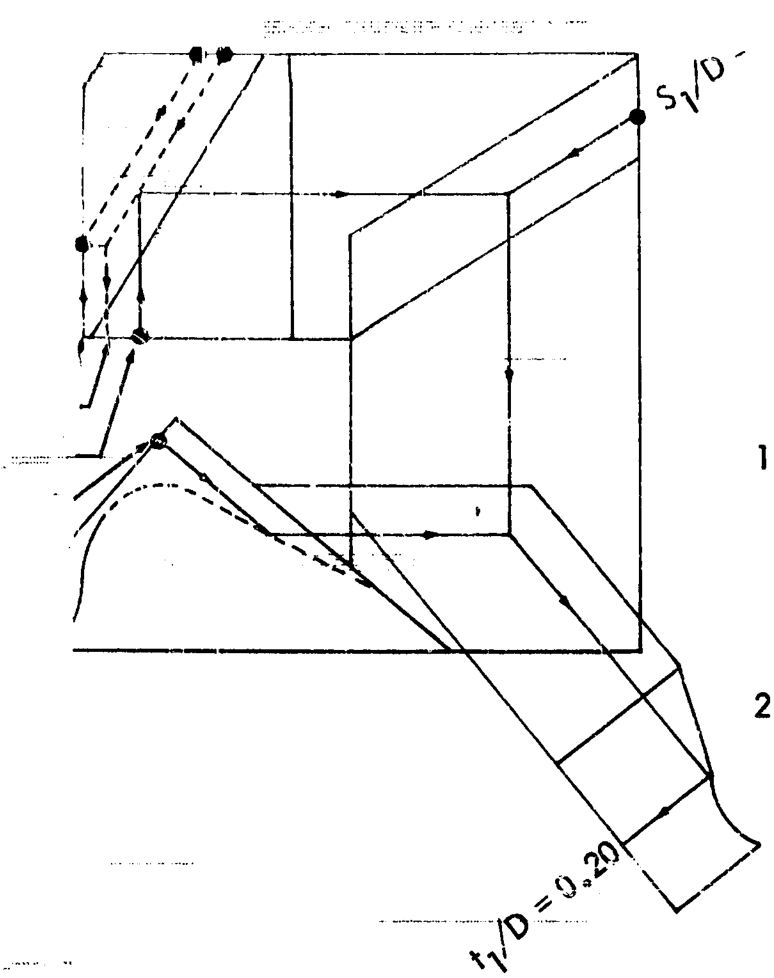

EXAMPLE 2 - DESIGN OF FIRST SHEET OF A THREE-SHEET BARRIER

1. Find number of sheets of equal thickness t_2 of an equivalent penetration resistance barrier, i.e. convert sheet 3 to an equivalent number of sheets of thickness t_2. Enter nomogram at N = 1 and $t_2/D = 0.148$. Move horizontally to $t_2/D = 0.074$. The result is 1.5 sheets.

2. Re-enter the nomogram at the total equivalent number of t_2/D sheets (N = 2.5), $t_2/D = 0.074$, $S_1/D = 18.5$, and V/C = 6. The result is $t_1/D = 0.20$.

EXAMPLE	GIVEN	STEP 1	STEP 2
D	0.27		
V/C	6		6
t_2/D	0.074	0.148	0.074
t_3/D	0.148		
S_1/D	18.5		18.5
N		1	2.5
t_1/D	?		0.20
RESULT		N = 1.5	$t_1 = 0.054$